Reconstruction methods for single-shot diffractive imaging of free nanostructures with ultrashort x-ray and XUV laser pulses

Dissertation zur Erlangung des akademischen Grades
doctor rerum naturalium
an der Mathematisch-Naturwissenschaftlichen Fakultät
der Universität Rostock

vorgelegt von

Katharina Sander

Rostock, August 2018

https://doi.org/10.18453/rosdok_id00002439

Betreuer:	Prof. Dr. Thomas Fennel (Universität Rostock)
Gutachter:	Prof. Dr. Thomas Fennel (Universität Rostock) Prof. Dr. Bernd von Issendorff (Universität Freiburg)
Eingereicht:	15.8.2018
Verteidigung:	25.1.2019

List of own publications

[1] K. Sander, C. Peltz, C. Varin, S. Scheel, T. Brabec, and T. Fennel, "Influence of wavelength and pulse duration on single-shot x-ray diffraction patterns from nonspherical nanoparticles", *Journal of Physics B: Atomic, Molecular and Optical Physics*, vol. 48, 204004, 2015

[2] D. Rupp, N. Monserud, B. Langbehn, M. Sauppe, J. Zimmermann, Y. Ovcharenko, T. Möller, F. Frassetto, L. Poletto, A. Trabattoni, F. Calegari, M. Nisoli, K. Sander, C. Peltz, M. J. Vrakking, T. Fennel, and A. Rouzée, "Coherent diffractive imaging of single helium nanodroplets with a high harmonic generation source", *Nature Communications*, vol. 8, 493, 2017

[3] B. Langbehn, K. Sander, Y. Ovcharenko, C. Peltz, A. Clark, M. Coreno, R. Cucini, M. Drabbels, P. Finetti, M. Di Fraia, L. Giannessi, C. Grazioli, D. Iablonskyi, A. C. LaForge, T. Nishiyama, V. Oliver Álvarez de Lara, P. Piseri, O. Plekan, K. Ueda, J. Zimmermann, K. C. Prince, F. Stienkemeier, C. Callegari, T. Fennel, D. Rupp, and T. Möller, "Three-dimensional shapes of spinning helium nanodroplets", *Phys. Rev. Lett.*, vol. 121, 255301, 25 Dec. 2018

List of presentations

Talks:

04.03.2015 Graduate School Workshop, Bentwisch
Discrete Dipole Approximation: Optimization and Applications

24.11.2015 Theory Seminar, Rostock
Influence of wavelength and pulse duration on single-shot x-ray diffraction patterns from nonspherical nanoparticles

29.02.2016 DPG Spring Meeting (Section AMOP), Hannover
Influence of wavelength and pulse duration on single-shot x-ray diffraction patterns from nonspherical nanoparticles

08.06.2017 Graduate School Seminar, Rostock
Three-dimensional characterization of free nanostructures via two-color coherent diffractive imaging

Posters:

18.03.2014 DPG Spring Meeting (Section AMOP), Berlin
Microscopic Description of single-shot diffractive imaging of clusters via the dyadic Green's function approach

25.11.2014 Atomic Physics Conference, Dresden
Microscopic Description of single-shot diffractive imaging of clusters via the dyadic Green's function approach

23.03.2015 DPG Spring Meeting (Section AMOP), Heidelberg
Microscopic Description of single-shot diffractive imaging of atomic clusters

27.07.2015 IMPRS-MAP Workshop, Wildbad-Kreuth
Influence of wavelength and pulse duration on single-shot x-ray diffraction patterns from nonspherical nanoparticles

15.09.2015 CERF conference, Rostock
Influence of wavelength and pulse duration on single-shot x-ray diffraction patterns from nonspherical nanoparticles

21.09.2015 Clustertreffen, Lindow
Influence of wavelength and pulse duration on single-shot x-ray diffraction patterns from nonspherical nanoparticles

29.01.2016 XFEL User's Meeting, Hamburg
Influence of wavelength and pulse duration on single-shot x-ray diffraction patterns from nonspherical nanoparticles

09.03.2017 DPG Spring Meeting (Section AMOP), Mainz
Three-dimensional chracterization of free nanostructures via two-color coherent diffractive imaging

15.06.2017 SFB Abschlusskolloquium, Rostock
Three-dimensional chracterization of free nanostructures via two-color coherent diffractive imaging

25.09.2017 Clustertreffen, Bacharach
Three-dimensional characterization of free nanostructures via two-color coherent diffractive imaging

Contents

List of Figures

List of Tables

1. Introduction

For the understanding of physical and chemical properties of nanometer sized objects, knowledge about their structure is an important prerequisite, as the specific physical and chemical properties are often closely connected to structure and shape. An understanding of basic behaviors and their relation to the morphology of particles such as molecules, proteins, bacteria and viruses is of great interest also in biology and medicine. The connection between function and structure could e. g. successfully be utilized for the structure determination of the DNA (deoxyribonucleic acid) via x-ray diffraction, that revealed the double helix structure with paired bases and allowed to understand mechanisms of biological information storage and transfer [133]. Not only the biological function is connected to shape, size and structure of particles, for nanocrystals it is connected to optical, catalytic, electronic and magnetic properties [17]. Further, structure determination of nanometer sized objects allows to approach questions in many branches of fundamental research. For example, the arrangement of magnetic moments in crystals can be investigated by neutron powder diffraction [106]. With a combination of scanning tunneling microscopy and dynamical low energy electron diffraction, the shape of atomic clusters deposited on surfaces can be verified [18]. The course of chemical reactions can be identified by x-ray diffraction [88].

The above examples already show that a broad range of methods exist for structure determination of nanotargets. In general, it is possible by utilizing either light, electron or neutron scattering. The main contribution to the scattered signal from light and electron scattering emerges from the interaction with electrons, the main contribution in neutron scattering from the interaction with the nuclei. In this thesis, the focus is put on nanotargets in free flight, since compared to fixed targets the absence of interaction with the surrounding does not alter the shape and structure of the targets and simplifies the interpretation of experimental results. For the investigation of free-flying nanotargets, light scattering is best suited. The reason is that electron scattering is only applicable to fixed targets and although neutron scattering enables the resolution of magnetic moments and oxygen positions, materials relying on this feature are not considered here. Hence, light scattering will be in the center of this thesis.
For structure determination of free-flight nanotargets utilizing light the target is illuminated and the scattered light is recorded on a detector. A basic setup of such an experiment is depicted in fig. 1.1. The obtained scattering image contains information about the object's size, shape and structure. This imaging procedure at first sounds very simple. However, as illustrated in the following, for resolving nanostructures, high demands on the light source are made and in addition numerical methods to extract information about

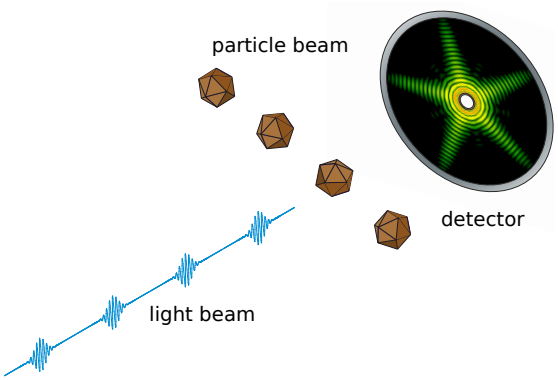

Figure 1.1.: Sketch of single-shot diffractive imaging experiment with light beam hitting a particle beam. The scattered field is recorded on a detector.

the target from the scattering image are indispensable.

In the far-field, the scattered field from the object is directly connected to the Fourier transform of the object's density, i. e. it represents a reciprocal space image. Experimentally, this reciprocal space image or far-field diffraction pattern can be converted to a real space image with lenses. The resolution that can be achieved in such an imaging scenario, i. e. the minimal distance of two separate structures that can be resolved, is limited by the diffraction of light. The minimal distance d that can be resolved by light of a certain wavelength λ is given by Ernst Abbe's formula

$$d = \frac{\lambda}{2n \sin \alpha}, \tag{1.1}$$

where n is the refractive index and α the angle of incidence. With nonlinear methods such as stimulated emission depletion (STED) microscopy resolution below the diffraction limit can be achieved [56]. However, this method can only be applied to embedded targets that can be stimulated to fluoresce. For the targets considered in this thesis the resolution on the nanometer scale can only be achieved by utilizing wavelengths on the same order, i. e. x-ray or extreme ultraviolet (XUV) light is required. In this wavelength regime, a high photon flux is needed to collect enough elastically scattered photons. Since the targets are imaged in free flight, the scattered photons have to be generated in a single shot. Thus, to reach sufficiently high light intensities to meet this requirement, pulse durations have to be very short. In addition to that, the short pulse durations are required to image the nanoparticle before its destruction due to the interaction with the high-intensity beam [91]. The usage of x-ray and XUV laser pulses inhibits the possibility to convert the reciprocal space image to real space, since no efficient optical components are available for this wavelength regime. Thus, the diffraction pattern (in reciprocal space) is directly recorded behind the scattering region e. g. with a charged-coupled device (CCD) camera or a micro-channel plate (MCP) detector.

To sum up, for recording evaluable diffraction patterns of free-flight nanotargets utilizing light, the laser beam has to fulfill three basic requirements. Its wavelength needs to be in the XUV or x-ray regime and the laser pulses need to be very intense and ultrashort. In the imaging process, the diffraction pattern (squared amplitude of complex scattered electric field) is obtained in a single-shot. The encoded information about size, shape, structure and orientation of the target needs be reconstructed by numerical methods. This procedure then is called coherent diffractive imaging (CDI). The aim of this work, is to present, discuss and advance existing reconstruction methods and apply them to different scattering scenarios.

As an introduction, this chapter gives an overview about the current state of the research of coherent diffractive imaging (CDI). Therefore, in the first section, basics of single-shot diffraction experiments are discussed with giving a short description of the available light sources and experiments that already have been conducted. In the second part the two existing approaches for structure recovery are presented; (i) reconstruction by phase retrieval methods and (ii) reconstruction with forward fits. In the last part, the aim of this work is described in more detail.

1.1. Available light sources for single-shot diffractive imaging

Single-shot diffractive imaging experiments became possible in the past few decades due to the development of high brilliant light sources, such as synchrotrons and free electron lasers (FELs), depicted in fig. 1.2. Also high harmonic generation light sources start to become important for imaging and are discussed in more detail in the last part of this section. Figure 1.2 shows the peak brilliance reached at different light sources in dependence on photon energy. The peak brilliance is a measure of number of photons produced per second, per 0.1 % bandwidth, per unit solid angle, and per unit area. Synchrotrons reach higher photon energies but are orders of magnitude lower in peak brilliance than the free electron lasers, i. e. the scattered signal at synchrotrons is much smaller. However, synchrotrons enable the imaging of crystallized particles by long illumination times [94]. Although large non-crystalline samples can be imaged in synchrotrons [82], small non-crystalline targets do not generate a large enough scattering signal to obtain an adequate diffraction pattern. Since crystallization, e. g. of bio systems, often is not feasible [126], higher light intensities are needed to generate enough scattered signal of nanometer sized particles. FELs with much shorter pulse durations and therefore higher light intensities (cf. fig. 1.2) [36, 41, 119, 35, 65, 2] offer a solution to this problem. They enable imaging of non-crystalline targets [22] in a single shot.
Free electron lasers enable a very broad spectrum of experiments. The main benefit compared to synchrotrons and electron microscopy (which also requires embedding [1]) is the possibility of FELs to image nanoparticles in free flight. In free flight there is no

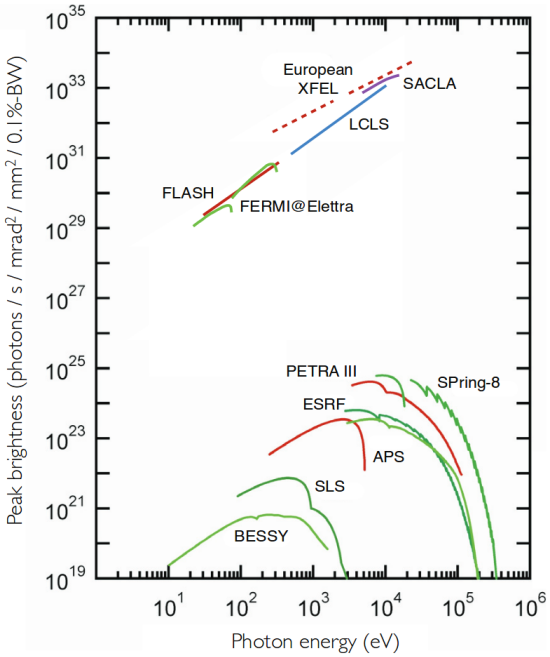

Figure 1.2.: Overview of peak brilliance in dependence on photon energy reached at free electron lasers and synchrotron facilities. Figure taken from [63].

spurious interaction due to a deposition on a substrate. This allows for investigation of metastable and transient states that only exist in the gas phase. Experiments e. g. have been conducted on non-crystalline specimen [81], aerosols [76], atomic clusters [13, 108, 48, 10], nanocrystals [136], free particles in the gas-phase [12, 20], biomolecules [42, 34], viruses [127, 122] and helium nanodroplets [48]. Further, dynamics could be observed; quantum vortices in helium nanodroplets [48], ultrafast changes of electronic properties in nanoplasma formation [14, 111], particle shape evolution during growth processes [110] and the explosion of laser-heated clusters [49].

Up to now, only large-scale facilities have been presented. However, although high harmonic generation (HHG) sources are orders of magnitude lower in brightness than FELs [83], in the past few years the achievable intensity and/or average power of these lab-based sources increased [58, 53, 107, 131, 61, 98] enabling HHG single-shot diffractive imaging on fixed targets [82, 116, 101, 23, 121, 145]. In such experiments a resolution of 20 nm could be reached with multiple exposures [121, 145] and even single exposures in some cases [101].

1.2. Reconstruction methods

The obtained scattered intensity distribution in single-shot diffractive imaging experiments encodes information about shape, structure and orientation of the imaged targets

in reciprocal space. For particle reconstruction, i. e. to convert the diffraction patterns to a real space image of the particle, numerical simulations are required. The diffraction pattern is proportional to the squared amplitude of the scattered electric field, the phase is lost. To solve the phase problem, basically two approaches exist. First, the phase can be retrieved by so-called phase retrieval algorithms that are based on oversampling. Second, the diffraction pattern can be forward fitted, by computing the scattered intensity from model shapes and compare them to the experiment. The utilized wavelength of the radiation has a large impact on the methods that can be applied for reconstruction, since it influences the resolvable scattering angle on the detector. In a single-shot diffractive imaging experiment a certain maximal momentum transfer q can be resolved that depends on the dynamical range the detector can resolve. The momentum transfer is connected to the scattering angle Θ and wavelength λ via

$$q = \frac{4\pi}{\lambda} \sin(\Theta/2). \tag{1.2}$$

The relation reveals that for longer wavelength larger scattering angles can be accessed in the experiment for a fixed q. Figure 1.3 shows the difference in resolvable scattering angles for different wavelength regimes. In fig. 1.3a the scattered photon with outgoing wave vector $\mathbf{k}_{\text{out}}$ is only weakly deflected from the incoming wave vector $\mathbf{k}_{\text{in}}$, the diffraction pattern is restricted to small scattering angles. In this case, the momentum transfer ($\mathbf{q} = \mathbf{k}_{\text{out}} - \mathbf{k}_{\text{in}}$) is parallel to the projection plane (indicated in blue), hence, the diffraction pattern is only dependent on the particle density projected onto that plane. Figure 1.3b illustrates the wide angle scattering regime in which the outgoing photons are deflected further away from the optical axis. In this case, also momentum transfers that are not parallel to the detector plane (indicated in red) are accessible. Thus, the orientation of the particle impacts the diffraction pattern, as also has been shown in [100, 136, 10]. When utilizing hard x-ray radiation with photon energies on the order of keVs, the diffraction pattern is restricted to small scattering angles (cf. eq. (1.2)) and atomic resolution is feasible [81, 136]. Additionally, absorption is small and usually negligible. For this wavelength regime, phase retrieval algorithms are applicable. For larger wavelength radiation, such as soft x-ray and XUV light, larger scattering angles can be resolved and the diffraction patterns are not a function of the projected particle density, but depend on its 3D orientation. In addition, absorption has a large impact on the diffraction pattern and hence, phase retrieval algorithms are not simply applicable anymore. Therefore, in this regime, forward fit methods are more suitable for particle reconstruction. In the following subsections, both approaches are discussed in more detail.

1.2.1. Phase retrieval algorithms

The loss of phase information when obtaining the diffraction pattern has to be overcome by oversampling [118, 85]. The oversampled diffraction pattern is applicable to phase retrieval algorithms. The iterative approach is based on alternating projections, first introduced

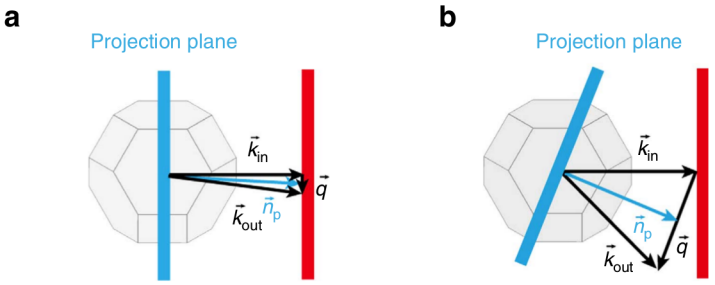

Figure 1.3.: a) In the small angle scattering regime the momentum transfer $\mathbf{q} = \mathbf{k}_{out} - \mathbf{k}_{in}$ (difference between incident and outgoing wave vector) is parallel to the projection plane (indicated in blue) ($\mathbf{q} = \mathbf{q}_{\parallel}$) and the scattering image on the detector (indicated in red) is dependent only on the projection of the particle density onto that plane. b) For the same scenario, with larger $\mathbf{q}$ projection planes (indicated in blue) not parallel to the detector (indicated in red) can be accessed. In this wide angle scattering regime the scattering image is dependent on the 3D orientation of the particle. Figure taken from [10].

by Gerchberg and Saxton [43] and extended by Fienup [38, 37]. Constraints on Fourier space (diffraction pattern) and real space (density) support are applied sequentially until convergence is reached. In one dimension, no unique solution for the phase retrieval exists, as the starting point is a random Fourier phase that can result into a valid solution that can be far away from the real solution [60]. For higher dimensions, however, the solution is unique [16, 55, 11]. Phase retrieval algorithms have been shown to work in electron microscopy on gold nanocrystals [135] and carbon nanotubes [144]. In lensless optical imaging successful 2D reconstruction on several experimental diffraction patterns has been done; on a non-crystalline sample consisting of array of gold dots [81], gold nanocrystals [105], an artificial 2D sample [21], viruses [127], a bone sample [27], intersections of mimiviruses [122] and aerosol particles [76]. The drawback of existing phase retrieval algorithms is that additional constraints to the object are necessary, they are unstable in presence of noise which requires user interaction. Holographic methods can highly accelerate the algorithm as e. g. shown in [50]. A contemporary overview of phase retrieval in optical imaging is given in [124] and a review of its experimental robustness can be found in [141].

Three-dimensional phase retrieval is only applicable when illuminating identical particles from different sides and assembling the diffraction patterns to a 3D Fourier volume. However, particles in free flight are randomly oriented in space, to be able to perform a 3D phase retrieval, the unknown orientations need to be extracted from the diffraction patterns. A number of different algorithms for orientation-retrieval have been reviewed in [62]. For crystalline targets orientation tagging can be performed by analyzing the position of the Bragg peaks [140, 8]. Further, several self-orienting algorithms for non-crystalline targets exist. In manifold embedding methods [120] (diffusion map, isomal and generative topographic mapping (GTM)) a consistent set of particle orientations is found by identifying pairs of similar diffraction patterns. GTM has been shown to work on synthetic data [40]. Intensity cross-correlation methods [67, 115, 28] have been shown

to work on 2D reconstruction [96]. Another approach accounts for underlying symmetries of orientation space that lead to approximate symmetries of diffraction patterns [45], combined with manifold embedding techniques. A simplified version of [45] can be found in [68]. The expand-maximize-compress (EMC) algorithm is based on probabilistic modeling of detector photon counts [77], but was shown to be fundamentally equivalent with GTM [89]. EMC has been verified with synthetic data [75]. Further, proof-of-principle experiments have been conducted [97, 6, 7, 134]. 3D reconstruction from experimental data has been shown to work on a mimivirus with a resolution of 150 nm for a 1 nm wavelength [34]. Hence, the available stochastical methods work on synthetic data, but up to now the experimental results deliver a quite low resolution.

1.2.2. Forward fit methods

In forward fit methods, the scattered intensity is computed for a given model shape and compared to experimental diffraction patterns. Different algorithms exist to accomplish this. Mie theory describes electromagnetic scattering from spherical, ellipsoidal and cylindrical targets including absorption from near- to far-fields [84, 64, 5]. It can be applied to any size and wavelength and often is utilized as benchmark model for other numerical methods. For non-spherical targets, several numerical methods are employable. The finite difference time domain (FDTD) technique [139, 137, 129] solves Maxwell's equations on a grid in a leap-frog approach, absorption is included. The far-field scattering image is obtained by a near-far-field transformation. In terms of required memory the method is computationally very expensive. The approach has been applied to describe light scattering from small ice crystals [137], cells [33, 32] and dielectric particles [128]. A gridless approach that is less memory exhausting is the discrete dipole approximation (DDA) [99, 31]. It describes the particle as an ensemble of discrete point dipoles that each interact with the incident field and the scattered fields from the other dipoles. Near- and far-field components and absorption are included. The accuracy of DDA is discussed in [30, 29, 59]. It is widely used in various areas, e. g. for description of optical properties of nanostructures [29, 132], plasmonic response of nanoparticles [73, 112] and Raman scattering intensities [138]. FDTD and DDA are advanced models that are computationally expensive and therefore not applicable for fast forward fitting data if not already a good selection of model shapes exist. For finding such a selection the multislice Fourier transform method (MSFT) is more convenient. It is a simple and efficient model that only includes far-field components. The scattered field is computed by Fourier transforming particle slices that are summed up phase-correctly on the detector. Absorption can be included via Beer-Lambert's law. MSFT has applications in electron scattering [25, 123, 103] and soft x-ray diffraction of supported particles [54]. It has been utilized as forward fit method on silver nanoparticles [10] and as a part of this work on helium nanodroplets [72]. Note, that the best fit found for a certain diffraction pattern can only be as good as the chosen model shapes and is not necessarily a unique solution. This can only be ensured by utilizing phase retrieval algorithms, which, however, are not applicable to all

scattering scenarios (cf. chp. 1.2.1).

1.3. Aim of this work

The aim of this thesis is the reconstruction of free nanoparticles from single-shot diffractive imaging experiments. Therefore, numerical methods for the description of light scattering of extreme ultraviolet (XUV) and x-ray radiation by nanotargets are derived, implemented and applied to experimental data. The applicable numerical methods highly depend on the wavelength utilized for the imaging process, therefore it is necessary to understand the influence of this parameter onto the diffraction pattern. Hence, a systematic study of the effect of different wavelength on the diffraction pattern is provided in this thesis. Further, the diffraction pattern needs to be obtained before the particle is destructed [91]. To this end, short pulse durations are favorable and also necessary to resolve fast electron dynamics. The advent of single-shot imaging experiments with HHG radiation [82, 116, 101, 23, 121, 145] and the possible seeding of FELs with HHG pulses [114] moves the potential of imaging with attosecond pulse durations closer. Therefore, the influence of different pulse durations is investigated to estimate if attosecond imaging even is feasible.

One major goal of single-shot diffractive imaging is to gain understanding about shape and structure of nanoparticles. To this end, forward fit methods are applied to different experiments in this work. Single-shot diffractive imaging offers the opportunity to characterize warm dense matter (WDM), which is important for understanding astrophysical objects [52] and initiate laser-driven fusion [74]. Typical approaches for determining plasma properties of WDM such as temperature, density and ionization state is spectrally resolved x-ray Thomson scattering (XRTS) [104, 51, 102, 47]. In XRTS, usually two detectors are needed to record a backward scattering signal from structural disorder and forward scattering from the target shape to deduce the dynamical structure factor from the data. In this thesis, the possibility to resolve both signals from structural disorder and shape on a single detector by single-shot diffractive imaging on a jet target is investigated. Further, the impact of different properties of the finite jet target on the diffraction patterns is analyzed and compared to experimental results from a FLASH experiment by Zastrau *et al.*.

Most single-shot diffractive imaging experiments are conducted at FEL facilities, however, due to ongoing developments in HHG radiation sources, these light sources start to be feasible for imaging experiments. So far, HHG single-shot diffractive imaging experiments only have been conducted on supported particles as described in sec. 1.1. In this work, the first HHG imaging experiment on helium nanodroplets in free flight performed by Nils Monserud and Daniela Rupp *et al.* is presented. The diffraction patterns of spherical helium droplets are utilized to extract material specific wavelength dependent refractive indices. Forward fitting non-spherical diffraction patterns by exploiting large scattering angles allow for the 3D reconstruction of non-spherical helium droplets.

For hard x-ray scattering experiments diffraction patterns are restricted to small scattering angles, in which the scattering image is proportional to the Fourier amplitude of the projected particle density. Further, in this regime absorption is usually negligible, which enables the reconstruction with phase retrieval algorithms [37]. Successful 2D reconstruction from 2D scattering patterns has been achieved in several scenarios [81, 105, 21, 127, 27, 122, 76]. For gaining information about the three-dimensional shape and structure of the target the 3D Fourier amplitude is required. To obtain it, the nanotarget has to be imaged from different sides and according to the particle orientation, the diffraction patterns have to be assembled to a 3D Fourier volume. The most challenging part is the necessary orientation tagging of the small angle diffraction patterns. Complex stochastical approaches exist to solve this task, as outlined in sec. 1.2.1. In this work, a simple approach to solve the orientation tagging task is proposed that builds on the possibility to image the target with two different wavelength in the wide and small angle scattering regime at the same time. Therefore, a route to find a particle orientation to a small angle diffraction pattern by utilizing information of a corresponding wide angle diffraction pattern is tested. The orientation tagged small angle diffraction patterns then are applied to 3D phase retrieval.

Structure of this thesis

The second chapter of this thesis is dedicated to the basic principles of light scattering in linear response. Hence, in the chapter, the relevant theory is derived by starting from the microscopic Maxwell's equations. From these equations, approximations for different scattering regimes are deduced, i. e. the wide and small angle scattering regime.
In the third chapter, the effects of different laser parameters on the diffraction patterns are investigated. To this end, the influence of wavelength and pulse duration on the scattering images are analyzed.
In the fourth chapter, scattering from hydrogen jets is studied, by analyzing typical properties of the corresponding diffraction patterns and how the shape and orientation of the jet impacts the scattering images. Further, characteristic features found in the simulations are connected to features in experimental diffraction patterns.
In chapter 5, diffraction patterns from a high harmonic generation scattering experiment on free helium nanodroplets are analyzed to extract optical parameters of helium and information about the 3D shape of helium nanodroplets in the superfluid state.
Chapter 6 presents a two-color single-shot diffractive imaging approach, that enables the orientation tagging of randomly oriented targets and consequently the 3D particle reconstruction by 3D phase retrieval on the example of an asymmetric target (tripod) and a highly symmetric target (icosahedron).

The contents of chapter three and five have been published in [117] and [109], respectively.

2. Basic principles of scattering theory in linear response

Single-shot diffractive imaging experiments enable the characterization of shape, size and structure of free nanotargets. In such an experiment, a high-intensity laser is shot at a nanotarget and the light scattered by it is recorded on a detector. In this work, methods for reconstruction of the imaged nanotargets from the diffraction patterns are developed or improved and applied to different scattering scenarios with noble gas clusters, helium nanodroplets and hydrogen jets. To derive the reconstruction methods, the numerical description of the scattering scenario requires to be applicable to different scattering regimes with different incident laser wavelength and targets with different material properties such as size, shape and refractive index. For reconstruction of the particle density from diffraction patterns, the scattering problem has to be solved or inverted. The scattering problem can be described with Maxwell's equations and solving it can be extremely complex and complicated. As shown in this chapter, for certain regimes it can be solved approximately. Therefore, a mathematical description of the scattering problem in linear response is introduced, where damage due to the interaction with the laser beam is neglected. The chapter is separated into two parts.
First, a general expression for the scattered electric field in presence of incident laser field and finite material is deduced. Therefore, the electric field evolution in space is obtained by solving Maxwell's equations utilizing a Green's function approach. Second, approximations to the general description of the scattered field are introduced in the regimes of weak and strong scattering. In the regime of weak scattering, additional simplifications in the far-field region are presented that include a simple description for small and wide angle scattering.

2.1. Scattered electric field

In this section, the scattered electric field generated due to the interaction of a finite object with a monochromatic laser is deduced as a function of particle density distribution and the electric field acting on it. The derivation follows the steps in [92]. Starting from the microscopic Maxwell's equations, the electric field wave equation is derived, which describes the spatial evolution of the electric field for a certain current density. The wave equation then is solved utilizing a dyadic Green's function approach. An explicit form of the dyadic Green's function is derived with the help of a scalar Green's function that solves the inhomogeneous Helmholtz equations. Last, a current density description in terms of charge density and local electric field is introduced, ending up with a description

of the scattered electric field depending only on material properties and the electric field acting on the target.

2.1.1. Electric field wave equation

Starting point for the derivation are the microscopic Maxwell's equations [80], which dictate the spatial and temporal evolution of the electric and magnetic fields $\mathbf{E}(\mathbf{r},t)$ and $\mathbf{B}(\mathbf{r},t)$ in presence of a material via

$$\nabla \cdot \mathbf{E}(\mathbf{r},t) = \frac{\rho(\mathbf{r},t)}{\epsilon_0}, \tag{2.1}$$

$$\nabla \cdot \mathbf{B}(\mathbf{r},t) = 0, \tag{2.2}$$

$$\nabla \times \mathbf{E}(\mathbf{r},t) = -\frac{\partial}{\partial t}\mathbf{B}(\mathbf{r},t), \tag{2.3}$$

$$\nabla \times \mathbf{B}(\mathbf{r},t) = \mu_0 \mathbf{j}(\mathbf{r},t) + \mu_0 \varepsilon_0 \frac{\partial}{\partial t}\mathbf{E}(\mathbf{r},t), \tag{2.4}$$

where $\mathbf{r} = (x,y,z)$ denotes the location, t the time, ε_0 the electric permittivity and μ_0 the magnetic permeability. The charge density $\rho(\mathbf{r},t)$ and the current density $\mathbf{j}(\mathbf{r},t)$ determine the material response. Further, ∇ is the nabla operator, $\nabla\cdot$ denotes the divergence and $\nabla\times$ the curl operator. All fields are real-valued and contain the full time dependence and all spectral components. For description of electric fields from monochromatic lasers, it is necessary to consider only a single frequency. To obtain Maxwell's equations for a single spectral component, the fields can be written as time harmonic fields, here done exemplarily for $\mathbf{E}$ for the angular frequency ω

$$\mathbf{E}(\mathbf{r},t) = \frac{1}{2}\left[\mathbf{E}(\mathbf{r})e^{-i\omega t} + \mathbf{E}^*(\mathbf{r})e^{i\omega t}\right], \tag{2.5}$$

where $\mathbf{E}(\mathbf{r})$ denotes the complex electric field and $\mathbf{E}^*(\mathbf{r})$ its complex conjugate. It is sufficient to only consider the first term. Due to the linearity of Maxwell's equations, the real-valued fields can easily be constructed if needed. Inserting eq. (2.5) into the Maxwell's equations (2.1)-(2.4) gives

$$\nabla \cdot \mathbf{E}(\mathbf{r}) = \frac{\rho(\mathbf{r})}{\varepsilon_0}, \tag{2.6}$$

$$\nabla \cdot \mathbf{B}(\mathbf{r}) = 0, \tag{2.7}$$

$$\nabla \times \mathbf{E}(\mathbf{r}) = i\omega \mathbf{B}(\mathbf{r}), \tag{2.8}$$

$$\nabla \times \mathbf{B}(\mathbf{r}) = \mu_0 \mathbf{j}(\mathbf{r}) - i\omega\mu_0\varepsilon_0 \mathbf{E}(\mathbf{r}), \tag{2.9}$$

The term $e^{-i\omega t}$ cancels on the left and right hand sides of the equations. The wave equation for the electric field that describes its evolution in space can easily be obtained

by combining eqs. (2.8) and (2.9), which yields

$$\nabla \times \nabla \times \mathbf{E}(\mathbf{r}) - k^2 \mathbf{E}(\mathbf{r}) = i\omega\mu_0 \mathbf{j}(\mathbf{r}). \tag{2.10}$$

The structure of the wave equation reveals that the x, y and z component of the electric field and current density depend on each other. For a point source, the equation can be solved by utilizing a Green's function approach. Therefore, the current density is described via (exemplarily for the x component)

$$\mathbf{j}_x(\mathbf{r}) = \frac{\delta(\mathbf{r} - \mathbf{r}')}{i\omega\mu_0} \mathbf{e}_x, \tag{2.11}$$

with the delta function δ, $\mathbf{r}'$ denoting the point source position and $\mathbf{e}_x$ the unit vector in x-direction. Inserting this equation into eq. (2.10) gives

$$\nabla \times \nabla \times \mathbf{G}_x(\mathbf{r}, \mathbf{r}') - k^2 \mathbf{G}_x(\mathbf{r}, \mathbf{r}') = \delta(\mathbf{r} - \mathbf{r}')\mathbf{e}_x, \tag{2.12}$$

where $\mathbf{G}_x(\mathbf{r})$ is the field generated by the point current $\mathbf{j}_x$. Moreover, $\mathbf{G}_x(\mathbf{r})$ is the vector corresponding to the first column of the so-called dyadic Green's function $\overleftrightarrow{\mathbf{G}}(\mathbf{r}, \mathbf{r}')$. The full solution for all current density components is given by

$$\nabla \times \nabla \times \overleftrightarrow{\mathbf{G}}(\mathbf{r}, \mathbf{r}') - k^2 \overleftrightarrow{\mathbf{G}}(\mathbf{r}, \mathbf{r}') = \delta(\mathbf{r} - \mathbf{r}')\overleftrightarrow{\mathbf{I}}, \tag{2.13}$$

with $\overleftrightarrow{\mathbf{I}}$ being the unity diad. Assuming the current density in eq. (2.10) can be viewed as superposition of point currents, the electric field can then be expressed via

$$\mathbf{E}(\mathbf{r}) = i\omega\mu_0 \int \overleftrightarrow{\mathbf{G}}(\mathbf{r}, \mathbf{r}')\mathbf{j}(\mathbf{r}')dV'. \tag{2.14}$$

This is a so-called volume-integral equation. For its solution, an explicit expression of the dyadic Green's function and current density is required. The dyadic Green's function can easily be deduced by moving to a description of the Maxwell's equations in terms of scalar and vector potentials, which allows for presentation of the dyadic Green's function in dependence on a scalar Green's function. Therefore, the vector and scalar potentials are introduced in the following. Further, the scalar Green's function is derived by introducing the inhomogeneous Helmholtz equations. A current density description is obtained afterwards for a charge density distribution.

2.1.2. Dyadic and scalar Green's function

For deducing an explicit form of the dyadic Green's function Maxwell's equations are first simplified by introducing the scalar and the vector potential $\Phi(\mathbf{r})$ and $\mathbf{A}(\mathbf{r})$ via

$$\mathbf{E}(\mathbf{r}) = i\omega\mathbf{A}(\mathbf{r}) - \nabla\Phi(\mathbf{r}), \tag{2.15}$$
$$\mathbf{B}(\mathbf{r}) = \nabla \times \mathbf{A}(\mathbf{r}). \tag{2.16}$$

Maxwell's equations (2.7) and (2.8) are fulfilled automatically for these potentials. The scalar and vector potentials are not uniquely defined yet meaning that Gauge transformations that do not alter magnetic and electric fields can be applied e. g. by adding a curl-free component $\nabla \cdot \mathbf{A}$. For further simplification, the Lorenz gauge is a convenient choice

$$\nabla \cdot \mathbf{A}(\mathbf{r}) = i\omega\mu_0\varepsilon_0\Phi(\mathbf{r}). \tag{2.17}$$

By inserting the Lorenz gauge into eq. (2.15), the electric field can be expressed only in terms of the vector potential

$$\mathbf{E}(\mathbf{r}) = i\omega\left[1 + \frac{1}{k^2}\nabla\nabla\cdot\right]\mathbf{A}(\mathbf{r}). \tag{2.18}$$

To solve the above equation for the field generated by a point source, i. e. generated by the dyadic Green's function, an expression for the vector potential in presence of a point source is needed. A solution for such a vector potential can easily be found by solving the inhomogeneous Helmholtz equations, a symmetric form of Maxwell's equations for a point source. The inhomogeneous Helmholtz equations can be obtained by inserting eqs. (2.15) and (2.16) into eqs. (2.6) and (2.9) which gives

$$i\omega\nabla \cdot \mathbf{A}(\mathbf{r}) = \frac{\rho(\mathbf{r})}{\varepsilon_0} + \Delta\Phi(\mathbf{r}) \tag{2.19}$$
$$\nabla \times \nabla \times \mathbf{A}(\mathbf{r}) = \mu_0\mathbf{j}(\mathbf{r}) - i\omega\mu_0\varepsilon_0\left(i\omega\mathbf{A}(\mathbf{r}) - \nabla\Phi(\mathbf{r})\right). \tag{2.20}$$

Inserting again the Lorenz gauge eq. (2.17) into eqs. (2.19) and (2.20) and utilizing the identity for well-behaved vector fields $\nabla \times \nabla \times \mathbf{A} = \nabla(\nabla \cdot \mathbf{A}) - \Delta\mathbf{A}$ yields the inhomogeneous Helmholtz equations

$$\left[\Delta + k^2\right]\mathbf{A}(\mathbf{r}) = -\mu_0\mathbf{j}(\mathbf{r}). \tag{2.21}$$
$$\left[\Delta + k^2\right]\Phi(\mathbf{r}) = -\frac{\rho(\mathbf{r})}{\varepsilon_0}. \tag{2.22}$$

with the wave number $k = \omega/c$, the speed of light $c = \sqrt{1/\varepsilon_0\mu_0}$ and the Laplace operator Δ. For a point source, these scalar equations can be solved by introducing the scalar Green's function $G_0(\mathbf{r}, \mathbf{r}')$ with $\mathbf{r}$ being the observation point and $\mathbf{r}'$ the location of the point source. To this end, the source on the right hand side of eq. (2.21) is expressed via

$\delta(\mathbf{r}-\mathbf{r}')$, giving

$$\left[\Delta + k^2\right] G_0(\mathbf{r},\mathbf{r}') = -\delta(\mathbf{r}-\mathbf{r}'), \tag{2.23}$$

A particular solution for the vector potential in eq. (2.21) then can be obtained via

$$\mathbf{A}(\mathbf{r}) = \mu_0 \int \mathbf{j}(\mathbf{r}') G_0(\mathbf{r},\mathbf{r}') dV' \tag{2.24}$$

The vector potential from a point current in x can be obtained by inserting the point current eq. (2.11) into eq. (2.24), which yields

$$\mathbf{A}(\mathbf{r}) = (i\omega)^{-1} G_0(\mathbf{r},\mathbf{r}')\mathbf{e}_x \tag{2.25}$$

Inserting this expression into eq. (2.18) gives the first column of the dyadic Green's function

$$\mathbf{G}_x(\mathbf{r},\mathbf{r}') = \left[1 + \frac{1}{k^2}\nabla\nabla\cdot\right] G_0(\mathbf{r},\mathbf{r}')\mathbf{e}_x. \tag{2.26}$$

The second and third column can be obtained equivalently for the current density in y and z direction. The full dyadic Green's function can therefore be obtained via

$$\overleftrightarrow{\mathbf{G}}(\mathbf{r},\mathbf{r}') = \left[\overleftrightarrow{\mathbf{I}} + \frac{\nabla\nabla^T}{k^2}\right] G_0(\mathbf{r},\mathbf{r}'). \tag{2.27}$$

To finally obtain an explicit form of the dyadic Green's function, an expression for the scalar Green's function G_0 is required. The exact form of G_0 can easily be derived by considering the symmetric form of the inhomogeneous Helmholtz equations. In this case, the solution G_0 of the equations only depends on the relative position $R = |\mathbf{r}-\mathbf{r}'|$ and the Laplace operator can be written in spherical coordinates via

$$\frac{1}{R}\frac{d^2}{dR^2}\left[RG_0(R)\right] + k^2 G_0(R) = -\delta(R). \tag{2.28}$$

Solving this equation by assuming the Green's function to be an oscillatory eigenfunction of d^2/dR^2 results into the following expression of the free space Green's function

$$G_0(\mathbf{r},\mathbf{r}') = \frac{\exp(ik|\mathbf{r}-\mathbf{r}'|)}{4\pi|\mathbf{r}-\mathbf{r}'|}. \tag{2.29}$$

Inserting eq. (2.29) into eq. (2.27) finally gives the dyadic Green's function for electromagnetic scattering, which can be computed straightforward in a Cartesian coordinate system, yielding

$$\overleftrightarrow{\mathbf{G}}(\mathbf{R}) = \frac{\exp(ikR)}{4\pi R}\left[\left(1 + \frac{ikR-1}{k^2R^2}\right)\overleftrightarrow{\mathbf{I}} + \frac{3-3ikR-k^2R^2}{k^2R^2}\frac{\mathbf{R}\otimes\mathbf{R}}{R^2}\right], \tag{2.30}$$

and has the form of a Hertzian dipole. Note that the observation points $\mathbf{r}$ need to be

different from $\mathbf{r}'$ due to the singularity at $\mathbf{r} = \mathbf{r}'$ of $\overleftrightarrow{\mathbf{G}}$.
For solving eq. (2.14), the remaining quantity to specify, is the current density. The goal is to obtain an expression only depending on the electric field acting on the material and the material properties such as density and a material response function. Therefore, the current density is rewritten in the following as function of charge density and local electric field.

2.1.3. Current density

A material consists of atoms with electrons, neutrons and protons. Electromagnetic scattering basically emerges from the interaction of light with the electrons. Therefore, to describe a light scattering scenario, targets can be described by a charge density distribution ρ. When the electrons of the material interact with an electric light field a dipole moment is induced, resulting in an electric current. Therefore, the current density can be defined as the product of dipole velocity $\dot{\mathbf{p}}$ and charge density via

$$\mathbf{j}(\mathbf{r}, t) = \dot{\mathbf{p}}(\mathbf{r}, t)\rho(\mathbf{r}), \tag{2.31}$$

The dipole moment $\mathbf{p}(\mathbf{r}, \mathbf{t})$ can be expressed in dependence of the local electric field $\mathbf{E}_{\text{loc}}(\mathbf{r})$ at the dipole position via

$$\mathbf{p}(\mathbf{r}, t) = \alpha(\omega)\mathbf{E}_{\text{loc}}(\mathbf{r})e^{-i\omega t}. \tag{2.32}$$

The dipole velocity then reads

$$\dot{\mathbf{p}}(\mathbf{r}, t) = -i\omega\alpha(\omega)\mathbf{E}_{\text{loc}}(\mathbf{r})e^{-i\omega t}, \tag{2.33}$$

where $\alpha(\omega)$ denotes the material specific complex polarizability. It is a measure for the amplitude and phase of the dipole moment induced in an atom by an external field of frequency ω and is proportional to the refractive index or atomic scattering factor. Note that the term $e^{-i\omega t}$ can be omitted in the following as in sec. 2.1.1. Inserting eq. (2.33) into eq. (2.31) gives the current density via

$$\mathbf{j}(\mathbf{r}) = -i\omega\alpha(\omega)\mathbf{E}_{\text{loc}}(\mathbf{r})\rho(\mathbf{r}). \tag{2.34}$$

and inserting this current density into eq. (2.14) gives the scattered electric field $\mathbf{E}_{\text{scatt}}(\mathbf{r})$ emitted from a density distribution due to interaction with the local electric field

$$\mathbf{E}_{\text{scatt}}(\mathbf{r}) = \alpha(\omega)\omega^2\mu_0 \int \overleftrightarrow{\mathbf{G}}(\mathbf{r}, \mathbf{r}')\mathbf{E}_{\text{loc}}(\mathbf{r}')\rho(\mathbf{r}')d^3\mathbf{r}'. \tag{2.35}$$

Assuming the density of the target is known, only the local electric field is the remaining quantity that needs to be defined to compute the scattered electric field. Therefore, approximations for different scattering regimes are presented and discussed in the following section.

2.2. Approximations

To solve eq. (2.35) for a given density distribution of a target, the local electric field needs to be quantified. Therefore, in this section, expressions for the local electric field are derived for different scattering regimes that are essential for this thesis. First, an approximation of the local electric field in the weak scattering regime is presented. The first Born approximation is introduced that is applicable from near- to far-field scattering. Further, for weak scattering, the small angle scattering approximation is derived. Analytical solutions for spherical and cylindrical targets are given in this regime. Further, a description for wide angle scattering is presented for far-field scattering with a simple absorption model. Last, a full solution is given by introducing the discrete dipole approximation, containing near- and far-fields for strong scattering, i. e. including absorption.

2.2.1. Near- to far-field weak scattering

In a scattering scenario with refractive indices close to unity (which is the case for hard x-ray radiation) and/or small particles the scattered electric fields are much smaller compared to the incident electric field. This case is referred to as weak scattering. In this regime, the solution of the homogeneous wave equation for free space can be applied for describing the local electric field. The homogeneous wave equation (cf. eq. (2.10)) with the incident plane wave field $\mathbf{E}_{\mathrm{inc}}(\mathbf{r}) = \hat{\mathbf{E}}_0 e^{i\mathbf{kr}}$, with the wave vector $\mathbf{k}$ and the field amplitude $\hat{\mathbf{E}}_0$ reads

$$\nabla \times \nabla \times \mathbf{E}_{\mathrm{inc}}(\mathbf{r}) - k^2 \mathbf{E}_{\mathrm{inc}}(\mathbf{r}) = 0. \tag{2.36}$$

Setting the local electric field equal to this solution $\mathbf{E}_{\mathrm{loc}}(\mathbf{r}) = \mathbf{E}_{\mathrm{inc}}(\mathbf{r})$ and inserting it into eq. (2.35) results into the scattered electric field at any position outside of the scattering region

$$\mathbf{E}_{\mathrm{scatt}}(\mathbf{r}) = \alpha(\omega)\omega^2\mu_0 \int \overleftrightarrow{\mathbf{G}}(\mathbf{r}, \mathbf{r}')\mathbf{E}_{\mathrm{inc}}(\mathbf{r}')\rho(\mathbf{r}')d^3\mathbf{r}'. \tag{2.37}$$

This weak scattering scenario also is referred to as first Born approximation. The scattered electric field in first Born approximation for a given incident electric field easily can be computed for a particle density distribution described as an ensemble of point dipoles $\rho(\mathbf{r}) = \delta(\mathbf{r} - \mathbf{r}')$ via

$$\mathbf{E}_{\mathrm{scatt}}(\mathbf{r}) = \alpha(\omega)\omega^2\mu_0 \sum \overleftrightarrow{\mathbf{G}}(\mathbf{r}, \mathbf{r}')\mathbf{E}_{\mathrm{inc}}(\mathbf{r}') \tag{2.38}$$

where the scattered electric field at a certain position is the sum of the scattered fields from each dipole of the ensemble. Thus, the weak scattering scenario can be pictured as single scattering, since each dipole only scatters once and the dipoles do not interact with each other.

2.2.2. Far-field weak scattering

The first Born approximation can be utilized to derive an analytical solution for the scattered electric field for weak and far-field scattering. To this end, the observation points have to be far out the scattering region. This is the case if the virtual detector is situated in the Fraunhofer distance $z \gg \frac{D^2}{\lambda}$, where D denotes the particle dimension, λ the wavelength and z the detector distance. In this case, the dyadic Green's function reduces to the far-field dyadic Green's function

$$\overleftrightarrow{\mathbf{G}}_{\mathrm{FF}}(\mathbf{r},\mathbf{r}') = \frac{e^{ik|\mathbf{r}-\mathbf{r}'|}}{4\pi|\mathbf{r}-\mathbf{r}'|}\left(\overleftrightarrow{\mathbf{I}} - \frac{(\mathbf{r}-\mathbf{r}')\otimes(\mathbf{r}-\mathbf{r}')}{|\mathbf{r}-\mathbf{r}'|^2}\right). \tag{2.39}$$

Equation (2.39) is inserted into the scattered electric field in first Born approximation eq. (2.37), which yields

$$\mathbf{E}_{\mathrm{scatt}}(\mathbf{r}) = \alpha(\omega)\omega^2\mu_0 \int \frac{e^{ik|\mathbf{r}-\mathbf{r}'|}}{4\pi|\mathbf{r}-\mathbf{r}'|}\left(\overleftrightarrow{\mathbf{I}} - \frac{(\mathbf{r}-\mathbf{r}')\otimes(\mathbf{r}-\mathbf{r}')}{|\mathbf{r}-\mathbf{r}'|^2}\right)\mathbf{E}_{\mathrm{inc}}(\mathbf{r}')\rho(\mathbf{r}')d^3\mathbf{r}'. \tag{2.40}$$

Assuming a linearly polarized plane wave field $\mathbf{E}_{\mathrm{inc}}(\mathbf{r}') = \hat{\mathbf{E}}_0 e^{i\mathbf{k}\mathbf{r}'}$ and considering that $z \gg x, y, x', y', z'$ the following simplification can be applied

$$\left(\overleftrightarrow{\mathbf{I}} - \frac{(\mathbf{r}-\mathbf{r}')\otimes(\mathbf{r}-\mathbf{r}')}{r^2}\right)\hat{\mathbf{E}}_0 \approx \hat{\mathbf{E}}_0. \tag{2.41}$$

This reduces eq. (2.40) to

$$\mathbf{E}_{\mathrm{scatt}}(\mathbf{r}) = \alpha(\omega)\omega^2\mu_0\hat{\mathbf{E}}_0 \int \frac{e^{ik|\mathbf{r}-\mathbf{r}'|}}{4\pi|\mathbf{r}-\mathbf{r}'|}\rho(\mathbf{r}')e^{i\mathbf{k}\mathbf{r}'}d^3\mathbf{r}', \tag{2.42}$$

Further, in the far-field region the following relation holds

$$\begin{aligned}
|\mathbf{r}-\mathbf{r}'| &= \sqrt{(\mathbf{r}-\mathbf{r}')^2}, \\
&= \sqrt{r^2 + r'^2 - 2\mathbf{r}\mathbf{r}'}, \\
&= r\sqrt{1 - \frac{2\mathbf{r}\mathbf{r}'}{r^2}}, \\
&= r(1 - \frac{\mathbf{r}\mathbf{r}'}{r^2}), \\
&= r - \hat{\mathbf{r}}\mathbf{r}'.
\end{aligned}$$

In the second line r'^2 can be omitted, since $r \gg r'$ and from the third to the fourth line a Taylor expansion is performed around the argument $2\mathbf{r}\mathbf{r}'/r^2$. The vector pointing in the

direction of the observation point is denoted by the unity vector $\hat{\mathbf{r}} = \mathbf{r}/r$. The outgoing wave vector points in the same direction and is $\mathbf{k}_{\text{out}} = k\hat{\mathbf{r}}$ for elastically scattered photons. Inserting this relation into eq. (2.42) yields

$$\mathbf{E}_{\text{scatt}}(\mathbf{k}, \mathbf{k}_{\text{out}}) = \alpha(\omega)\omega^2\mu_0 \frac{\hat{\mathbf{E}}_0 e^{ikr}}{4\pi r} \int e^{-i\mathbf{k}_{\text{out}}\mathbf{r}'} \rho(\mathbf{r}') e^{i\mathbf{k}\mathbf{r}'} d^3\mathbf{r}'. \tag{2.43}$$

Further, introducing the momentum transfer between incoming and outgoing (scattered) light

$$\mathbf{q} = \mathbf{k}_{\text{out}} - \mathbf{k} \tag{2.44}$$

reduces the equation to the so-called Born result

$$\mathbf{E}_{\text{scatt}}(\mathbf{q}) = \alpha(\omega)\omega^2\mu_0 \frac{\hat{\mathbf{E}}_0 e^{ikr}}{4\pi r} \int \rho(\mathbf{r}') e^{-i\mathbf{q}\mathbf{r}'} d^3\mathbf{r}'. \tag{2.45}$$

It becomes obvious that the scattered electric field is proportional to the 3D Fourier transform of the 3D particle density $\int \rho(\mathbf{r}') e^{-i\mathbf{q}\mathbf{r}'} d^3\mathbf{r}' = \mathcal{FT}[\rho(\mathbf{r}')]$. Absorption is not included but all 3D information about the particle is. This equation can be even more simplified in the limit of small scattering angles, which is shown in the following section.

Small angle x-ray scattering

To derive the scattered electric field for small angle x-ray scattering (SAXS), starting point is the Born result for weak scattering (eq. (2.45)) with the prefactors condensed to $c_0 = \alpha(\omega)\omega^2\mu_0$

$$\mathbf{E}_{\text{scatt}}(\mathbf{q}) = c_0 \frac{\hat{\mathbf{E}}_0 e^{ikr}}{4\pi r} \int \rho(x', y', z') e^{-iq_x x'} e^{-iq_y y'} e^{-iq_z z'} d^3\mathbf{r}'. \tag{2.46}$$

An incoming plane wave that propagates in z-direction with the incoming wave vector being $\mathbf{k} = (0, 0, k)$ is considered. The momentum transfer then yields (cf. eq. (2.44))

$$\mathbf{q} = \frac{k}{r} \begin{pmatrix} x \\ y \\ z \end{pmatrix} - \begin{pmatrix} 0 \\ 0 \\ k \end{pmatrix} \tag{2.47}$$

The z-component of $\mathbf{q}$ then is approximately zero for small scattering angles, since $r \approx z$. For this case, the integration can be performed with respect to z' in eq. (2.46) over the charge density, resulting in a charge density projected onto the x-y-plane

$$\int \rho(\mathbf{r}') dz' = \rho_p(x', y') \tag{2.48}$$

Inserting this into eq. (2.46) leads to

$$\mathbf{E}_{\text{scatt}}(q_x, q_y) = c_0 \frac{\hat{\mathbf{E}}_0 e^{ikr}}{4\pi r} \int \rho_p(x', y') e^{-i(q_x x' + q_y y')} dx' dy' = c_0 \frac{\hat{\mathbf{E}}_0 e^{ikr}}{4\pi r} \mathcal{FT}\left[\rho_p(x, y)\right], \quad (2.49)$$

where $\mathcal{FT}\left[\rho_p(x, y)\right]$ is the 2D Fourier transform of the projected particle density. Hence, for SAXS the diffraction pattern is proportional to the squared amplitude of the Fourier transform of the particle density projected onto the plane perpendicular to the laser propagation direction. Note that this leads to the possibility of multiple particle orientations resulting into the same diffraction pattern.
In the SAXS regime, iterative phase retrieval algorithms can be applied to obtain the projected particle density from the diffraction patterns. They are based on alternating Fourier transforms (FT) and inverse FT of diffraction pattern and particle density. To reach convergence constraints on particle density and scattered electric field are applied in each iteration. A phase retrieval algorithm is outlined in more detail in appendix D.
Further, for simple and symmetric shapes analytical solutions for SAXS can be found. For this thesis, the solutions for a sphere (cf. chapter 5) and jet (cf. chapter 4) are important and are derived along a one-dimensional detector trace in the following.

SAXS for a sphere

Considering only a one-dimensional detector trace along the x-axis with $y = 0$ (i. e. $q_y = 0$), the scattered electric far-field (eq. (2.49)) becomes

$$\mathbf{E}_{\text{scatt}}(q_x) = c_0 \frac{\hat{\mathbf{E}}_0 e^{ikr}}{4\pi r} \int \rho_p(x') e^{-i(q_x x')} dx'. \quad (2.50)$$

It can be seen that the expression only depends on the particle density projected onto z and y with $\rho_p(x') = \int \rho(x', y', z') dy' dz'$. The density of a homogeneous sphere with number density n_a and radius R projected onto z and y can be described via $\rho_p(x') = 4n_a[R^2 - x'^2]$. This is clarified in fig. 2.1 for the projection onto the z-axis. The same geometrical consideration holds for the projection onto the y-axis. Inserting this expression into eq. (2.50) yields

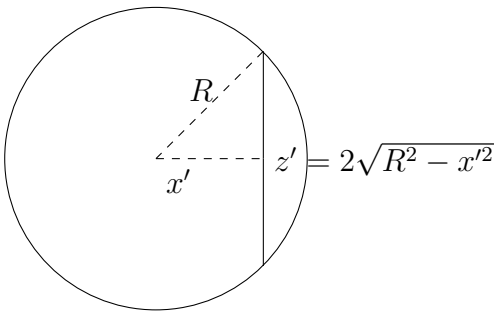

Figure 2.1.: Sketch of the projection of a circle onto the z-axis. The projection in dependence on the position x' and the circle radius R is $z' = 2\sqrt{R^2 - x'^2}$.

$$\mathbf{E}_{\text{scatt}}(q_x) = n_a c_0 \frac{\hat{\mathbf{E}}_0 e^{ikr}}{\pi r} \int (R^2 - x'^2) e^{-iq_x x'} dx'. \quad (2.51)$$

Performing the integration from $-R$ to R gives

$$\mathbf{E}_{\text{scatt}}(q_x) = 4n_a c_0 \frac{\hat{\mathbf{E}}_0 e^{ikr}}{\pi r} \frac{\sin(q_x R) - q_x R\cos(q_x R)}{q_x^3}, \tag{2.52}$$

The measured intensity is defined as $I = \frac{c\epsilon_0}{2}|E|^2$ and inserting eq. (2.52) yields

$$I(q_x) = 2n_a c\epsilon_0 c_0 \frac{\hat{\mathbf{E}}_0 e^{ikr}}{\pi r} \frac{[\sin(q_x R) - q_x R\cos(q_x R)]^2}{q_x^6}, \tag{2.53}$$

Since a sphere is radially symmetric, the scattered intensity on the detector is as well. Therefore, to obtain the two-dimensional diffraction pattern for a spherical target q_x can be interchanged with the momentum transfer perpendicular to the laser propagation direction $q_x \to q_\perp = \sqrt{q_x^2 + q_y^2}$. In this case, the scattered intensity becomes

$$I(q_\perp) = 2n_a c\epsilon_0 c_0 \frac{\hat{\mathbf{E}}_0 e^{ikr}}{\pi r} \frac{[\sin(q_\perp R) - q_\perp R\cos(q_\perp R)]^2}{q_\perp^6}, \tag{2.54}$$

Considering this periodic function to be maximal for $q = (n+1)\pi/R$, with n being an integer number, the envelope of the intensity trace is

$$I_{\text{env}}(q_\perp) = 2n_a c\epsilon_0 c_0 \frac{\hat{\mathbf{E}}_0 e^{ikr}}{4\pi r} \frac{R^2}{q_\perp^4}. \tag{2.55}$$

Thus, the scattered intensity drops with $\propto q_\perp^{-4}$, which is called Porod's law [125]. A typical scattering detector can resolve intensities up to five orders of magnitude, which means that only scattered light up to a certain momentum transfer can be recorded on the detector. Considering that the momentum transfer is $q = \frac{4\pi}{\lambda}\sin(\theta/2)$, with the wavelength λ and the scattering angle θ shows that for small wavelength, i. e. large photon energies, scattering images are confined to small scattering angles. Larger scattering angles, only can be resolved when utilizing longer wavelength.

SAXS for a jet

The density of a homogeneous jet aligned along x, i. e. a cylinder with number density n_a and radius R, projected in z can be described via $\rho_p(x', y') = \int 2n_a\sqrt{R^2 - y'^2}dx'$ (cf. fig. 2.2). Inserting this expression into eq. (2.49) and considering only a one-dimensional detector trace with $x = 0$ yields

$$\mathbf{E}(q_y) = 2n_a c_0 \frac{\hat{\mathbf{E}}_0 e^{ikr}}{4\pi r} \int \sqrt{R^2 - y'^2} e^{-iq_y y'} dx' dy', \tag{2.56}$$

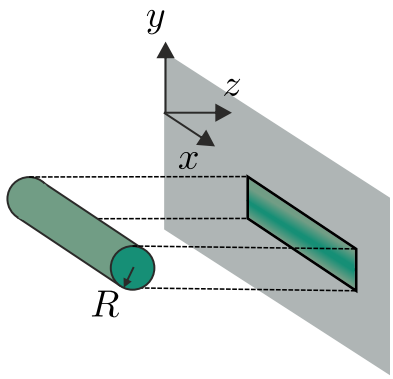

Figure 2.2.: Cylindric jet projected onto x-y-plane.

Performing the x' integration over the jet length l gives

$$\mathbf{E}(q_y) = 2ln_a c_0 \frac{\hat{\mathbf{E}}_0 e^{ikr}}{4\pi r} \int \sqrt{R^2 - y'^2} e^{-iq_y y'} dy'. \tag{2.57}$$

The Integration over y' then results into

$$\mathbf{E}(q_y) = 2ln_a c_0 \frac{\hat{\mathbf{E}}_0 e^{ikr}}{4\pi r} \frac{\pi R J_1(q_y R)}{q_y}, \tag{2.58}$$

where J_1 denotes the Bessel function of first kind. The measured intensity $I = \frac{c\epsilon_0}{2}|E|^2$ then yields

$$I(q_y) = (ln_a c_0)^2 c\epsilon_0 \frac{|\hat{\mathbf{E}}_0|^2}{8\pi^2 r^2} \frac{[J_1(q_y R)]^2}{q_y^2} \tag{2.59}$$

The Bessel function $J_1(t)$ for $t \gg 1$ can be approximated by

$$J_\nu(t) = \sqrt{\frac{2}{\pi t}} \cos(t - \pi/2 - \pi/4). \tag{2.60}$$

Inserting the above expression with $t = q_y R$ into eq. (2.59), the intensity for non-zero q_y and large R yields

$$I(q_y) = (ln_a c_0)^2 c\epsilon_0 \frac{|\hat{\mathbf{E}}_0|^2}{4\pi^3 r^2 R} \frac{\cos^2(q_y R - 3/4\pi)}{q_y^3} \tag{2.61}$$

This periodic function is maximal for $\cos(q_y R - 3/4\pi) = 1$. Thus, the envelope of the intensity trace is

$$I_{\text{env}}(q_y) = (ln_a c_0)^2 c\epsilon_0 \frac{|\hat{\mathbf{E}}_0|^2}{4\pi^3 r^2 R} \frac{R}{q_y^3}, \tag{2.62}$$

The intensity drops with $\propto q_y^{-3}$, thus, is visible up to larger scattering angles for the same wavelength compared to scattering by a sphere.

Wide angle x-ray scattering

To include wide scattering angles in the computation of the diffraction patterns, the multislice Fourier transform method (MSFT) is a convenient approach [10]. Starting point for its derivation is the Born result (cf. eq. (2.45))

$$\mathbf{E}_{\text{scatt}}(\mathbf{q}) = c_0 \frac{\hat{\mathbf{E}}_0 e^{ikr}}{4\pi r} \int \rho(x', y', z') e^{-i(q_x x' + q_y y' + q_z z')} dx' dy' dz'. \tag{2.63}$$

Only a single slice j of the object with small thickness $\Delta z' = z'_{j+1} - z'_j$ is considered. The particle density in this slice can be assumed to be constant in z', thus, being only dependent on x' and y'. Then, applying the mean value theorem, the integration over z' for the jth slice simplifies to $\int_{z'_j}^{z'_{j+1}} e^{-iq_z z'} dz' = \Delta z' e^{-iq_z z'_j}$, where $z'_j = j\Delta z$. Inserting this into eq. (2.63), the scattered electric field generated by a single particle slice yields

$$\mathbf{E}_{\text{scatt,j}}(\mathbf{q}) = c_0 \Delta z' \frac{\hat{\mathbf{E}}_0 e^{ikr}}{4\pi r} \int \rho_j(x', y') e^{-i(q_x x' + q_y y' + q_z z'_j)} dx' dy', \tag{2.64}$$

$$= c_0 \Delta z' \frac{\hat{\mathbf{E}}_0 e^{ikr}}{4\pi r} \mathcal{FT}[\rho_j(x', y')] e^{-iq_z z'_j}. \tag{2.65}$$

To obtain the total scattered field from the object, the sum of the scattered fields from all slices is computed via

$$\mathbf{E}_{\text{scatt}}(\mathbf{q}) = c_0 \Delta z' \frac{\hat{\mathbf{E}}_0 e^{ikr}}{4\pi r} \sum_j \mathcal{FT}\left[\rho_j(x', y')\right] e^{-iq_z z'_j}. \tag{2.66}$$

Hence, the scattered electric field is the phase-correct sum of the Fourier transforms of each slice of the particle density. Equation (2.66) is only applicable to weak scattering scenarios where absorption is negligible. However, by utilizing Lambert-Beers-law, absorption can be introduced into the equation. Therefore, the incident electric field amplitude reaching each slice is attenuated according to the material dependent absorption length l_{abs} via

$$\hat{\mathbf{E}}_0(x', y', z_j) = \hat{\mathbf{E}}_0(z_0) e^{-z_j \bar{\rho}_{0j}(x', y') l_{\text{abs}}}, \tag{2.67}$$

with the unattenuated incident field amplitude $\hat{\mathbf{E}}_0(z_0)$ and $\bar{\rho}_{0j}(x', y') = \sum_{k=0}^{j} \rho(x', y', z_k)$. Inserting this into eq. (2.66) gives

$$\mathbf{E}_{\text{scatt}}(\mathbf{q}) = c_0 \Delta z' \frac{\hat{\mathbf{E}}_0(z_0) e^{ikr}}{4\pi r} \sum_{j=0} \left(e^{-z_j \bar{\rho}_{0j}(x', y') l_{\text{abs}}} \mathcal{FT}\left[\rho_j(x, y)\right] e^{-iq_z z_j} \right). \tag{2.68}$$

This very simplified absorption model does not include backscattering, which only can be included when considering multiple scattering scenarios. A method for solving the scattering equation (2.35) with including these effects is derived in the following section.

2.2.3. Near- to far-field strong scattering

For the scenario of strong scattering, where incident and scattered field are on the same order, both fields need to be taken into account for the computation of the local electric field in eq. (2.35). This is done by adding inhomogeneous and homogeneous solution of the wave equation eqs. (2.35) and (2.36) yielding the Born series for the local electric field as

$$\mathbf{E}_{\mathrm{loc}}(\mathbf{r}) = \mathbf{E}_{\mathrm{inc}}(\mathbf{r}) + \mathbf{E}_{\mathrm{scatt}}(\mathbf{r}) \tag{2.69}$$

$$= \mathbf{E}_{\mathrm{inc}}(\mathbf{r}) + \alpha(\omega)\omega^2\mu_0 \int \overleftrightarrow{\mathbf{G}}(\mathbf{r},\mathbf{r}')\mathbf{E}_{\mathrm{loc}}(\mathbf{r}')\rho(\mathbf{r}')d^3\mathbf{r}'. \tag{2.70}$$

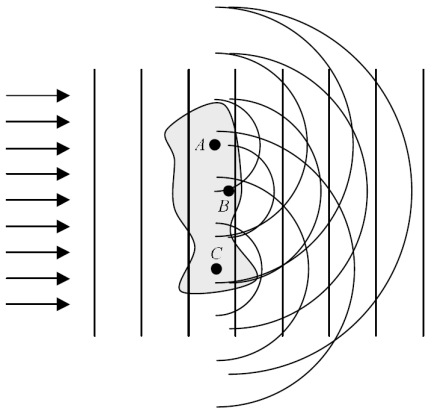

Figure 2.3.: Schematic presentation of discrete dipole approximation with three representative discrete point dipoles A, B and C interact with an incoming plane wave, radiating spherical waves. Figure taken from [93].

The local electric field is present on left and right-hand side of the equation, thus, the Born series needs to be solved self-consistently. The discrete dipole approximation (DDA) [99, 31] is a very powerful tool to accomplish this goal. In this method, the particle is described as an ensemble of discrete point dipoles. For such a target, the scattering scenario can be illustrated in a physical picture by a multiple scattering scenario. In such a scenario each dipole of the ensemble of discrete point dipoles emits a spherical wave induced by the incident field. This corresponds to the first scattering event. Such a scenario is depicted in fig. 2.3. The generated spherical waves then induce new scattered fields at all dipole positions. This corresponds to a second scattering event. These new scattered fields induce a third scattering event and so on. This physical picture indicates that it is convenient to solve the Born series in an iterative approach, where in each step another scattering event is taken into account. To this end, the DDA approach is described in more detail in the following. Therefore, first the charge density for an ensemble of point charges is introduced into the Born series to derive the scattered and local fields in the discrete dipole approximation. Second, an iterative approach for solving the DDA problem is presented.

Discrete dipole approximation

The discrete dipole approximation (DDA) approximates the particle density by an ensemble of discrete point dipoles. Thus, the charge density can be described with a δ-function via

$$\rho(\mathbf{r}') = \delta(\mathbf{r}' - \mathbf{r}_n), \tag{2.71}$$

where $\mathbf{r}_n$ denotes the dipole position. The scattered field (eq. (2.35)) from such a density distribution is

$$\mathbf{E}_{\text{scatt}}(\mathbf{r}) = \alpha(\omega)\omega^2\mu_0 \int \overleftrightarrow{\mathbf{G}}(\mathbf{r}, \mathbf{r}')\mathbf{E}_{\text{loc}}(\mathbf{r}')\delta(\mathbf{r}' - \mathbf{r}_n)d^3\mathbf{r}'. \tag{2.72}$$

The scattered electric field outside the scattering region can be obtained by integration over all discrete particle positions

$$\mathbf{E}_{\text{scatt}}(\mathbf{r}) = \alpha(\omega)\omega^2\mu_0 \sum_n \overleftrightarrow{\mathbf{G}}(\mathbf{r}, \mathbf{r}_n)\mathbf{E}_{\text{loc}}(\mathbf{r}_n). \tag{2.73}$$

For the scattered electric field inside the scattering domain at a certain particle position $\mathbf{r}_n$ the scattered field from this dipole has to be excluded. The scattered field then reads

$$\mathbf{E}_{\text{scatt}}(\mathbf{r}_j) = \alpha(\omega)\omega^2\mu_0 \sum_{n\neq j} \overleftrightarrow{\mathbf{G}}(\mathbf{r}_j, \mathbf{r}_n)\mathbf{E}_{\text{loc}}(\mathbf{r}_n). \tag{2.74}$$

Then the local electric field at a certain particle position can be found by inserting eq. (2.74) into eq. (2.70), yielding

$$\mathbf{E}_{\text{loc}}(\mathbf{r}_j) = \mathbf{E}_{\text{inc}}(\mathbf{r}_j) + \alpha(\omega)\omega^2\mu_0 \sum_{n\neq j} \overleftrightarrow{\mathbf{G}}(\mathbf{r}_j, \mathbf{r}_n)\mathbf{E}_{\text{loc}}(\mathbf{r}_n). \tag{2.75}$$

Solving this equation is required to finally compute the scattered electric field at the detector. However, first, an expression for the complex polarizability needs to be found. For discrete point dipoles, it is convenient to describe it in terms of the frequency-dependent material specific atomic scattering factor $f^0(\omega)$ via

$$\alpha(\omega) = -f^0(\omega)\frac{e^2}{m_e\omega^2}, \tag{2.76}$$

with the electron charge e and mass m_e. The complex atomic scattering factor can be taken from tables [57] or can be interchanged with the complex refractive index $n(\omega)$ via the Clausius-Mossotti relation

$$f^0(\omega) = \frac{3m_\text{e}\omega^2\varepsilon_0}{n_\text{a}\, e^2}\left(\frac{1 - n(\omega)^2}{n(\omega)^2 + 2}\right), \tag{2.77}$$

where n_a denotes the atomic number density. Now, every quantity in eq. (2.74) is known, except for the local electric field. In the following an iterative approach is presented that allows for the self-consistent computation of the local electric field.

Iterative approach for solving the Born series

For solving the DDA problem an expression for the local electric field is required. To this end, first, the local electric field in eq. (2.75) is rewritten via

$$\mathbf{E}_\mathrm{loc}(\mathbf{r}_j) = \mathbf{E}_\mathrm{inc}(\mathbf{r}_j) + \sum_{k\neq j} \mathbf{E}_\mathrm{scatt}(\mathbf{r}_j, \mathbf{r}_k). \tag{2.78}$$

with the scattered field from the kth dipole acting on the jth dipole

$$\mathbf{E}_\mathrm{scatt}(\mathbf{r}_j, \mathbf{r}_k) = -\frac{e^2\mu_0 f^0(\omega)}{m_e} \overleftrightarrow{\mathbf{G}}(\mathbf{r}_j, \mathbf{r}_k)\mathbf{E}_\mathrm{loc}(\mathbf{r}_k). \tag{2.79}$$

Now, the local electric field can be obtained in an iterative approach. Starting the iteration with the local electric fields set to zero gives

$$\mathbf{E}^0_\mathrm{loc}(\mathbf{r}_j) = \mathbf{E}_\mathrm{inc}(\mathbf{r}_j). \tag{2.80}$$

for the 0th iteration for the jth dipole. This result then is inserted into the eq. (2.79) and ultimately in eq. (2.78) to update the local electric fields. The goal is to repeat this until the local electric field converges to a certain value. However, this solution methods already diverges for weak scattering scenarios, as is shown in chp. 3.1. An approach to stabilize the convergence was already introduced by Purcell and Pennypacker, who first described the discrete dipole approximation [99]. A mixing parameter g is introduced that steers fraction of local electric field from current and previous iteration via

$$\mathbf{E}^{i+1}_\mathrm{loc}(\mathbf{r}_j) = g\left[\mathbf{E}_\mathrm{inc}(\mathbf{r}_j) + \sum_{k\neq j} \mathbf{E}^i_\mathrm{scatt}(\mathbf{r}_j, \mathbf{r}_k)\right] + (1-g)\,\mathbf{E}^i_\mathrm{loc}(\mathbf{r}_j), \tag{2.81}$$

where i is the number of iteration and

$$\mathbf{E}^i_\mathrm{scatt}(\mathbf{r}_j) = \alpha(\omega)\omega^2\mu_0 \sum_{n\neq j} \overleftrightarrow{\mathbf{G}}(\mathbf{r}_j, \mathbf{r}_n)\mathbf{E}^i_\mathrm{loc}(\mathbf{r}_n). \tag{2.82}$$

For $g = 1$ the Born series result is obtained, for $g = 0$ only the local field from the last iteration is taken into account. In chp. 3.1, a mixing parameter g is introduced to efficiently solve this iterative mixing approach. The discrete dipole approximation introduced here represents a numerical model for describing scattering scenarios of arbitrarily shaped particles including absorption effects.

method	small angles	large angles	absorption included	atomic resolution
SAXS	x			
MSFT	x	x	(x)	
DDA	x	x	x	x

Table 2.1.: Regimes to which different forward fit methods can be applied. (x) denotes that the absorption model in MSFT is simplified.

Synopsis

So far, three numerical methods for computing diffraction patterns from known density distributions have been derived. For weak scattering in the far-field at small scattering angles (SAXS), the diffraction pattern can be computed by performing the Fourier transform (FT) of the projected particle density. For weak scattering at large scattering angles, the multislice Fourier transform method (MSFT) is applicable. A simple description of absorption is included by Beer-Lamberts-law. For strong scattering, where absorption is not negligible, the discrete dipole approximation (DDA) has been introduced. It is applicable to near- and far-field scattering scenarios. The numerical methods presented can be implemented to forward fit scattering data, i. e. calculate diffraction patterns for a set of known model shapes and compare them to the experimental diffraction patterns. Further, especially MSFT and DDA are applicable to investigate the effect of different laser parameters onto the scattering images, such as wavelength and pulse duration, as done in chapter 3. Further, MSFT and DDA are utilized for forward fitting diffraction patterns by helium nanodroplets and hydrogen jets (chps. 4 and 5). Table 2.1 provides an overview for which regimes the different methods are applicable.
The drawback of these approaches is that for comparison to experimental data, already a good selection of model shapes has to be utilized to find the correct shape to a diffraction pattern. Another approach, that shortly was addressed in this chapter, is the iterative phase retrieval applicable to weak scattering scenarios. Phase retrieval algorithms can be utilized to gain the particle density from a diffraction pattern without prior knowledge about the particle shape and structure. Chapter 6 is considered with three-dimensional reconstruction of particle shapes via phase retrieval.

3. Influence of pulse duration and wavelength on single-shot diffraction patterns

In this chapter, the influence of different wavelengths and different pulse durations on the diffraction pattern is investigated and discussed. For the theoretical investigation of the effect of different wavelengths onto the diffraction pattern, the utilized numerical model has to cover a wide range of scenarios. At large wavelength, absorption effects are important and need to be taken into account. For short wavelength, e. g. in the hard x-ray regime, sub-nanometer length scales need to be resolved. The discrete dipole approximation (DDA, cf. chp. 2.2.3) meets these requirements. In this chapter, therefore first, the discrete dipole approximation with a complex scaling ansatz is implemented (CSDDA - complex scaling DDA). The CSDDA then is utilized to compute diffraction patterns for a test shape, an icosahedron, in different scattering scenarios. The second part of this chapter is dedicated to investigate the influence of wavelength on diffraction patterns. To this end, diffraction patterns obtained by scattering from extreme ultraviolet to soft and hard x-ray radiation are compared to each other. Comparing the CSDDA numerical results to MSFT diffraction patterns (multislice Fourier transform method, cf. chp. 2.2.2) allows for investigation of absorption effects at the same time. Third, the influence of different pulse durations is explored by comparing CSDDA diffraction patterns computed for different pulse durations and laser wavelength. The results presented in this chapter are published in [117].

3.1. Complex Scaling Discrete Dipole Approximation

In the following, the DDA problem derived in chp. 2.2.3 is solved. Therefore, first, an iterative mixing approach with complex scaling is presented (complex scaling discrete dipole approximation, CSDDA). Second, a coarse graining is introduced by merging the point dipoles to so-called super-particles to solve the CSDDA for larger wavelength. Last, the numerical model is benchmarked for a spherical target utilizing Mie theory.

3.1.1. Theoretical framework of the CSDDA

Starting point for the derivation is eq. (2.81) that describes the local electric field $\mathbf{E}_{\mathrm{loc}}$ acting on the jth point dipole of an ensemble of N point dipoles that interact with an incident laser beam $\mathbf{E}_{\mathrm{inc}}$ via

$$\mathbf{E}^{i+1}_{\mathrm{loc}}(\mathbf{r}_j) = (1-g)\,\mathbf{E}^{i}_{\mathrm{loc}}(\mathbf{r}_j) + g\left[\mathbf{E}_{\mathrm{inc}}(\mathbf{r}_j) + \mathbf{E}^{i}_{\mathrm{scatt,sum}}(\mathbf{r}_j,\mathbf{r}_k)\right]. \tag{3.1}$$

The iteration number is denoted by i, g is the mixing parameter. The latter term reflects the incident field and the scattered field from all other dipoles

$$\mathbf{E}_{\mathrm{scatt,sum}}(\mathbf{r}_j) = -\sum_{k\neq j}^{N} \frac{e^2\mu_0 f^0(\omega)}{m_e} \overleftrightarrow{\mathbf{G}}(\mathbf{r}_j,\mathbf{r}_k)\mathbf{E}_{\mathrm{loc}}(\mathbf{r}_k). \tag{3.2}$$

In the original DDA description by Purcell and Pennypacker the mixing parameter g has been chosen to be a real quantity and set to a constant value [99]. The iteration procedure is started by setting the local electric field equal to the incident electric field for iteration $i = 0$.

$$\mathbf{E}^0_{\mathrm{loc}}(\mathbf{r}_j) = \mathbf{E}_{\mathrm{inc}}(\mathbf{r}_j). \tag{3.3}$$

This zeroth-order solution is now used as the initial guess $\mathbf{E}^0_{\mathrm{loc}}$ for the iterative procedure defined via eqs. (3.1) and (3.2). The updated local fields are then utilized to update the scattered fields iteratively. The iteration sequence can be terminated as soon as the error expressed via R falls below a certain limit $R \leq \epsilon$. A reasonable choice for the residuum is the sum of squared differences between old and new solution of the local electric fields

$$R^{i+1} = \sqrt{\frac{\sum_j |\mathbf{E}_{\mathrm{inc}}(\mathbf{r}_j) + \mathbf{E}^{i+1}_{\mathrm{scatt,sum}}(\mathbf{r}_j) - \mathbf{E}^{i+1}_{\mathrm{loc}}(\mathbf{r}_j)|^2}{N}}. \tag{3.4}$$

The convergence of the mixing scheme can be highly accelerated by adapting the mixing parameter g in each iteration. Considering the residuum after a given mixing step as the target observable, the optimal mixing parameter g can be obtained from a minimization problem. For the derivation, eq. (3.1) is inserted into eq. (3.4), which then clearly shows the dependence of the residuum R^{i+1} on the mixing parameter of the previous iteration g^i

$$R^{i+1} = \sqrt{\frac{\sum_j \left|g^i\mathbf{X}^i_j + \mathbf{Y}^i_j\right|^2}{N}}, \tag{3.5}$$

where

$$\begin{aligned}
\mathbf{X}^i_j &= \mathbf{E}^i_{\mathrm{loc}}(\mathbf{r}_j) - \mathbf{E}_{\mathrm{inc}}(\mathbf{r}_j) - 2\mathbf{E}^i_{\mathrm{scat,sum}}(\mathbf{r}_j) + \underbrace{\sum_{k\neq j} \overleftrightarrow{\mathcal{G}}_{jk}\left[\mathbf{E}_{\mathrm{inc}}(\mathbf{r}_k) + \mathbf{E}^i_{\mathrm{scat,sum}}(\mathbf{r}_k)\right]}_{\mathbf{z}^{i+1}_j}, \\
\mathbf{Y}^i_j &= -\mathbf{E}^i_{\mathrm{loc}}(\mathbf{r}_j) + \mathbf{E}_{\mathrm{inc}}(\mathbf{r}_j) + \mathbf{E}^i_{\mathrm{scat,sum}}(\mathbf{r}_j),
\end{aligned} \tag{3.6}$$

with $\overleftrightarrow{\mathcal{G}}_{jk} = \frac{e^2\mu_0 f^0(\omega)}{m_e}\overleftrightarrow{\mathbf{G}}(\mathbf{r}_j,\mathbf{r}_k)$. For the optimal mixing parameter, the first derivative of

the residuum (eq. (3.5)) with respect to the mixing parameter has to vanish

$$\frac{\partial R^{i+1}}{\partial g^i} = 0. \tag{3.7}$$

Since $\mathbf{X}$ and $\mathbf{Y}$ are complex quantities, also the mixing parameter can, in general be complex. However, historically, only real mixing parameters were considered, for which optimal reduction of the residuum is achieved for

$$g^i_{\text{opt,real}} = -\frac{\sum_j \left[(\mathbf{X}^i_j)^* \mathbf{Y}^i_j + \mathbf{X}^i_j (\mathbf{Y}^i_j)^*\right]}{2\sum_j |\mathbf{X}^i_j|^2}. \tag{3.8}$$

If, however, the mixing parameter is allowed to be complex, optimal error reduction is found for

$$g^i_{\text{opt,complex}} = -\frac{\sum_j \left[(\mathbf{X}^i_j)^* \mathbf{Y}^i_j\right]}{\sum_j |\mathbf{X}^i_j|^2}. \tag{3.9}$$

Prior to the comparison of the convergence behavior with optimized real or complex mixing factors, it is important to check if the determination of the mixing parameter itself requires additional numerical effort. Interestingly, no additional effort is needed, since fields computed for calculating g^i can be utilized to construct the fields $\mathbf{E}^{i+1}_{\text{loc}}$ (cf. eq. (3.1)) and $\mathbf{E}^{i+1}_{\text{scatt,sum}}$ via

$$\mathbf{E}^{i+1}_{\text{scat,sum}}(\mathbf{r}_j) = g^i \mathbf{Z}^{i+1}_j + \left(1 - g^i\right) \mathbf{E}^i_{\text{scat,sum}}(\mathbf{r}_j). \tag{3.10}$$

The calculation of the $\mathbf{Z}$ field (defined in eq. (3.6)), however, is computationally very expensive. The effort for the computation is $\propto N^2$, since the interaction between all dipoles needs to be taken into account. The effort could be reduced by implementing a regular equidistant grid and accelerate the calculation by FFT methods. Nevertheless, for a construction of particles for example with a certain crystal lattice, it is convenient to be able to distribute dipoles on a grid that is not equidistant. Hence, in the following the acceleration is not utilized.

To test the efficiency of CSDDA, first the simplest test case one could think of is investigated. The local electric field of two identical point scatterers with $f^0 = 30$, separated by a distance of $d = 2\,\text{nm}$ along the x-axis, is computed for an incident plane wave with $k = 1\,\text{nm}^{-1}$ propagating along the z-axis and polarized in x direction. The setup is sketched in fig. 3.1a. It is sufficient to only examine the local field of one of the dipoles, since the problem is completely symmetric and the fields are equal at the two positions. For this test case, the analytical solution can easily be calculated and is used as a benchmark. The local fields are computed for a real scaling (eq. (3.8), red) and a complex scaling (eq. (3.9), blue) mixing parameter for different iterations. The results are depicted in fig. 3.1b. Additionally, the local field for the Born series result ($g^i = 1$, green) is

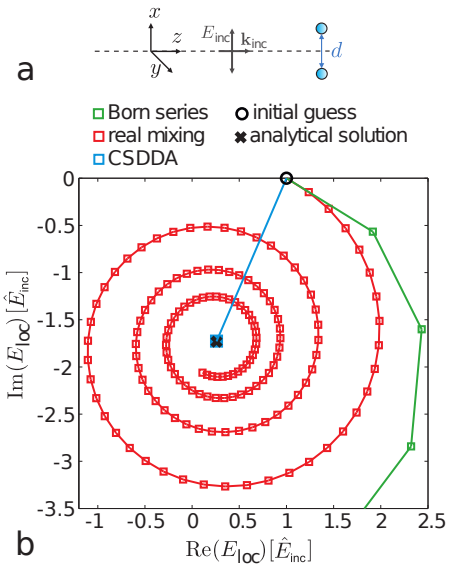

Figure 3.1.: a) Sketch of scenario to benchmark and test efficiency of complex scaling discrete dipole approximation. Two point dipole scatterers with $f = 30$ separated by $d = 2\,\mathrm{nm}$ (along the x-axis) are illuminated by an incident plane wave laser field ($k = 1\,\mathrm{nm}^{-1}$) that is polarized along the x-direction and propagates along the z-direction. b) Evolution of real and imaginary parts of the x-component of the local field for several iterations with the optimal real and optimal complex (CSDDA) mixing and the full Born series. The initial guess ($E_{\mathrm{loc}} = E_{\mathrm{inc}}$) and the analytical solution are indicated by a circle and a cross, respectively. Figure published in [117].

shown. It can be seen that the Born series already diverges for this simple test case, the real scaling result converges to the analytical result, however, more than 100 iterations are necessary. The complex scaling result, on the other hand, only needs a single iteration to reach the analytical solution. Therefore, it is obvious, that the implementation of the complex scaling is much more efficient than the original proposition of a real scaling. The advantage of the complex scaling discrete dipole approximation is that it is very simple to implement and a very intuitive approach to solve the discrete dipole approximation. However, there are more complex and sophisticated algorithms such as the Krylov subspace methods that can be applied in a wider regime of particle sizes and wavelengths than CSDDA [142]. A comparison of CSDDA to the well-established Krylov-subspace methods can be found in the appendix A.

So far, the DDA approach has been discussed for the case of atomic resolution, where each dipole represents an individual atom. However, for larger wavelength or very large particles, it is desirable to decrease the number of dipoles to reduce the computational costs (that scale with N^2) by merging them to super-particles that represent multiple atoms. This is done in the following subsection.

3.1.2. Super-particles and benchmark

Super-particles have a larger scattering strength than a single atom. To account for this the atomic scattering factor is adjusted via

$$\tilde{f}^0 = \frac{N}{N_{\mathrm{at}}} f^0, \tag{3.11}$$

with the number of effective particles N and the particle number N_{at} for atomic resolution. The applicability of this description is tested in the following.

A suitable benchmark case for a larger object is the scattering by homogeneous spheres. The solution of the Maxwell's equations for this scenario is given by the Mie solution [84]. Therefore, the scattering problem is solved using spherical vector harmonics, described in more detail in app. B. For the benchmark, the scattered fraction, which is the number of photons dN_{scat} scattered into an element solid angle $d\Omega$ relative to the number of photons scattered into the geometrical cross section of the target N_{inc}, is computed via

$$S(\Theta) = \frac{dN_{\mathrm{scat}}}{N_{\mathrm{inc}} d\Omega} = \frac{D^2 \mathbf{I}^2_{\mathrm{scatt}}}{R^2 \pi}, \tag{3.12}$$

with the scattered Intensity $\mathbf{I}_{\mathrm{scatt}}$, the detector distance D and the radius R. The scattered fraction is calculated along a one-dimensional detector for a silver sphere of radius $R = 30\,\mathrm{nm}$ with a laser wavelength of $\lambda = 13.5\,\mathrm{nm}$ and the corresponding atomic scattering factor $f^0 = 23.00 - 16.52i$ [57]. The corresponding refractive index can be computed via eq. (2.77) and is $n = 0.8896 + 0.0779$, which is utilized for calculation of the Mie solution. The number density can be described with $n_a = \frac{3}{4\pi r_s^3}$ with the Wigner-Seitz radius $r_s = 1.59\,\text{Å}$ for bulk silver, the corresponding particle number for atomic resolution is $N_{\mathrm{at}} = \left(\frac{R}{r_s}\right)^3$. The scattered fraction is computed for different dipole numbers that are arranged in a face-centered-cubic lattice, see fig. 3.2a. The numbers in brackets of the legend are the in-medium wavelength in units of inter atomic distances $\tilde{\lambda} = \lambda/|n|d$ with the dipole-dipole distance d and the refractive index n, which basically is the number of dipoles per wavelength. It can be seen that smaller dipole numbers result into a deviation from the Mie result especially at larger scattering angles. This is because at larger scattering angles the smallest distances contribute most to the scattering signal and these are not resolved sufficiently anymore for the small super-particle numbers. At zero scattering angle, the result is only proportional to the particle number and therefore is equal for all cases. For the investigated case, a resolution of $\tilde{\lambda} = 5.92$ is required to achieve a reasonably high accuracy to describe features at high scattering angles. This is highlighted by the inset of fig. 3.2a. Note, that the number of iterations required to reach convergence is unaffected by the number of particles computed. Actually, the number of iterations only depends on the size parameter kR (wave number times radius) for a certain refractive index. This is illustrated in fig. 3.2b by the number of iterations (convergence reached at $R \leq 10^{-5}$) versus the size parameter for a silver sphere, for the same laser

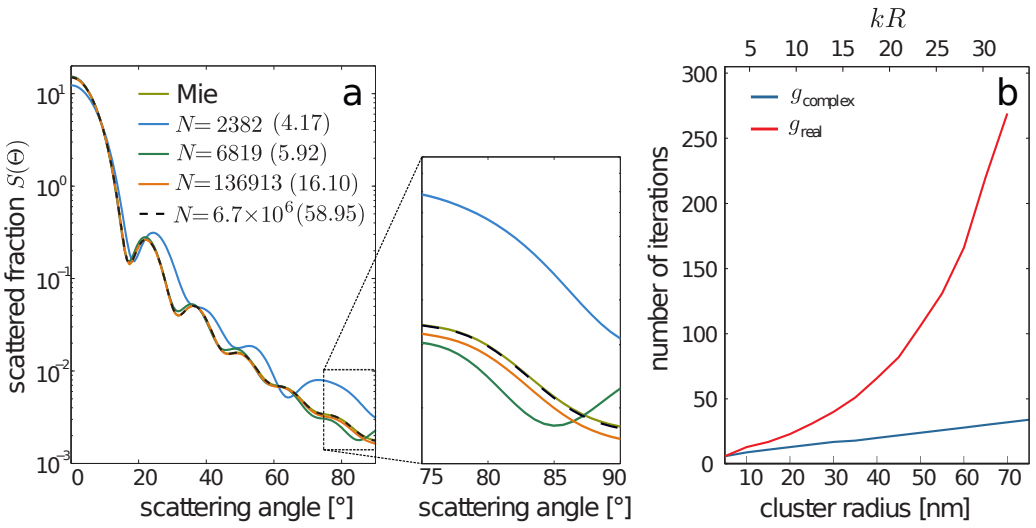

Figure 3.2.: a) Scattered fraction $S(\Theta) = \frac{dN_{\mathrm{scat}}}{N_{\mathrm{inc}} d\Omega}$ of a silver sphere with $R = 30\,\mathrm{nm}$ and $f^0 = 23.00 - 16.52i$ with fcc crystal structure for different particle numbers (see legend) and corresponding Mie solution for the scattering of $\lambda = 13.5\,\mathrm{nm}$ radiation. The scattered fraction indicates the number of photons dN_{scat} scattered into an element of solid angle $d\Omega$ relative to the number of photons impinging on the geometrical cross section of the target N_{inc}. Note that the highest particle number corresponds to atomic resolution. For the CSDDA, a convergence criterion $R < 10^{-5}$ has been used. The numbers in brackets in the legend labels indicate the in-medium wavelength in units of the inter atomic distance $\tilde{\lambda} = \lambda/|n|d$. b) Cluster-size dependent convergence analysis with optimal real and optimal complex (CSDDA) mixing parameter for the same cluster and laser parameters as in a. The chosen particle numbers did not affect the convergence speed. Figure published in [117].

wavelength and atomic scattering factor as before. It can be seen, that the number of iterations increases for larger size parameters, for the CSDDA it ascends moderately, whereas for the real scaling it exponentially increases.

In summary, the DDA with a complex scaling mixing approach represents a simple and intuitive description of the discrete dipole approximation. The method could successfully be benchmarked for a spherical silver target including absorption. In the following section, the CSDDA is utilized to investigate the influence of different wavelength onto the diffraction pattern on the example of a silver icosahedron. The diffraction patterns are further compared to MSFT diffraction patterns to analyze the applicability of different numerical models in different scattering regimes.

3.2. Influence of laser wavelength on diffraction patterns

Depending on the utilized wavelength and the target in single-shot diffractive imaging experiments, absorption can either be negligible or play an important role in the scattering scenario. Further, the wavelength influences the resolvable scattering angle, as has been discussed in chapters 1.2 and 2.2.2. In addition to that, the wavelength impacts the

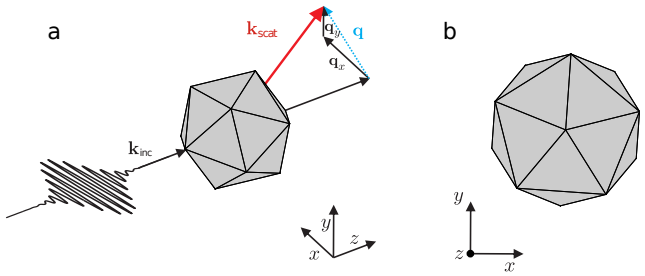

Figure 3.3.: a) Schematic setup of the scattering scenario. An incident plane wave polarized in x propagating in z-direction interacts with an icosahedron. b) depicts the icosahedron as seen by the laser. Parts of the figure published in [117].

wavelength / photon energy	$f1$	$f2$	absorption length l_{abs}
20 nm / 62 eV	8.38	18.16	8.3 nm
13.5 nm / 92 eV	23.00	16.52	13.6 nm
5 nm / 248 eV	14.13	4.69	129.1 nm
1.24 nm / 1 keV	38.9	18.21	134.1 nm
0.5 nm / 2.48 keV	40.54	5.18	1169.0 nm

Table 3.1.: Relevant atomic scattering factors and absorption lengths for silver for different wavelength and photon energies as tabulated from [57].

applicable numerical model for reconstruction of the particle density from the diffraction pattern (cf. chp. 2.2). In what way the wavelength influences the points stated above can be clarified by systematically studying diffraction patterns for different laser wavelengths and numerical models. In this section, this is done exemplarily for a silver icosahedron utilizing CSDDA and MSFT to compute single-shot diffraction images.

The influence of the wavelength on the diffraction pattern is tested for the scenario, depicted in fig. 3.3a, a laser is propagated in z-direction, polarized in x and interacts with a silver icosahedron with outer radius of $R = 120\,\text{nm}$. The 2D detector screen is situated in the far field at $200R$. The particle as seen by the laser is depicted in fig. 3.3b. The diffraction patterns are computed for five different wavelength from $\lambda = 20\,\text{nm}$ to $\lambda = 0.5\,\text{nm}$, listed in tab. 3.1. The diffraction patterns are computed with CSDDA (chp. 3.1) and MSFT (chp. 2.2.2), for both methods with and without absorption. The following simulation parameters are utilized for the CSDDA. For $\lambda = 20\,\text{nm}$ and $\lambda = 13.5\,\text{nm}$, the icosahedra are computed with $N = 1.2 \times 10^6$ super particles, the three shorter wavelengths with $N = 7.8 \times 10^6$ dipoles, the corresponding atomic scattering factors ($f^0 = f_1 - if_2$) can be found in tab. 3.1. There, also the absorption lengths for the multislice Fourier transform method are displayed. The three dimensional particle density for the MSFT calculation is described on $60 \times 60 \times 60$ grid points, the Fourier transforms are computed with a resolution of 1024×1024 grid points.
Figure 3.4a-d show the diffraction patterns computed with CSDDA, fig. 3.4e-h show the MSFT results. The left halves of all diffraction patterns are computed with absorption

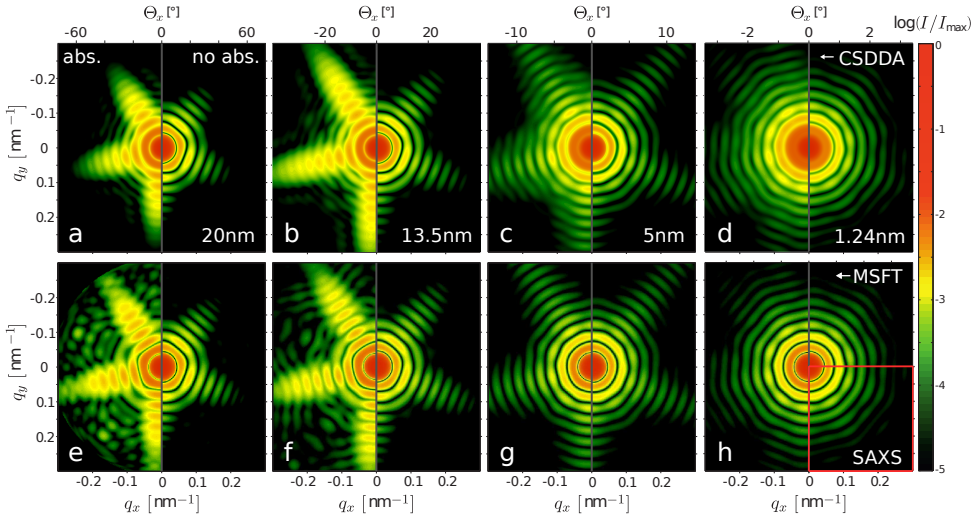

Figure 3.4.: Diffraction patterns for different wavelength as predicted with CSDDA and MSFT. Upper panels are complex scaling discrete dipole approximation (CSDDA, see sec. 3.1) calculations, lower panels multislice Fourier transform (MSFT, see sec. 2.2.2) simulations with and without absorption taken into account. The wavelength are indicated in the lower right corners in the upper panel and also apply to the diffraction patterns below. The diffraction pattern h also contains a small angle x-ray scattering (SAXS, see sec. 2.2.2) diffraction pattern in the lower right quarter of the image, highlighted by a red square. Parts of figure published in [117].

taken into account, the right halves show the respective first Born approximation, hence, no absorption is included. Basically three observations can be made from the diffraction patterns.

(i) Absorption has a large impact on diffraction patterns, especially for the larger wavelength. The effect of absorption onto the diffraction pattern manifests as a blurring of the fringes and a rising of the scattered intensity at larger scattering angles. The influence of absorption decreases for smaller wavelength, the differences between full Born solution and first Born approximation relative to the central region becomes less distinct.

(ii) The simple absorption model in the MSFT calculations delivers different results than the CSDDA patterns. The blurring of fringes due to absorption is larger for the MSFT diffraction patterns of the long wavelengths and smaller for the shorter wavelength compared to the respective CSDDA results. This behavior can be attributed to the lack of backscattering in the MSFT absorption model. For the longest absorption length in fig. 3.4h almost no difference between absorption and no absorption can be observed, whereas in the CSDDA result the fringes are a bit blurred compared to the result without absorption (cf. fig. 3.4d and h).

(iii) For larger wavelength, diffraction patterns are not point symmetric. This is because in

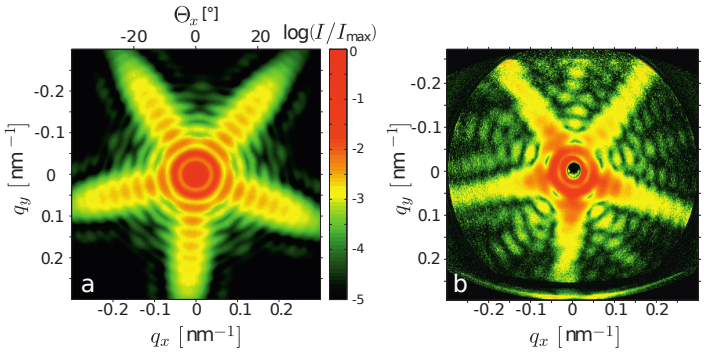

Figure 3.5.: a) CSDDA diffraction pattern of a $R = 120\,\text{nm}$ icosahedron with $N = 1.2 \times 10^6$, $\lambda = 13.5\,\text{nm}$ and the corresponding atomic scattering factor $f^0 = 23.00 - i16.52$ for silver. b) Experimental diffraction pattern from a $R \approx 120\,\text{nm}$ silver icosahedron obtained at FLASH with $\lambda = 13.5\,\text{nm}$ and a pulse duration of $\tau \approx 100\,\text{fs}$ by Barke *et al.* [10]. Figure published in [117].

this regime, larger scattering angles can be resolved (cf. sec. 2.2.2), in which the scattering image contains information about the 3D orientation of the particle. In the region of small wavelength, i. e. small scattering angles, the diffraction pattern only is dependent on the projected density of the target. This becomes evident for fig. 3.4h ($\lambda = 1.24\,\text{nm}$), where the MSFT result matches the Fourier transform of the projected density, shown in the lower right quarter of the figure (small angle x-ray scattering - SAXS).

From the observations, two different scattering regimes can be identified. The small angle scattering regime that can be accessed by short wavelength radiation with photon energies of keVs. In this regime, diffraction patterns are only dependent on the projected target density. Due to the small effect of absorption on those scattering images, phase retrieval algorithms can be applied to retrieve information about the target from the diffraction patterns. In the wide angle scattering regime with rather long wavelength with photon energies of tens to hundreds of eV, 3D information about the target can be inferred from the diffraction pattern, however, the interpretation gets complicated due to the large impact that absorption has on the diffraction patterns.

Figure 3.5a shows the complete CSDDA diffraction pattern of the silver icosahedron of fig. 3.4b with absorption for $\lambda = 13.5\,\text{nm}$. This pattern can be compared to a scattering image for a single-shot diffraction experiment performed at the free electron laser FLASH for the same laser wavelength for a pulse duration of $\tau \approx 100\,\text{fs}$ for silver nanotargets in free flight. The experimental image shows the same blurring of the fringes as the simulation. Hence, the blurring of the fringes in the experiment also can be explained with the effects of absorption and does not occur from a deformation of the target due to the interaction with the laser pulse. However, the CSDDA result has been computed with only a single frequency. Experimentally, the creation of a monochromatic laser pulse with finite pulse durations is impossible. Therefore, in the following, the effect of a finite pulse duration onto scattering images is investigated.

3.3. Influence of pulse duration on diffraction patterns

For ultrafast imaging of e. g. transient plasma dynamics on the attosecond time scale, pulse durations on the same order are required. Attosecond imaging might become feasible in the future when utilizing high harmonic generation sources (cf. chapter 5.1). So far, the assumption has been made that the laser beam from a high intensity x-ray source is monochromatic, this is only correct in the continuous wave limit. Finite pulse durations only can be achieved utilizing light with a certain bandwidth. For a Fourier limited pulse, the pulse duration τ and bandwidth $\Delta\omega$ are connected via

$$\frac{\Delta\omega}{2\pi}\tau = \mathrm{TBP}, \tag{3.13}$$

with the time-bandwidth-product TBP, which is linked to the pulse shape. Hence, short pulses can only be achieved with large bandwidths resulting into the laser spectrum consisting of multiple frequencies. Therefore, in this section, the influence of a large bandwidth onto the diffraction pattern is investigated. First, the evolution of a diffraction pattern from an icosahedron is analyzed for decreasing pulse durations, i. e. increasing bandwidth. Second, the decreasing fringe contrast induced by decreasing pulse durations is determined by introducing a simple measure to estimate the pulse duration where the fringe contrast is lost.

3.3.1. Diffraction patterns for different pulse durations

The discrete dipole approximation does not include time, it is a static method where only a single frequency can be considered. To describe the interaction of a nanotarget with a laser beam with a finite pulse duration, the corresponding bandwidth (cf. eq. (3.13)) can be spectrally decomposed. In linear response, the scattered intensities from each spectral component can be computed independently and can be added up weighted according to the pulse shape to obtain the total scattered intensity. In this analysis, a Gaussian pulse shape is implemented. Therefore, the amplitudes $\tilde{\mathbf{E}}$ of the spectral components are chosen corresponding to a Gaussian pulse via

$$\tilde{\mathbf{E}} = \tilde{\mathbf{E}}_\mathrm{c} e^{\left(\frac{-\tau(\omega-\omega_\mathrm{c})}{2}\right)^2}, \tag{3.14}$$

with the center frequency ω_c, the center field amplitude $\tilde{\mathbf{E}}_\mathrm{c}$ and the pulse duration τ. The influence of the pulse duration is tested for the same scattering scenario as in the previous section (cf. fig. 3.3a) for a slightly smaller icosahedron with $R = 64.5\,\mathrm{nm}$. The central laser wavelength is set to $\lambda = 13.5\,\mathrm{nm}$ and CSDDA diffraction patterns are computed for three different pulse durations and the cw (continuous wave) solution. The corresponding atomic scattering factor can be found in tab. 3.1. The diffraction patterns are depicted in fig. 3.6. It can be seen that for decreasing pulse duration (which corresponds to an increasing bandwidth), the fringe contrast decreases. At $\tau = 1\,\mathrm{fs}$, which is a much smaller

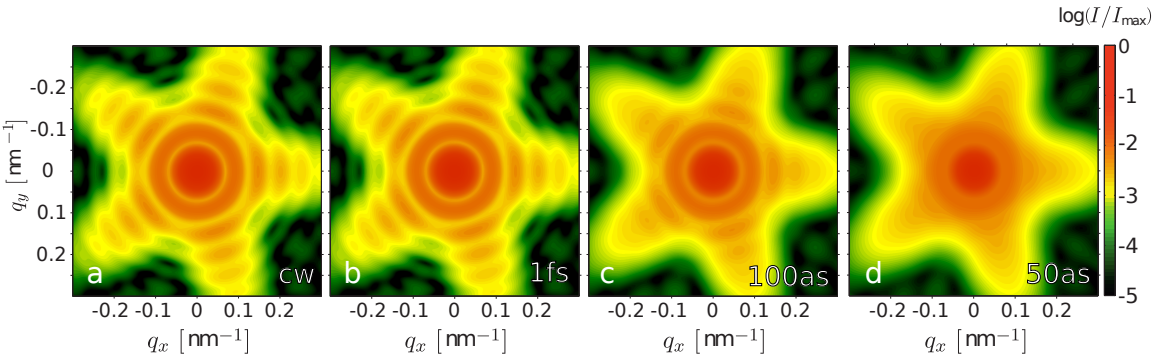

Figure 3.6.: CSDDA diffraction patterns for a silver icosahedron with $R = 64.5\,\text{nm}$ and a central laser wavelength $\lambda = 13.5\,\text{nm}$ for different pulse durations indicated in the lower right corner of each pattern. Figure modified from [117].

pulse duration than typically achieved in FEL experiments, the diffraction pattern does not differ from the cw solution. Only for very short pulses from 100 as the diffraction pattern starts to alter, visible as blurring of the fringes. The overall shape of the diffraction pattern persists such that the information about the target orientation remains accessible. At $\tau = 50\,\text{as}$, the fringes are no longer visible so the size information about the target is lost. This means that the future prospect of attosecond imaging is feasible.

In the following section, the blurring of the fringes is investigated more systematically. To this end, the fringe contrast which represents a simple measure of the blurring effect is introduced. Further, a simple estimate for the critical pulse duration, where the fringe contrast and therefore the size information is lost, is derived as function of wavelength and scattering order.

3.3.2. Fringe contrast in dependence on wavelength

As the starting point, a contrast parameter is introduced to quantify the loss of information on the size. In the following, the procedure underlying the definition of the contrast measure is motivated based on sample results. Figure 3.7a shows slices through the diffraction pattern obtained for a icosahedron with $kR = 20$ and $\lambda = 5\,\text{nm}$ with a pulse duration of $\tau = 100\,\text{as}$ (dark red line) and the cw-solution (orange line). The fringes cannot be separated anymore, when the ratio between maxima and preceding minima is equal or larger than one. The ratio is called γ parameter in the following and is depicted here for the fourth scattering order. This γ parameter is computed for different wavelength and different scattering orders in dependence on the pulse duration, displayed in fig. 3.7b. Three conclusions can be drawn from the plot. First, the γ parameter is larger for all scattering orders for the shorter wavelength. The reason is that the smaller influence of absorption on the diffraction pattern results into sharper maxima compared to the larger wavelength already for the cw-solution. Second, the fringe contrast gets lost at longer

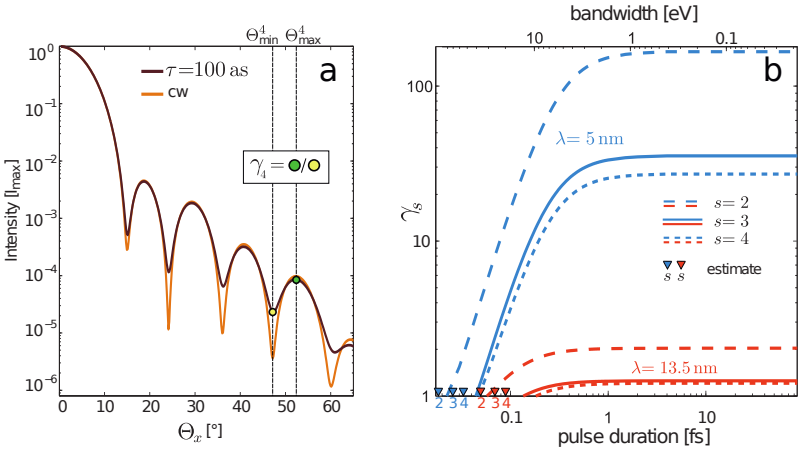

Figure 3.7.: a) Scattered intensity in dependence on scattering angle along x for the scattering by a silver icosahedron with $kR = 20$ and the central wavelength $\lambda = 5\,\mathrm{nm}$ for the cw solution (orange) and $\tau = 100\,\mathrm{as}$ (dark red) The definition of the γ parameter for the fourth maximum is indicated as the ratio of the maximum and preceding minimum by the circles. b) γ parameter for different central laser wavelength and scattering orders in dependence on the pulse duration. Figure published in [117].

pulse durations for higher scattering orders, i. e. at larger scattering angles. Third, the fringe contrast starts to decrease for both wavelength only at pulse durations of about 1 fs. Therefore, single-shot diffraction experiments at free electron lasers with typical pulse durations of $\tau \approx 100\,\mathrm{fs}$ are not influenced by the finite bandwidth (cf. fig. 3.5). However, for future attosecond imaging experiments, it is necessary to find a trade-off between utilized wavelength (which influences the resolvable angular range) and pulse duration to achieve the highest possible information content in the diffraction patterns.

An analytical estimate for this trade-off can be derived by assuming that the fringe contrast disappears when the position of the maximum of the highest frequency of the laser pulse and the preceding maximum of the lowest frequency overlap. Assuming a spherical non-absorbing target, the position of the sth maximum is approximately (cf. sec. 2.2.2)

$$qR = \pi(s+1) \tag{3.15}$$

with the radius R, the transfer momentum $q = 2k\sin(\Theta/2)$, the scattering angle Θ and the wave number k for the central frequency of the pulse. For small scattering angles the transfer momentum can be written as $q = k\Theta$. Inserting this relation into eq. (3.15) gives the scattering angle for a certain maximum s via

$$\Theta^s = \frac{\pi(s+1)}{kR}. \tag{3.16}$$

The fringe contrast at a certain maximum is vanishing when the maximum s of the highest frequency component of the spectrum $k + \Delta k/2$ and the maximum $s-1$ of the lowest

frequency component $k - \Delta k/2$ overlap. This is the case, if

$$\Theta^s(k + \Delta k/2) = \Theta^{s-1}(k - \Delta k/2) \tag{3.17}$$

which then gives

$$\frac{\pi(s+1)}{R(k + \Delta k/2)} = \frac{\pi s}{R(k - \Delta k/2)} \tag{3.18}$$

$$(s+1)(k - \Delta k/2) = s(k + \Delta k/2) \tag{3.19}$$

$$\frac{k}{\Delta k} = s + \frac{1}{2}. \tag{3.20}$$

This relation can be connected to the critical pulse duration where the fringe contrast vanishes via eq. (3.13), which yields (with $\Delta\omega = \Delta k/c$, the speed of light c and $k = 2\pi/\lambda$)

$$\tau_{\text{crit}} = \frac{\lambda \text{TBP}(s + \frac{1}{2})}{c}. \tag{3.21}$$

This critical pulse durations for the corresponding cases with TPB = 0.44 for a Gaussian pulse shape are indicated in fig. 3.7 by triangles. Although the critical pulse durations from the simple estimate are a bit shorter than the critical pulse durations computed from the CSDDA results, the overall behavior is equivalent: for smaller wavelength and larger scattering orders the critical pulse durations are shorter. Therefore, the analytical estimate gives a simple relation for finding the trade-off between wavelength and pulse duration to estimate the achievable information content in an attosecond single-shot diffraction experiment.

4. Characterization of hydrogen jets by single-shot x-ray diffractive imaging

The characterization of hydrogen from the strongly coupled state to a high energy density (HED) plasma state is crucial for the understanding of astrophysical objects such as giant planets [52] and for achieving laser driven fusion [74]. The reason is that hydrogen at high pressures is a major component of planets interiors and a key ingredient for inertial confinement fusion. For understanding these systems measurements have to be taken at similar or the same conditions. Spectrally resolved x-ray Thomson scattering (XRTS) is a well-established diagnostic tool for warm dense matter and can be utilized for characterizing basic plasma properties such as temperature, density and ionization state [104, 51, 102, 47]. The plasma properties are accessed by measuring the inner structure of the target via the static and dynamic structure factor. XRTS is usually performed utilizing lab-based laser systems, but also can be performed at free electron lasers [46]. The experiments are highly repetitive and typical targets are foils, where the target can be assumed to be seen as infinite by the laser. However, there are other available targets such as droplets or jets. Hydrogen jets for example are a suitable target to investigate the plasma properties of hydrogen in a infrared (IR) pump - x-ray probe setup, where the plasma state is created by interaction with an IR laser and probed with an x-ray beam. These jets are created by injecting liquid H_2 from a cryostat (cooled with helium) into a vacuum chamber. The evaporative cooling results into a liquid or solid cylindrical jet of pure hydrogen [69]. At a certain point the jet experiences a breakup and scatters into nanodroplets due to the Rayleigh instability [95].

In this chapter, the influence of a jet target is investigated and how its finite shape effects the actual goal of achieving information about the inner structure of the target. To this end, first, characteristic properties of diffraction patterns obtained by jet scattering are analyzed. Therefore, typical diffraction patterns of cylindrical jet targets are investigated utilizing different numerical methods. Further, the influence of the shape and density distribution and the structural disorder on the diffraction pattern is examined. In the second part, different structural jet properties and how they effect the corresponding diffraction patterns are analyzed. Different effects of jet shape variation are connected to experimental diffraction patterns from a FLASH experiment conducted on a hydrogen jet target.

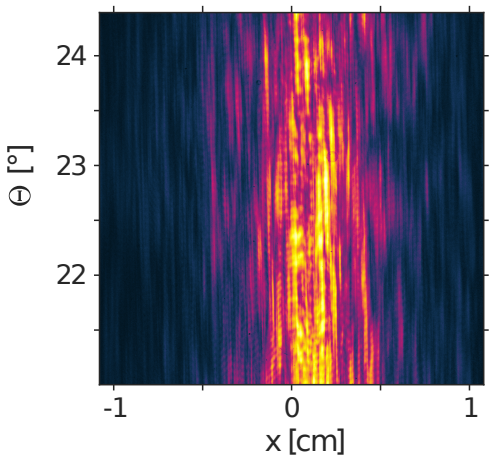

Figure 4.1.: Diffraction pattern of a 10 μm hydrogen jet obtained at FLASH (by Ulf Zastrau *et al.*) with a laser wavelength of $\lambda = 13.5\,\text{nm}$.

4.1. Single-shot x-ray diffractive imaging as diagnostic tool

In single-shot diffractive imaging experiments, structure, shape and size of finite nanotargets can be resolved. In the following, the possibility to also extract plasma properties from diffraction patterns is analyzed. To this end, it is important to understand what contributes to the scattering signal. The scattering signal is a sum of the scattering by the shape of the target and its inner structural disorder, in the following denoted by coherent and incoherent scattering. From the coherent signal from forward scattering the static structure factor can be directly measured [44], i. e. from the elastically scattered intensity from tightly-bound electrons the spatial structure of the target can be accessed. The incoherent signal emerging from weakly bound quasi-free electrons encodes the dynamical structure factor, i. e. excitations to the system. In typical diffractive imaging experiments on finite nanotargets, the coherent signal is orders of magnitude larger than the incoherent scattering. However, as mentioned above for deducing information about excitations to the system, incoherent scattering has to be evaluated.

In this chapter, it is investigated whether a jet is a suitable target to resolve coherent and incoherent scattering on the same detector. A typical experimental diffraction pattern of a hydrogen jet obtained at FLASH by Ulf Zastrau *et al.* with a laser wavelength of $\lambda = 13.5\,\text{nm}$ is displayed in fig. 4.2a. The diffraction pattern shows distinct features. Multiple straight streaks with high-frequency fringes along the Θ-axis can be observed that decrease in intensity the further away from the center. The following analysis aims to understand which characteristic features of the diffraction pattern emerge from coherent scattering, which from diffuse scattering and which from possible jet breakups. In this section, therefore first, the basic scattering scenario on a hydrogen jet target is presented shortly. Second, the coherent signal that depends on the spatial structure of the jet is computed

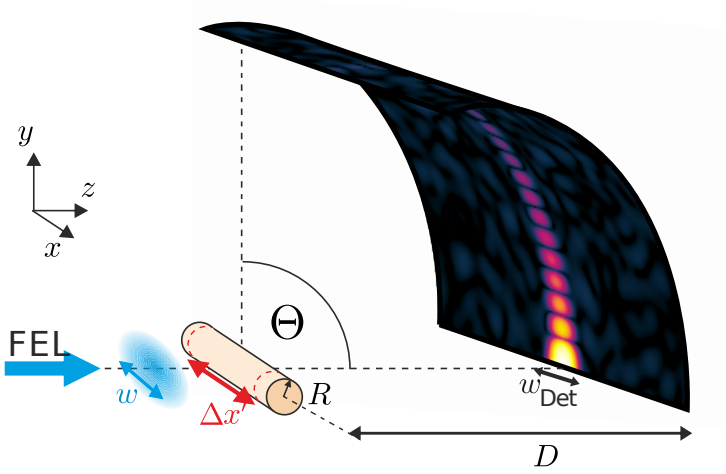

Figure 4.2.: Schematic setup for a jet scattering experiment. The incident Gaussian laser pulse with spot size w hits a cylindrical jet with radius R. The diffraction pattern is obtained on a detector in distance D. The scattering angle is denoted by Θ.

and analyzed utilizing the discrete dipole approximation with a cylindrical jet target with a regular grid, i. e. without structural disorder. Third, the same target is investigated with an inner structural disorder by introducing a random particle distribution. Averaging diffraction patterns from multiple random particle distributions then includes coherent and incoherent signal.

4.1.1. Jet scattering scenario

A single-shot diffractive imaging experiment on a solid or liquid jet can be performed as follows: a high intensity short laser pulse, e. g. from a free electron laser (FEL) hits the jet and the scattered intensity is recorded on a far-field detector. The field amplitude of the laser pulse can be described as a Gaussian pulse via

$$\hat{\mathbf{E}}_0 = \hat{\mathbf{E}}_{\max} e^{-\frac{x^2+y^2}{w^2}}, \tag{4.1}$$

with the maximal field amplitude $\hat{\mathbf{E}}_{\max}$ and the positions x and y. The spot size is denoted by w. In the following, the discrete dipole approximation is utilized to describe such a scattering experiment. The laser wavelength is set to $\lambda = 13.5\,\mathrm{nm}$ throughout the chapter. In this wavelength regime, the refractive index of hydrogen is basically unity [57] and therefore absorption can be neglected. Thus, the scattered electric fields can be computed in first Born approximation (see chp. 2.2.3). The hydrogen jet, is implemented as a cylinder aligned along the x-axis with radius R and length $\Delta x'$, as depicted in fig. 4.2. The detector is placed in the far-field with a distance to the jet center $D = 200R$. The particle density for hydrogen at solid state is $\rho = 0.8988 \times 10^{-4}\,\mathrm{g/cm^3}$, which results into a Wigner-Seitz radius of $r_s = 1.8\,\text{Å}$. In the following subsection the coherent scattering

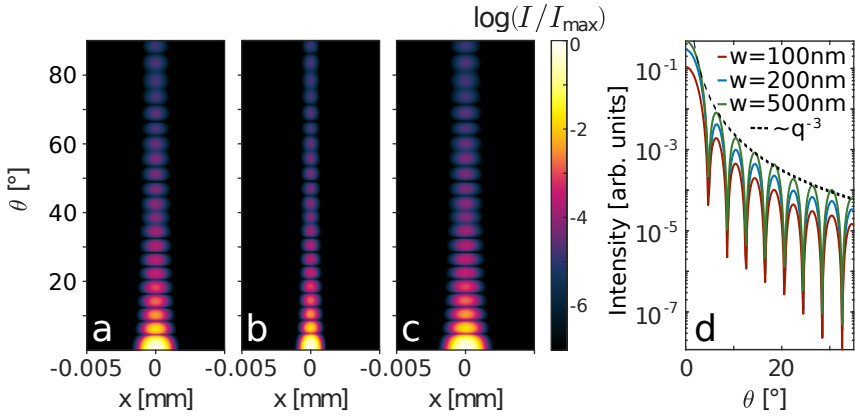

Figure 4.3.: a)-c) Diffraction patterns for different Gaussian spot sizes of a cylindrical jet computed with DDA in first Born approximation. The laser wavelength is set to 13.5 nm, the jet radius to $R = 100\,\text{nm}$. a) $w = 100\,\text{nm}$, b) $w = 200\,\text{nm}$ and c) $w = 500\,\text{nm}$. d) Scattered intensities for $x = 0$ corresponding to a-c.

signal from a hydrogen jet is investigated.

4.1.2. Coherent scattering: basic structure and influence of finite focus size

The coherent signal emerges from elastically scattered photons and can be reproduced by a regular dipole distribution. Therefore, the dipoles are distributed on an equidistant grid with sub-wavelength distance $\lambda/3$, which reflects the continuum case. The cylinder radius is set to $R = 100\,\text{nm}$ and the height to $\Delta x' = 10w$. To not only examine the basic structure of a diffraction pattern from a cylindric target, but also the influence of the finite laser focus size, the scattering scenario is characterized for three different focus sizes of the incident Gaussian pulse, $w_1 = 100\,\text{nm}$, $w_2 = 200\,\text{nm}$ and $w_3 = 500\,\text{nm}$. The resulting diffraction patterns are depicted in fig. 4.3a, b and c respectively. All three diffraction patterns show the same basic structure; a streak with interference fringes perpendicular to the jet resulting from Mie scattering. The fringe distance is dependent on the jet radius and is equivalent for all three diffraction patterns, as can be seen in fig. 4.3d showing the intensity traces along $x = 0$. The maximal signal scales with the number of irradiated particles squared n^2. It is larger for larger w, since the larger the spot size the more particles are irradiated. The streak signal decreases with larger scattering angle with q^{-3}, as indicated by the dashed line. For a spherical target the scattering signal decreases with q^{-4}, hence, the signal from jets is visible up to larger scattering angles (cf. chp. 2.2.2). These results show that from coherent scattering the size and density of the jet can be deduced. The difference between the three diffraction patterns in figs. 4.3a-c displays in the width of the streak. For $w_1 = 100\,\text{nm}$ it is larger than for $w_2 = 200\,\text{nm}$, but smaller than for $w_3 = 500\,\text{nm}$. The exact values of the widths of the streaks can easily be accessed from the diffraction patterns at $\Theta = 0\,^\circ$ by extracting the full width at half maximum

(FWHM). The streak widths then can be computed via $w_{\mathrm{det}} = \mathrm{FWHM}/\sqrt{4\ln 2}$ and are $w_{\mathrm{det},1} = 441\,\mathrm{nm}$, $w_{\mathrm{det},2} = 294\,\mathrm{nm}$, and $w_{\mathrm{det},3} = 507\,\mathrm{nm}$, respectively. This clarifies the observation that the line focus on the detector does not change linearly with the incident laser spot size. To understand this behavior, in the following an analytical expression for the line focus on the detector is derived.

Analytical expression for line focus width on the detector

To derive the width of the line focus on the detector, a jet with radius R aligned along the x-axis is considered. The detector is placed in z-direction and its distance D is assumed to be much larger than R. In this case, the scattered electric field only depends on the particle density projected onto the x-y-plane, as has been shown in chp. 2.2.2. The scattered electric field for the introduced scenario reads (cf. eq. (2.56))

$$\mathbf{E}(x,y) = \int 2n_a c_0 \frac{\hat{\mathbf{E}}_0 e^{ikr}}{4\pi r}\sqrt{R^2 - y'^2}e^{-iq_y y'}dy'dx', \tag{4.2}$$

with the number density n_a and $c_0 = \alpha(\omega)\omega^2\mu_0$, where α is the frequency ω dependent polarizability and μ_0 the permeability of free space. The distance between jet and detector is denoted by r. Note that D is the smallest distance between detector and jet, and r is the distance between any point of the jet and any point on the detector. To derive the width of the line focus it is sufficient to only consider a single detector trace along x with $y = 0$. In this case, $q_y = 0$ and eq. (4.2) becomes

$$\mathbf{E}(x) = \int 2n_a c_0 \frac{\hat{\mathbf{E}}_0 e^{ikr}}{4\pi r}\sqrt{R^2 - y'^2}dy'dx', \tag{4.3}$$

Inserting the expression for the Gaussian field amplitude eq. (4.1) into eq. (4.3) yields

$$\mathbf{E}(x) = n_a c_0 \hat{\mathbf{E}}_{\max} \int \frac{e^{ikr}}{2\pi r} e^{-\frac{x'^2+y'^2}{w^2}}\sqrt{R^2 - y'^2}dy'dx', \tag{4.4}$$

Performing the integration of y' gives

$$c_1 = \int_{-R}^{R}\sqrt{R^2 - y'^2}e^{-\frac{y'^2}{2w^2}}dy' = \frac{1}{2}\pi R^2 e^{-\frac{R^2}{4w^2}}\left(I_0\left(\frac{R^2}{4w^2}\right) + I_1\left(\frac{R^2}{4w^2}\right)\right), \tag{4.5}$$

with $I_n(z)$ denoting the modified Bessel function of first kind. The integrand is just a factor and is denoted by c_1 in the following. For small Gaussian spot sizes much smaller than the detector dimensions $w \ll x$ only parts of the jet with $x' \ll x$ will contribute to the scattering signal and the distance between jet and detector can be assumed to be constant $r = D$. However, for larger w, this relation does not hold anymore. Thus, for the general case r is expressed via $r(x') = \sqrt{D^2 + (x - x')^2}$. Inserting this into eq. (4.4)

gives

$$\mathbf{E}(x) = n_a c_0 c_1 \hat{\mathbf{E}}_{\max} \int\int \frac{e^{ik\sqrt{D^2+(x-x')^2}}}{2\pi\sqrt{D^2-(x-x')^2}} e^{-\frac{x'^2}{w^2}} dx', \tag{4.6}$$

The term $\sqrt{D^2+(x-x')^2} = D\sqrt{1+(x-x')^2/D^2}$ can be replaced by its Taylor expansion around $(x-x')^2/D^2$, i. e. by $D+(x-x')^2/2D$, since $x, x' < D$. Further, the following relation holds $1/\sqrt{D^2+(x-x')^2} \approx 1/D$. Inserting both expressions into eq. (4.6) yields

$$\mathbf{E}(x) = n_a c_0 c_1 \frac{\hat{\mathbf{E}}_{\max} e^{ikD}}{2\pi D} \int \exp\left(ik\frac{(x-x')^2}{2D}\right) \exp\left(-\frac{x'^2}{w^2}\right) dx', \tag{4.7}$$

Further, the remaining prefactors are condensed into $c_2 = 2n_a c_0 c_1 \frac{\hat{\mathbf{E}}_{\max}}{2\pi D}$, which then simplifies eq. (4.7) to

$$\mathbf{E}(x) = c_2 e^{ikD} \int \exp\left(ik\frac{(x-x')^2}{2D}\right) \exp\left(-\frac{x'^2}{2w^2}\right) dx'. \tag{4.8}$$

Expanding $(x-x')^2$ and rearranging gives

$$\mathbf{E}(x) = c_2 e^{ikD} \int \exp\left(-\left[\frac{1}{2w^2} - \frac{ik}{2D}\right] x'^2 - \left[\frac{ikx}{D}\right] x'\right) dx'. \tag{4.9}$$

The integral over x' can easily be performed by considering the relation

$$\int \exp(-(ax^2+bx))dx = \sqrt{\frac{\pi}{a}} \exp\left(\frac{b^2}{4a}\right). \tag{4.10}$$

In this case, $a = \frac{1}{2w^2} - \frac{ik}{2D}$ and $b = \frac{ikx}{D}$, and the electric field with $c_3 = \sqrt{\frac{\pi}{a}}$ becomes

$$\begin{aligned}
\mathbf{E}(x) &= c_2 c_3 e^{i(kD+x^2/2D)} \exp\left(\frac{-k^2x^2}{4D^2}\frac{2w^2D}{D-ikw^2}\right) \\
\mathbf{E}(x) &= c_2 c_3 e^{i(kD+x^2/2D)} \exp\left(\frac{-k^2x^2w^2D}{2D^2}\frac{D+ikw^2}{D^2+k^2w^4}\right) \\
\mathbf{E}(x) &= c_2 c_3 e^{i(kD+x^2/2D)} \exp\left(\frac{-2k^2w^2x^2}{2D^2+2k^2w^4} - i\frac{k^3w^4x^2}{2D(D^2+k^2w^4)}\right)
\end{aligned} \tag{4.11}$$

The scattered intensity is proportional to the squared scattered electric field amplitude $I \propto |\mathbf{E}|^2$ and thus yields

$$I \propto \exp\left(-\frac{k^2w^2x^2}{D^2+k^2w^4}\right) = \exp\left(-\frac{x^2}{w_{\text{det}}^2}\right) \tag{4.12}$$

Comparing the left and right hand side of the equation yields the line focus on the detector

$$w_{\mathrm{det}} = \sqrt{\frac{D^2}{k^2 w^2} + w^2}. \tag{4.13}$$

There are two limits for the line focus of the scattered intensity; (i) for the spot size of the Gaussian beam going towards zero and (ii) going towards infinity

$$\lim_{w\to 0} w_{\mathrm{det}} = \frac{D}{kw}, \tag{4.14}$$

$$\lim_{w\to \infty} w_{\mathrm{det}} = w. \tag{4.15}$$

The relation is depicted in fig. 4.4 in dependence of the laser spot size for constant detector distance $D = 20000\,\mathrm{nm}$ and $\lambda = 13.5\,\mathrm{nm}$. The Gaussian spot size is varied from $w = 30\,\mathrm{nm}$ to $w = 500\,\mathrm{nm}$ to cover both limits. Further, the line focus on the detector can be computed numerically via the DDA and MSFT method (cf. chps. 2.2.3 and 2.2.2). Therefore, the scattering from a cylindrical jet with $R = 100\,\mathrm{nm}$ interacting with a Gaussian pulse with different spot sizes w is calculated. The length of the cylinder is set to $\Delta x' = 10w$. The DDA result is again computed in first Born approximation, and the super particles are distributed on an equidistant grid with sub-wavelength distance $\lambda/3$. The density resolution of the jet for the MSFT method is set to 300×300 and the Fourier transform resolution to 1024×1024. From the diffraction patterns, the line focus can be extracted via $w_{\mathrm{det}} = \mathrm{FWHM}/\sqrt{4\ln 2}$. The resulting line foci are depicted as filled circles in fig. 4.4, the MSFT as dark gray and the DDA as light gray. It becomes evident that the MSFT result reproduces the analytical solution only in the limit of $w \to 0$. The reason is that MSFT only includes far-field components of the scattered electric field. MSFT therefore only is applicable for small spot sizes, where the detector dimensions are much larger than the spot size of the incident beam. This regime is diffraction dominated. The DDA method reproduces the full analytical model since near- and far-field components are included in the computation of the scattered electric field. It therefore can be utilized for any detector dimension. For a typical jet scattering experiment with an incident beam with wavelength of $\lambda = 13.5\,\mathrm{nm}$, a spot size of $w = 20\,\mu\mathrm{m}$ and a detector distance of $\approx 1\,\mathrm{m}$, the resulting width of the line focus on the detector is only $110\,\mu\mathrm{m}$.

4.1.3. Incoherent scattering: Scattering from structural disorder

In the previous subsection, the numerical diffraction patterns were computed with an equidistant grid representing the continuum limit of scattering and ignoring the local structure. To also reproduce the local structure with structural disorder the $N = 10^6$ super-particles are randomly distributed inside the jet and compared to the homogeneous particle distribution. The scattered electric field is computed by DDA, with the same simulation parameters as in the previous section for a spot size of $w = 100\,\mathrm{nm}$. The re-

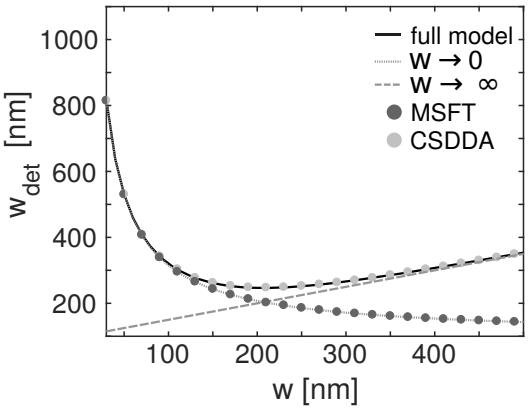

Figure 4.4.: Width of line focus on detector for a jet with $R = 100\,\text{nm}$ for different spot sizes of incident Gaussian laser pulse. The numerical solutions are denoted by the circles, black for MSFT and gray for DDA. Details on the simulation parameters can be found in the text. The analytical solutions are indicated by the solid lines, black for the full model (eq. (4.13)), gray for the limit of $w \to 0$ and the gray dotted line shows the line focus for $w \to \infty$.

sulting diffraction patterns are depicted in fig. 4.5a and b, schematic particle distributions are depicted above each plot.
The diffraction pattern of the randomized particle distribution shows the same features as the pattern from the regular distribution, i. e. a pronounced streak with fringes. However, an additional feature can be observed. Beside the streak a speckle signal from the structural disorder is visible. Averaging the scattering signal over 100 diffraction patterns with different random particle distributions, depicted in fig. 4.5c, gives the contribution from incoherent scattering, i. e. inelastic scattering. It can be seen that the incoherent signal is independent on the scattering angle. The sum of the intensity along the scattering angle shown in the plot above clarifies that the incoherent signal decreases the further away from the streak. At scattering angles of about 60 ° the diffuse signal and the signal from the shape of the jet are on the same order, hence, they can be resolved on the same detector in an experiment.

The analysis shows that single-shot diffractive imaging on jet targets opens the possibility to resolve the scattering from elastic and inelastic scattering on the same detector. In a pump-probe scenario the evolution of signal strength of incoherent signal compared to coherent signal could be utilized to measure e. g. the plasma temperature. The coherent signal can be analyzed for changes in the jet shape and size. The latter possibility is further analyzed in the following section, where variations in jet shape on the diffraction pattern is discussed and compared to experimental results.

4.2. Effects of jet shape onto diffraction patterns

The key motivation for the analysis of this section is a FEL single-shot imaging experiment performed by Ulf Zastrau *et al.* at the free electron laser FLASH in Hamburg. The

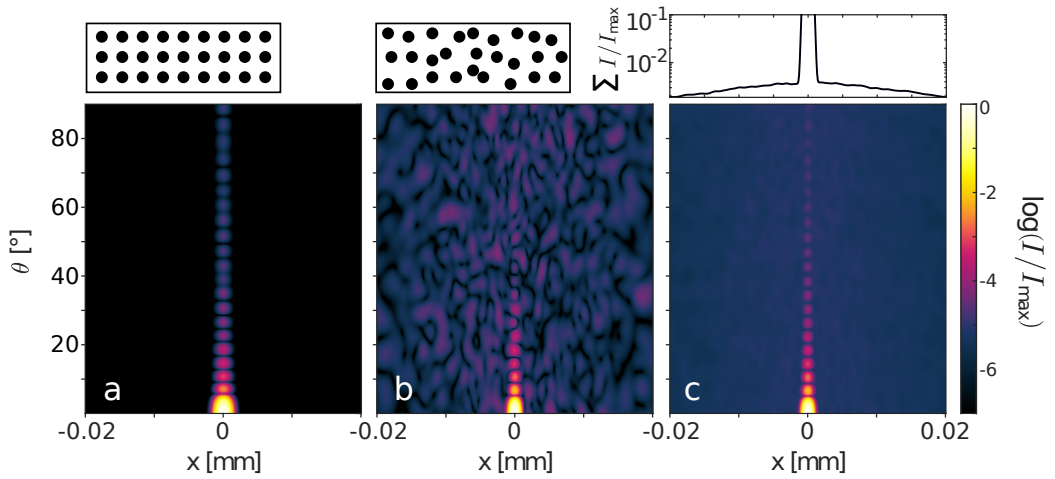

Figure 4.5.: Diffraction patterns of a cylindrical hydrogen jet with $R = 100\,\text{nm}$ and a laser wavelength of 13.5 nm computed with DDA in first Born approximation. a) shows the diffraction pattern the dipoles arranged on a primary cubic regular grid (illustrated in the plot above a). b) shows the diffraction pattern with a randomized distribution of dipoles (illustrated in the plot above b). c) shows the average of 100 diffraction patterns with random distributions. The plot above c shows the sum along the scattering angle, which shows that the incoherent scattering signal decays the further away from the streak.

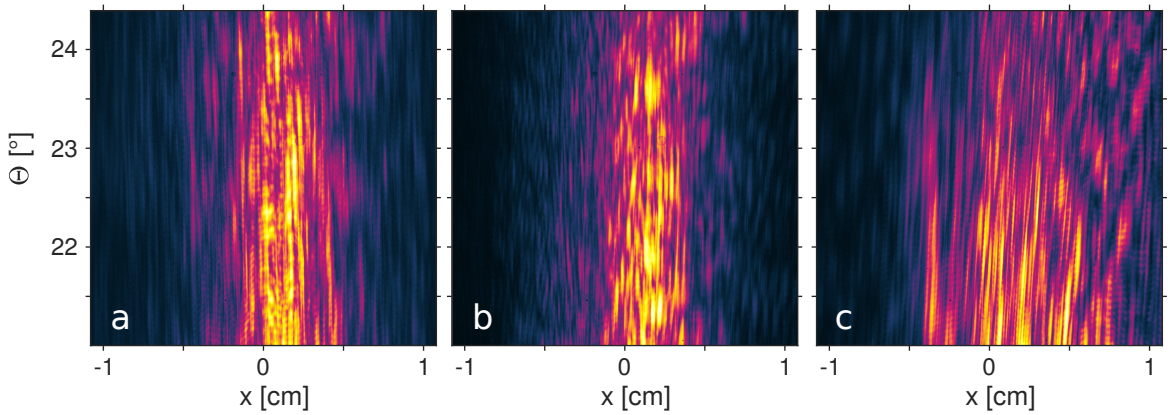

Figure 4.6.: Three example experimental single-shot diffraction patterns from FLASH (by Ulf Zastrau *et al.*) obtained with a laser wavelength of $\lambda = 13.5\,\text{nm}$ and a $10\,\mu\text{m}$ hydrogen jet.

experiment has been conducted on a 10 μm cryogenic hydrogen jet with a laser wavelength of $\lambda = 13.5$ nm. The detector was situated around scattering angle $\Theta = 21\,^\circ$ with an area of 25.4 mm $\times$ 25.4 mm (1881 $\times$ 1882 pixels) and a detector distance of $\approx$ 280 mm). The expected width of the Mie streaks on the detector is $w_{\mathrm{det}} = 36\,\mu$m (or a full width at half maximum of FWHM = 120 μm), which corresponds to 3 pixels (or 9 pixels) of the detector. Three example diffraction patterns from the experiment are depicted in fig. 4.6a-c. Basically four observations can be made.

(i) Fringes from the Mie scattering with a high frequency can be observed along the Θ-axis.

(ii) The streaks are straight for all diffraction patterns and for fig. 4.6a and c they are tilted around the laser propagation direction.

(iii) Some streaks are tilted in other directions than others in the same diffraction pattern. This can be observed in fig. 4.6b.

(iv) Beside bright streaks there are less bright streaks observable on both sides next to it.

Due to the generation process of the FLASH beam in a self-amplified spontaneous emission (SASE) process, the beam profile can have spikes, since it basically results from an amplification of noise [86, 35]. Smooth pulse shapes can be obtained in seeded FELs. The multiple Mie streaks on the detector could therefore emerge from the noisy FEL spectrum. Another possibility for the features in the diffraction patterns can be variations in the jet shape. Therefore, in the following, different jet shape variations are investigated and connected to features in the experimental diffraction patterns. However, first, the Mie fringes can be utilized to retrieve information about the size of the jet by a simple Fourier transform. Afterwards, the effect of the jet shape is analyzed, by investigating the effect of a rotation of the jet, the effect of a breakup of the jet due to a possible Rayleigh instability and last, due to a modulation of the jet surface.

4.2.1. Jet size

First, the jet radius can be identified by taking the Fourier transform of the experimental diffraction patterns. The Fourier transform is performed for ten experimental scattering images including the ones shown in fig. 4.6. The resulting average of the ten Fourier transforms is depicted in fig. 4.7, which reveals a peak at the jet diameter 12.5 μm which is similar to the expected 10 μm.

The shape of the jet and its orientation with respect to the propagation direction of the laser can have an effect on the diffraction pattern. A microscope image of the hydrogen jet of the FLASH experiment is shown in fig. 4.8. It becomes evident that the jet does

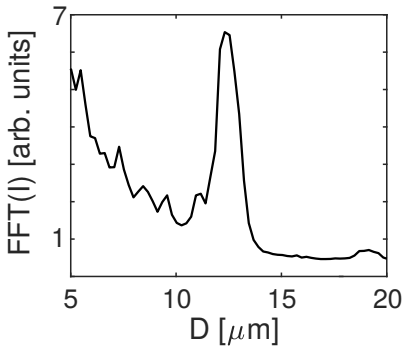

Figure 4.7.: Average 1D Fourier transform of single-shot diffraction patterns from fig. 4.6 (and seven additional patterns from the experiment described in the text) along Θ. The peak around 12 μm lies very close the predicted jet size of 10 μm.

Figure 4.8.: Microscope image of the 10 μm jet imaged in the jet scattering experiment described in more detail in the text.

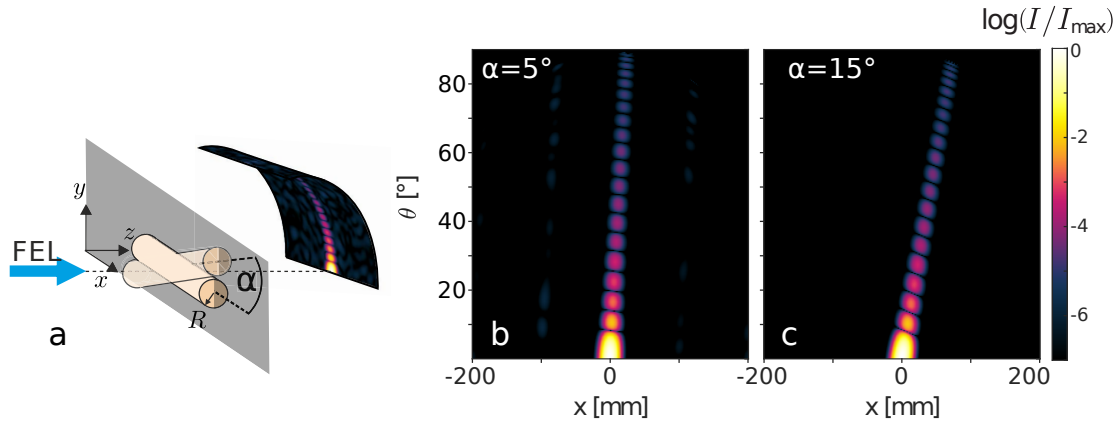

Figure 4.9.: a) Sketch of cylindrical jet rotated in x-y-plane (indicated in gray), with rotation angle α. Diffraction patterns obtained with MSFT for radius $R = 100\,\text{nm}$ and a wavelength of $\lambda = 13.5\,\text{nm}$. The jet length is set to $\Delta x' = 10w$ and the laser spot size to $w = 100\,\text{nm}$. The cylinder is sliced into 100 slices and the dimensions of each Fourier transform are 1024×1024. The rotation angles are $\alpha = 5\,^\circ$ (b) and $15\,^\circ$ (c).

not have an ideal cylindrical shape, it rather looks like a combination of spheres and cylinders. Further, it is not straight, which results in the jet in the interaction region not always being positioned perpendicular to the laser propagation direction, as assumed for the previous simulations. The role of structure and orientation of a jet is therefore investigated in the following.

4.2.2. Rotation of the jet

The analysis is carried out for the diffraction dominated regime, where the detector distance is much larger than the spot size of the incident laser pulse $D \gg w$. Therefore, the MSFT method is sufficient to compute the diffraction patterns as shown in fig. 4.4. The jet length is set to $\Delta x' = 10w$ with $w = 100\,\text{nm}$, the detector distance to $D = 280\,\text{mm}$ and the wavelength to $\lambda = 13.5\,\text{nm}$ for all calculations. First, the impact of different orientations of a cylindrical jet is investigated. Therefore, a cylindrical jet with radius $R = 100\,\text{nm}$ and different rotation angles α around the propagation direction is investigated, a sketch of the scenario is depicted in fig. 4.9a.
The resulting diffraction patterns are depicted in fig. 4.9b-c for $\alpha = 5\,^\circ$ and $\alpha = 15\,^\circ$, respectively. The rotation around the z-axis or laser propagation axis results into the equivalent rotation of the diffraction pattern around the same angle. Such a behavior can also be seen in the experimental diffraction patterns in fig. 4.6a and c, where the straight Mie streaks show a tilting around the laser propagation axis.

Further, the jet can be tilted inside the scattering plane, this is sketched in fig. 4.10a. The rotation angle γ describes the rotation around the y-axis. Figure 4.10b-g shows diffraction patterns for different γ. The upper panel corresponds to a cylinder radius of $R = 50\,\text{nm}$, and the lower panel to $R = 100\,\text{nm}$. Two observations can be made from the

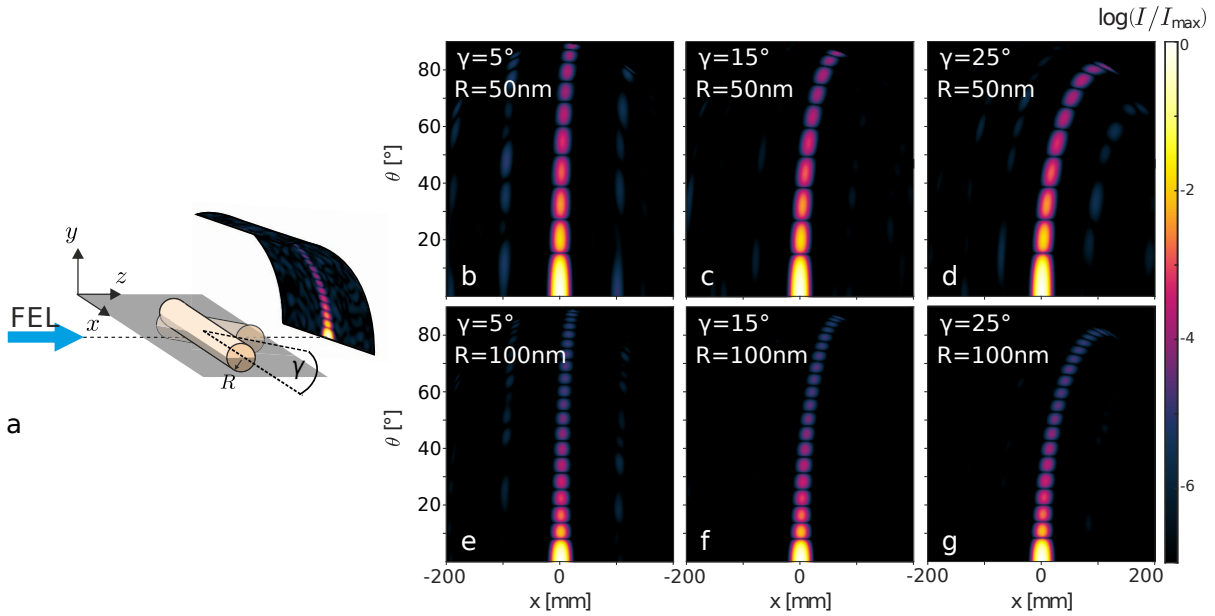

Figure 4.10.: a) Sketch of a cylindrical jet rotated in x-z-plane (indicated in gray) about an angle γ. Diffraction patterns b)-g) are computed with MSFT with a wavelength of $\lambda = 13.5\,\text{nm}$. The jet length is set to $\Delta x' = 10w$ and $w = 100\,\text{nm}$. Radii and rotation angles are indicated in the upper left corners of each diffraction pattern.

plots. First, the rotation around the y-axis leads to a bending of the Mie streak. The larger the rotation angle is, the more curved the streak gets. Second, the radius does not have an impact on the bending. Since in the experiment only scattering angles from 21 ° to 24.5 ° are visible such a bending cannot be observed.

4.2.3. Jet breakup

After some time after the creation of the hydrogen jet, it breaks up, ultimately into droplets, which is called Rayleigh breakup. This behavior is imitated by two cylinders separated by a distance d, such a jet is displayed in fig. 4.11a. The diffraction patterns for a $R = 100\,\text{nm}$ jet in dependence on different d are shown in figs. 4.11b-d. The space in between the cylinders leads to a signal with fringes next to the streaks. The fringe distance gets smaller, the larger the space between the two cylinders gets. For $d = 100\,\text{nm}$ the signal appears as multiple streaks left and right to the main streak, where the fringes are aligned. Such patterns can also be seen, when comparing to the experimental diffraction patterns, especially fig. 4.6c shows very bright streaks with less bright streaks to the left and right with the same fringe structure.
Another possibility that can be investigated is that part of the broken up jet rotates and then is differently oriented than the other part of the jet. Such a system is sketched in fig. 4.11e, where the angle α describes the rotation around the z-axis. Diffraction patterns for $d = 100\,\text{nm}$ are computed for different rotation angles. The results are shown

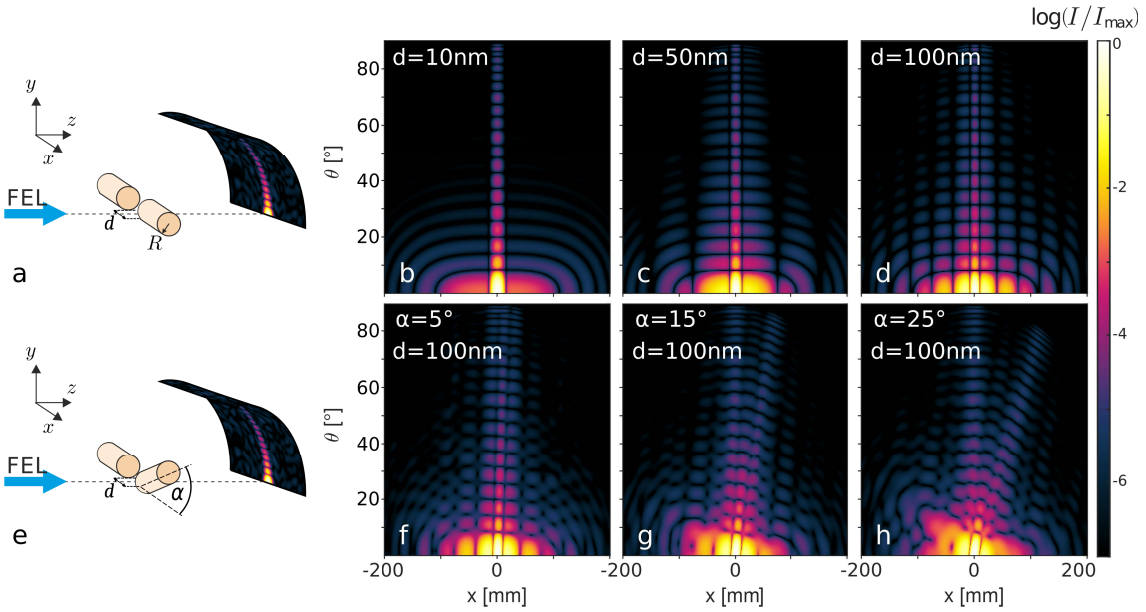

Figure 4.11.: a) Sketch of a cylindrical jet with radius R that is broken up with a distance d. e) Sketch of the same scenario with the right cylinder rotated around the x-axis around rotation angle α. Diffraction patterns b)-d),f)-h) are computed with MSFT with and a wavelength of $\lambda = 13.5\,\mathrm{nm}$. The jet length is set to $\Delta x' = 10w$ and $w = 100\,\mathrm{nm}$. The radius is set to 100 nm. The first row diffraction patterns correspond to the sketch in a, the second row to e. The radii and/or rotation angles are indicated in the upper left corners of each plot.

in figs. 4.11f-h. The diffraction patterns show the same signature of less bright signal beside the main streak as seen in fig. 4.11d. In fig. 4.11f it seems like the main streak is rotated by an angle of 5 °. However, figs. 4.11g and h clarify that the scattering pattern is an overlay of a straight and rotated streak, emerging from not rotated and rotated part of the jet. Thus, if parts of the jet are rotated differently, the diffraction pattern can have streaks with different directions. This effect can be seen in the experimental scattering image fig. 4.6b, e. g. by comparing the streaks around $(\Theta, x) = (22\,^\circ, -0.4\,\mathrm{cm})$ and $(\Theta, x) = (22\,^\circ, -0.2\,\mathrm{cm})$.

4.2.4. Modulation of jet surface

Last, the surface modulation of the jet (cf. fig. 4.8) is implemented as an oscillating jet radius as sketched in fig. 4.12a, i. e. a cylindrical shape with the surface described as sine function with a certain depth $R_{\mathrm{out}} - R_{\mathrm{in}}$ (outer minus inner radius) and the period Δ. Scattering images for $R_{\mathrm{in}} = 100\,\mathrm{nm}$ and different R_{out} and Δ are depicted in figs. 4.12b-g. Figure 4.12b shows that the modulation of the jet surface leads to the appearance of less bright streaks left and right to the main streak, with decreasing brightness the further away from the main streak. Additionally, the fringe positions are alternating for streaks directly next to each other. Comparing fig.4.12b and e shows that a larger outer radius

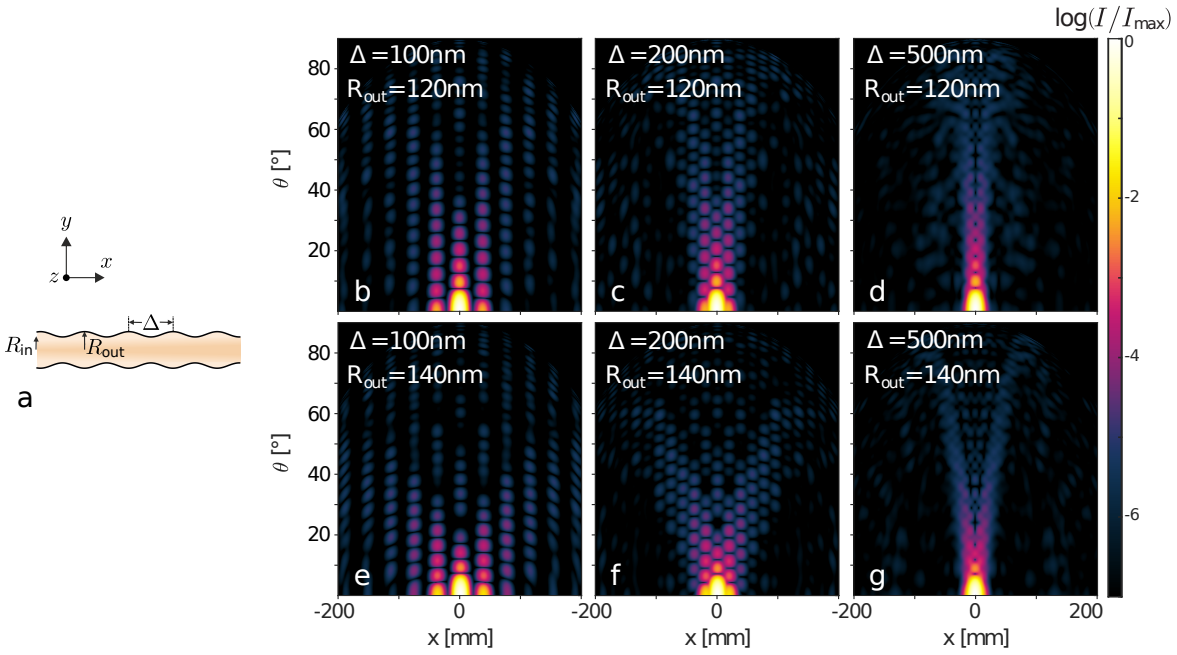

Figure 4.12.: a) Sketch of a cylindrical jet with radius R_{in} with periodic surface modulation of height R_{out} and period Δ. Diffraction patterns b)-g) are computed with MSFT with and a wavelength of $\lambda = 13.5\,\text{nm}$. The jet length is set to $\Delta x' = 10w$ and $w = 100\,\text{nm}$. The inner radius is set to $R_{\text{in}} = 100\,\text{nm}$. The modulation parameters are indicated in each upper left corner of the plots.

does not influence the distance between the streaks, but leads to streaks being visible further away from the main streak. Figures 4.12b-d and e-g, respectively, show that for increasing Δ, the distance between the streaks decreases. Due to the overlay of the streaks the fringes are blurring for $\Delta = 500\,\text{nm}$. Comparing figs. 4.12b and e, c and f, and d and g, shows that a larger outer radius leads to the streaks further away from the main streak being visible up to larger scattering angles and the main streak being visible up to smaller scattering angles. This leads to a 'V'-shaped streak structure for $R_{\text{out}} = 140\,\text{nm}$. Such a streak structure cannot be observed in the experimental diffraction patterns.

In summary, the jet shape has a large impact on the diffraction pattern. First, a rotation of the jet can lead to a rotation of the diffraction pattern or a bending of the Mie streaks. Second, a Rayleigh breakup can lead to additional streaks appearing next to the main streak due to the scattering by the slit occurring because of the breakup. Third, the modulation of the jet surface can lead to additional streaks beside the main streak with a 'V'-like structure of the streaks. Although a few of the investigated effects could be recognized in the experimental images it cannot be verified if the effects in the experimental diffraction pattern actually result from these jet structures, or if they result from the noisy FEL spectrum. However, it could be verified that the jet shape has a large impact on the diffraction pattern and single-shot diffractive imaging is a valuable tool to characterize the jet shape and structure. The experiment could be improved by

performing it at a seeded FEL with a well behaved spectrum that allows for a simpler analysis and interpretation of diffraction patterns.

5. Coherent diffractive imaging of single helium nanodroplets with a high harmonic generation source

Free electron lasers are large size facilities and only a few exist all over the world. The access to the few facilities is limited and the execution time of experiments always is confined to just a few days. Lab-based single-shot diffractive imaging experiments would therefore be a huge improvement for scientists. Although, the brightness of high harmonic generation (HHG) sources is magnitudes lower than of free electron lasers [83], they are a promising light source to fulfill this dream. HHG sources offer the possibility to perform experiments with zero jitter and they generate phase-stable multicolor pulses that can possibly be utilized for time-resolved measurements with attosecond pulse trains and isolated attosecond pulses. Further, lab-based experiments can be conducted over a longer time span allowing for large parameter scans. Diffractive imaging experiments with HHG pulses on supported particles have already been demonstrated for 2D artificial objects with multiple exposure [116, 101, 145] and in single-shot mode [101, 23], and on 3D objects with a very high resolution of 22 nm [121]. Lab HHG experiments on free nanoparticles were lacking, though this target class is of particular interest for investigation of structure formation, particle growth and light-induced dynamics.

This chapter describes the framework and my contribution to the first successful lab-based single-shot diffractive imaging experiment on free-flight helium nanodroplets utilizing a HHG source. The experiment has been conducted by Nils Monserud and Daniela Rupp *et al.*. In the following, the basics of high harmonic generation are recalled to point out that a multicolor-analysis is required for experiments with HHG radiation. Second, the single-shot diffractive imaging experiment is outlined and third, the multicolor analysis is presented in detail. The analysis is basically divided into two parts. First, optical properties of helium nanodroplets are extracted by multicolor simplex Mie fits of spherical droplets and second, 3D information about the shape of non-spherical helium droplets is identified by evaluating the wide angle scattering data from the XUV (extreme ultraviolet) diffraction patterns via forward fits utilizing the multislice Fourier transform method (MSFT) and the complex scaling discrete dipole approximation (CSDDA). In this regime, phase retrieval algorithms are not applicable, because on the one hand, absorption is not negligible and second the diffraction pattern contains scattering signal from multiple frequencies. The multicolor analysis is published in [109].

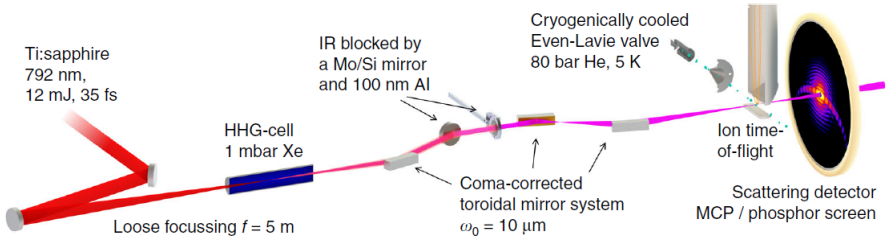

Figure 5.1.: Setup of the high harmonic generation (HHG) single-shot diffractive imaging experiment. A Ti:sapphire laser pulse is focused into a HHG-cell filled with xenon gas. The generated HHG radiation is focused into the interaction region with a toroidal mirror system. The IR is blocked by Mo/Si mirrors. Helium nanodroplets are generated by supersonic expansion through a cryogenic 5 K valve with a pressure of 80 mbar. After the HHG pulse hit the helium droplets the ions are detected with a time-of-flight spectrometer and the scattered photons are recorded with a micro-channel plate (MCP) detector combined with a phosphor screen. Figure from [109].

5.1. High harmonic generation

The high harmonic generation (HHG) process due to the interaction of an atomic gas with a high-intensity infrared laser can be described via the three-step model [24]. First, due to the interaction with the laser field (with an electric field amplitude comparable to the electric field in atoms) an electron can tunnel through its atomic core potential. Second, the freed electron gets accelerated in the laser field away from the core. Third, as the laser field changes its direction the electron gets accelerated back to the core and recombines with it, emitting a photon whose energy depends on ionization potential and photon energy of the driving laser. For this process laser intensities on the order of $10^{14}\,\mathrm{W/cm^2}$-$10^{15}\,\mathrm{W/cm^2}$ are required. In every laser half-cycle an attosecond pulse is generated that consists of multiple odd harmonics of the incident laser frequency. Therefore, attosecond imaging experiments enabled by attosecond HHG pulses will rely on a multicolor analysis for extracting useful information from the diffraction patterns.

5.2. Single-shot x-ray diffractive imaging with a high harmonic generation source

A schematic overview of the experimental setup of the HHG single-shot diffractive imaging experiment is depicted in fig. 5.1. A Ti-Sapphire laser with a central wavelength of 792 nm with a pulse duration of 35 fs and a pulse energy of 33 mJ at a repetition rate of 1 kHz, is focused into a xenon gas-cell. The interaction of the near-infrared (NIR) laser pulse with the xenon atoms results into the generation of high harmonics. In the experiment the HHG pulse achieves output energies of about 2 μJ, corresponding to a very high conversion efficiency of 1.6×10^{-4} and average power of 2 mW. The HHG pulse consists of four harmonics, the 11th (72 nm, 17.2 eV), the 13th (61 nm, 20.4 eV), the 15th (53 nm, 23.5 eV) and the 17th (47 nm, 26.6 eV). The numbers in brackets denote corresponding wavelengths

and photon energies. The pulse duration is $\tau \approx 20\,\text{fs}$. The HHG pulse is focused into the interaction chamber via a micro-focusing setup [39]. The IR intensity is decreased in the reflection from a Si mirror and subsequently blocked by an aluminum filter. The helium droplets are generated by expansion of high-purity ^{4}He at a pressure of 80 bars and are expected to be superfluid. The helium nanodroplets to be imaged are guided into the interaction chamber through a conical skimmer. In the interaction region the HHG pulse hits preferably a single helium nanodroplet and the scattered light is amplified using a large micro-channel plate (MCP) (∅: 75 mm) with a center hole (∅: 3 mm) combined with a phosphorus screen that converts the signal to optical light, which then is recorded on a shot-to-shot basis with an out-of-vacuum camera. From 3×10^5 measurements, 2300 single-shot diffraction patterns showed distinct structures and 12700 weak, unstructured signal. These statistics indicate that the experiment was conducted in the single-particle limit. As already mentioned, the diffraction patterns are obtained with a multi-frequency pulse. The average spectrum measured of the HHG light beam is depicted in fig. 5.2a and shows that the 13th and 15th harmonic have the largest signal and therefore are expected to contribute most to the scattered field. Figure 5.2b sketches the corresponding refractive indices of the frequencies with $n = \delta - i\beta$ (light grey: δ, dark grey: β) assembled from bulk liquid helium measurements (solid lines) [130, 78] and tabulated values from the NIST database (scatter) [19]. The refractive indices of the 13th and 15th harmonic lie very close to the helium 1s2p resonance at 20.4 eV. For helium nanodroplets they are expected to largely depend on the droplet size in this regime [66]. The existence of multiple harmonics in the spectrum complicates the analysis, but is unavoidable if attosecond pulse trains or isolated attosecond pulses are generated [70]. The analysis gets complicated further by the unknown refractive indices of two harmonics being very close to a resonance. In the following section, a multicolor fit to extract optical properties of helium from the experimental data is presented by utilizing a simplex optimization for spherical diffraction patterns, where the intensity of each harmonic can be computed utilizing Mie theory.

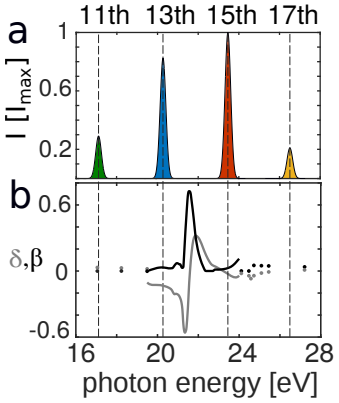

Figure 5.2.: a) Measured average high harmonic generation (HHG) radiation spectrum with four harmonics in extreme ultraviolet, the harmonic order is indicated above each peak. b) Sketch of real and imaginary part of refractive index $n = 1 - \delta + i\beta$ of bulk liquid helium. Solid lines from measurements [130, 78], scatters from tabulated values (NIST database, http://physics.nist.gov/PhysRefData/FFast/html/form.html). Figure from [109].

5.3. Multicolor simplex Mie fits

The diffraction patterns of the helium nanodroplets are obtained with four frequencies at once, where the refractive indices of two harmonics are close to the 1s2p resonance of helium. The refractive indices of these harmonics are expected to depend on the droplet radius [66], the remaining refractive indices are expected to be close to the values for bulk helium. Therefore, in this section, a fit routine is presented to extract the uncertain optical properties of the 13th and 15th harmonic from the diffraction patterns. To this end, diffraction patterns that can be directly assigned to a spherical shape are selected from the data. This is the case for scattering images with spherical fringes stemming from Mie scattering (which are $\approx 76\,\%$ of the scattering images). In total 18 suitable diffraction patterns are singled out.

Since the diffraction patterns are radially symmetric it is sufficient to only consider their radial integrals. The radial integral can be described as sum of scattered Mie intensities from the four harmonics via

$$\begin{aligned} I_{\text{fit}} =& c_{11} I_{\text{mie},11}(R, \delta_{11}, \beta_{11}) + c_{13} I_{\text{mie},13}(R, \delta_{13}, \beta_{13}) \\ &+ c_{15} I_{\text{mie},15}(R, \delta_{15}, \beta_{15}) + c_{17} I_{\text{mie},17}(R, \delta_{17}, \beta_{17}), \end{aligned} \tag{5.1}$$

where c_j is a scalar that adjusts the ratio by which the jth harmonic contributes to the total signal. The Mie intensities $I_{\text{mie,j}}$ of each harmonic are a function of droplet radius R and refractive index $n = 1 - \delta_j + i\beta_j$. Hence, the total scattered signal is dependent on the intensity ratios, the cluster radius and the refractive indices corresponding to the four harmonics. By fitting eq. (5.1) to the radial profiles it is possible to extract these parameters. Such a multidimensional fit can be performed by the simplex algorithm (or Nelder-Mead method) [90], which is an iterative search algorithm seeking the minimum of a n-dimensional function. In this analysis, the error which is defined via

$$\epsilon = \frac{\sum(\log(I_{\text{exp}}) - \log(I_{\text{fit}}))^2}{\sum(\log(I_{\text{exp}}))^2}, \tag{5.2}$$

is minimized where I_{exp} denotes the radial integral from the experimental diffraction pattern. To compute the Mie intensities in each simplex iteration the Mie theory is utilized. It is an efficient and fast method to compute scattered electric fields from spherical targets applicable to all wavelengths, sizes and refractive indices. The method is described in more detail in app. B.

For performing the simplex Mie fits on the 18 diffraction patterns, first, the experimental diffraction patterns have to be converted to be comparable to Mie theory. Therefore, the correct center of each diffraction pattern needs to be found and the nonlinear detector efficiency of the MCP detectors needs to be taken into account. These steps are described in the following subsection. Afterwards, the converted diffraction patterns are fitted with the simplex routine. First, it is shown that no reliable fit result can be found when fixing

the refractive indices to the values for bulk helium. Then, in the third part of this section, the optical properties of 13th and 15th harmonic are fitted. To this end, a Monte Carlo sampling is incorporated into the simplex Mie fit to sufficiently cover the large parameter space.

5.3.1. Preparing the multicolor scattering images

For fitting the multicolor scattering images with a simplex Mie fit, the radial profiles have to be computed by angular averaging. However, the center of the diffraction patterns varies from shot-to-shot due to wavefront tilts at the droplet positions. To this end, the correct center of the diffraction patterns needs to be obtained before computing the radial integral. Further, the MCP detector exhibits a nonlinear detection efficiency due to saturation effects. Therefore, a nonlinearity function is introduced to compensate for this.

Radial profiles for fluctuating centers

The position of the center of the diffraction pattern varies from shot to shot and influences the shape of the radial profile. The correct center can be found by fitting the analytical solution for the scattered intensity of a sphere to each experimental diffraction pattern. Neglecting absorption, the scattered intensity of a sphere I_{sph} with radius R in dependence on the distance to the center r reads (cf. eq. (2.54))

$$I_{\mathrm{sph}}(r) \propto \frac{(\sin(q(r)R) - qR\cos(q(r)R))^2}{q(r)^6}, \tag{5.3}$$

where the momentum transfer can be expressed via $q(r) = k\frac{r}{z} = k\frac{\sqrt{(x-x_m)^2+(y-y_m)^2}}{z}$ The wave number is denoted by k, the center point by (x_m, y_m) and the detector distance by z. In the following the ratio of size parameter kR and z are set to the constant $c = kR/z$, which is a scalar that affects the fringe distance of the diffraction pattern. Inserting this into eq. (5.3) and assuming the experimental data having a constant noise level I_{noise} yields

$$I_{\mathrm{sph}}(r) = I_{\mathrm{noise}} + I_{\mathrm{max}}R^6\frac{\sin(cr) + cr\cos(cr)}{(cr)^6}, \tag{5.4}$$

where $r = r(x, y, x_m, y_m)$ depends on pixel position (x, y) and center point (x_m, y_m). This equation is applied to fit each experimental diffraction pattern by minimizing $\epsilon = \sum(\log(I_{\mathrm{exp}}) - \log(I_{\mathrm{sph}}))^2$. The fit parameters are the droplet radius R, the noise level I_{noise}, the maximum intensity I_{max} and the center point (x_m, y_m). The fit is performed with a simple least square approach. Useful information about the droplet size, however, cannot be obtained from this fit, since absorption is not included and the light frequency is only included as effective fringe distance. Figure 5.3a shows one spherical diffraction pattern from the set of 18 experimental patterns and fig. 5.3b shows the corresponding

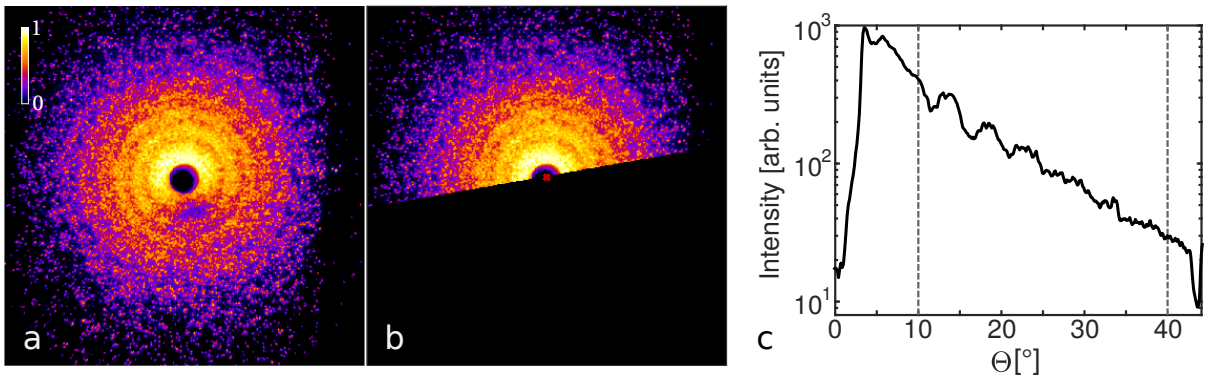

Figure 5.3.: a) Example diffraction pattern of spherical helium droplet from experiment of fig. 5.1 b) diffraction pattern with fitted center (red cross) and mask applied to compute the radial profile obtained by radial integration (c). Details on fit procedure to find the center are described in the text. Parts of the figure are published in supplementary material of [109].

fitted center as red cross. For computing the radial profile and fitting the center only the upper part of the diffraction pattern shown in fig. 5.3b is taken into account. As can be seen in fig. 5.3a, the lower part of the diffraction pattern shows a dent in the scattered intensity, which is present in each diffraction pattern due to the detector geometry. The MCP detector consists of electron multiplying channels that are tilted by 8 °, resulting in scattered photons arriving at this angle hitting the electron multiplier not as efficiently as under other scattering angles. Hence, in this area, the scattered intensity seems to be lower than it actually is and is not useful for the analysis. The resulting radial profile obtained from fig. 5.3b is depicted in fig. 5.3c. Around the detector hole, through which the unscattered high intensity laser beam is led, the radial profile is not evaluable due to saturation effects of the detector. Therefore, for the simplex Mie fits the radial profile is evaluated from 10 ° to 40 ° for the following analysis, illustrated by the dashed grey lines.

Nonlinear detection efficiency

The obtained radial profiles need to be corrected for the nonlinear detection efficiency of the MCP [10, 14]. It has been shown that the saturation effect can be characterized by an exponential efficiency function [10] via

$$I_{\mathrm{det}} = I_{\mathrm{exp}}^{\alpha}, \tag{5.5}$$

where I_{det} is the intensity obtained on the detector, I_{exp} the true experimental intensity, and α denotes the nonlinearity factor. To estimate the nonlinearity factor the radial integral from fig. 5.3c is compared to Porod's power law (cf. eq. (2.55)) with different nonlinearity factors, depicted in fig. 5.4. The calculation of the momentum transfer corresponds to the 15th harmonic with the supposedly highest contribution to the scattering signal. The best agreement with Porod's law (dashed black line) can be found for $\alpha = 0.5$. This value is used in the following to compute the true experimental intensity from the

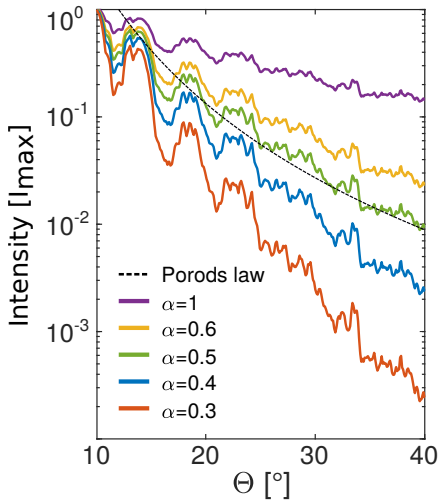

Figure 5.4.: Radial profile of fig. 5.3c with different nonlinearity factors α. The solid black line shows the intensity decay according to Porod's law ($I \propto q^{-4}$, cf. eq. (2.55)).

radial profiles.

Note that a diffraction pattern taken with a single frequency far from a resonance would be more convenient to predict the nonlinearity factor, since Porod's law only is applicable to weak scattering where absorption is negligible.

5.3.2. Fits of literature values

The 18 radial profiles with corrected intensity now can be fitted with the simplex Mie fit routine. The goal is to fit the optical parameters close to the 1s2p resonance of helium, since they are expected to be size dependent. However, first, the case that the literature values for bulk helium can reproduce the experimental results needs to be considered. Therefore, the intensity ratios c_{11}, c_{13}, c_{15} and c_{17} are fixed according to the average spectrum (cf. fig. 5.2a)

$$\begin{aligned} c_{11} &= 0.21 \\ c_{13} &= 0.82 \\ c_{15} &= 1.0 \\ c_{17} &= 0.29, \end{aligned}$$

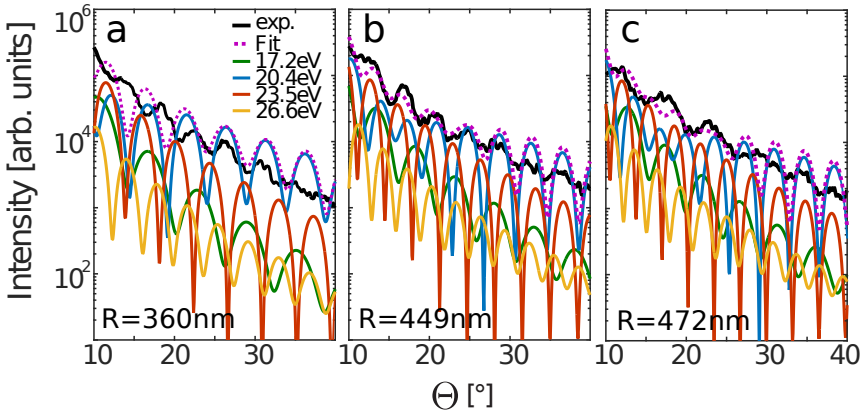

Figure 5.5.: Exemplary simplex Mie fit results for three measured radial profiles. Fit parameter is the droplet radius, refractive indices are fixed to $n_{11} = 0.97 + i0$, $n_{13} = 1.14 + i0.032$, $n_{15} = 1.03 + i0.029$ and $n_{17} = 1.0036 + i0.041$ according to the literature values for bulk liquid helium (fig. 5.2b). Intensity ratios are fixed to $c_{11} = 0.21$, $c_{13} = 0.82$, $c_{15} = 1.0$ and $c_{17} = 0.29$ according to the HHG spectrum (fig. 5.2a).

and the refractive indices are interpolated from the literature values depicted in fig. 5.2b and are

$$\begin{aligned} n_{11} &= 0.97 + i0 \\ n_{13} &= 1.14 + i0.032 \\ n_{15} &= 1.03 + i0.029 \\ n_{17} &= 1.0036 + i0.041. \end{aligned}$$

The only fit parameter then is the droplet radius R. The starting parameters for each simplex fit are randomly chosen between 300 nm and 600 nm. The fit results for three radial profiles are depicted in fig. 5.5. It can be seen that no fit matching the experimental data can be found with the refractive indices fixed to the literature values and the intensity scalings fixed according to the average HHG spectrum. Therefore, in the following, the intensity ratios are taken as additional fit parameters. The corresponding starting parameters are chosen between 0 and 1. The refractive indices of the four harmonics are again fixed to the literature values (cf. fig. 5.2b). Resulting fits for three selected radial profiles are shown in fig. 5.6. All 18 fits are depicted in the appendix fig. C.1. The fitted radial profiles describe the characteristics of the experimental data quite well, however, looking at the fitted intensity ratios for the 18 diffraction patterns, depicted in fig. 5.7, the intensities of the four harmonics are fluctuating a lot. The 17th harmonic gives the highest contribution to the signal for 14 of the diffraction patterns, which is not expected when comparing to the spectrum obtained in the experiment (cf. fig. 5.2), where the 17th harmonic has the lowest contribution. This indicates that the fit results do not correspond to a physically meaningful set of parameters. Hence, the

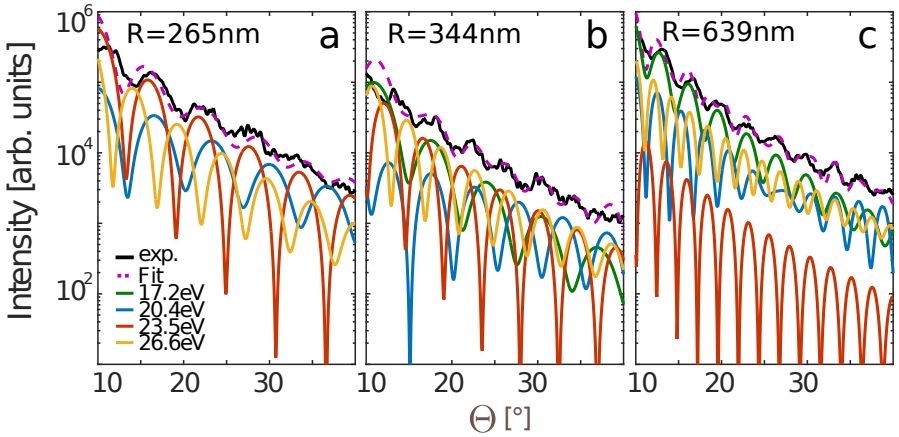

Figure 5.6.: Exemplary simplex Mie fit results for three radial profiles. Fit parameters are the droplet radius and the intensity ratios. Refractive indices are fixed to $n_{11} = 0.97 + i0$, $n_{13} = 1.14 + i0.032$, $n_{15} = 1.03 + i0.029$ and $n_{17} = 1.0036 + i0.041$ according to the literature values for bulk liquid helium (fig. 5.2b). Parts of Figure published in supplementary material of [109].

refractive indices fixed to the literature values of bulk helium do not reflect the optical constants for liquid helium droplets. Therefore, the intensity ratios are fixed according to fig. 5.2a to the average HHG spectrum in the following. Note that although here the fitted intensity ratios fluctuate unrealistically strong, it becomes evident that they have a large influence on the diffraction pattern and therefore need to be measured from shot-to-shot in future experiments. The refractive indices of the 11th and 17th harmonic lie far away from the 1s2p resonance of helium and therefore are well known and are fixed to their literature values (cf. fig. 5.2b) in the following. The refractive indices of the 13th and 15th harmonic, however, are very close to the resonance and therefore are expected to vary with droplet radius. They are fitted along with the droplet radius in the following, resulting into five fit parameters.

5.3.3. Fits of optical properties

For fitting the optical properties of the 13th and 15th harmonic along with the droplet radius, the simplex Mie fit needs to be performed with five fit parameters. Usually such a large parameter space results into an error map with many local minima. Unfortunately, with the simplex optimization it cannot be circumvented to end up in a local and not the real global minimum when performing the minimization. The located minimum depends on the starting parameters, i. e. different starting parameters can result in different fitted parameters corresponding to a certain local minimum. In the following a Monte Carlo sampling is implemented to scan the large parameter space and find the actual global minimum. To this end, first a typical error map is examined to verify the necessity of such a sampling. Second, the number of necessary Monte Carlo steps is estimated by a bootstrap method. Last, the optical properties of helium droplets for the 13th and 15th harmonic of the HHG pulse are fitted utilizing the Monte Carlo sampling simplex Mie fit.

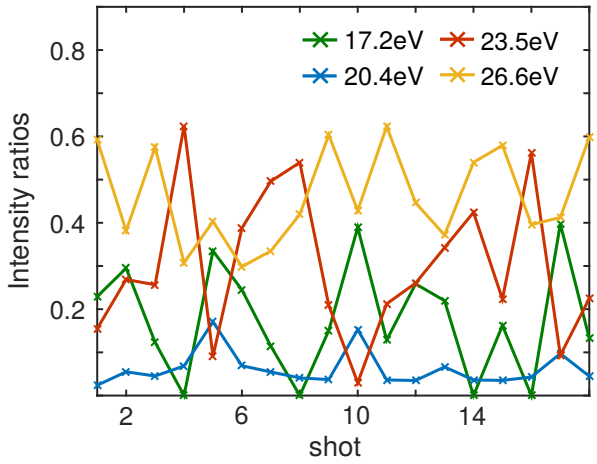

Figure 5.7.: Intensity ratios corresponding to simplex Mie fits of the 18 selected diffraction patterns. Published in supplementary material of [109].

Monte Carlo sampling

In the following, a typical structure of the error landscape of the large parameter space is analyzed to check how densely the parameter space needs to be scanned to find the global minimum. To additionally investigate the interrelations of the refractive indices of the 13th and 15th harmonic, the error (eq. (5.2)) is characterized on the example of one selected radial profile (fig. 5.3c) for different δ_{13} and δ_{15}. The radius and imaginary parts of the refractive indices are fixed to $R = 344\,\mathrm{nm}$, $\beta_{13} = 0.032$ and $\beta_{15} = 0.029$. The refractive indices of the 11th and 17th harmonic are now and in the following fixed to $n_{11} = 0.97 + i0$ and $n_{17} = 1.0036 + i0.041$ according to the literature values for bulk liquid helium (cf. fig. 5.2b). The resulting error map is depicted in fig. 5.8. Two main observations can be made from the plot. (i) As expected, multiple local minima exist, a large global minimum can be found around $\delta_{13} = \delta_{15} = 0.1$. (ii) A mirror axis at $\delta_{13} = \delta_{15}$ can be seen. This structure of the error map indicates that the 13th and 15th harmonic can interchange their roles in the contribution to the diffraction pattern. To find the real global minimum in the ensemble of local minima, the simplex fit procedure is started with multiple sets of starting parameters. This is done by starting with random parameters in certain limits, which is referred to as Monte Carlo sampling in the following. The limits are set to these values for the fit parameters:

$$\begin{aligned} R_{\mathrm{min}} &= 300\,\mathrm{nm} \quad \text{to} \quad R_{\mathrm{max}} = 600\,\mathrm{nm} \\ \delta_{\mathrm{min}} &= -0.3 \quad \text{to} \quad \delta_{\mathrm{max}} = 0.2 \\ \beta_{\mathrm{min}} &= 0 \quad \text{to} \quad \beta_{\mathrm{max}} = 0.07 \end{aligned}$$

The fit parameters corresponding to the global minimum then are the ones for the Monte Carlo step with the lowest error. To test how many Monte Carlo steps are required to find

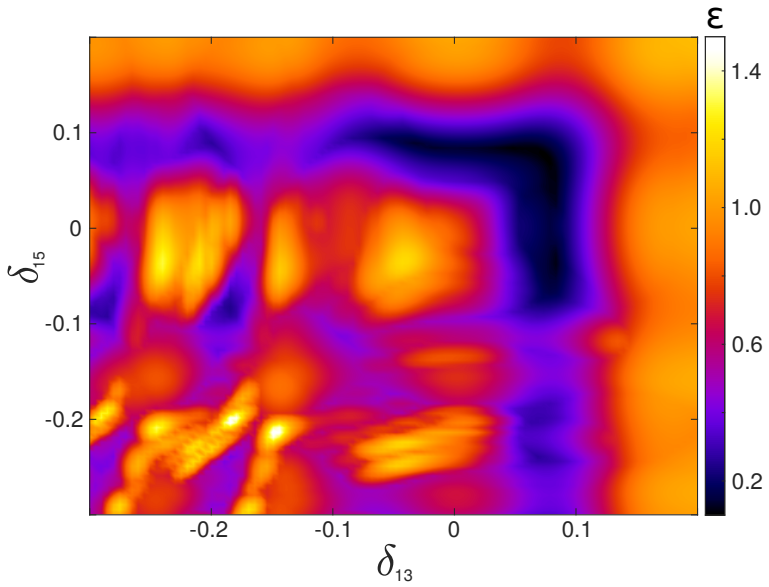

Figure 5.8.: Error map for different δ_{13} versus δ_{15} for radial profile fig. 5.3c with fixed radius $R = 343.6\,\text{nm}$ and $\beta_{13} = 0.032$ and $\beta_{15} = 0.029$. The refractive indices of the 11th and 17th harmonic are set to the literature values $n_{11} = 0.97 + i0$ and $n_{17} = 1.0036 + i0.041$, the intensity ratios are set to $c_{11} = 0.21$, $c_{13} = 0.82$, $c_{15} = 1.0$ and $c_{17} = 0.29$ according to the HHG spectrum (fig. 5.2a).

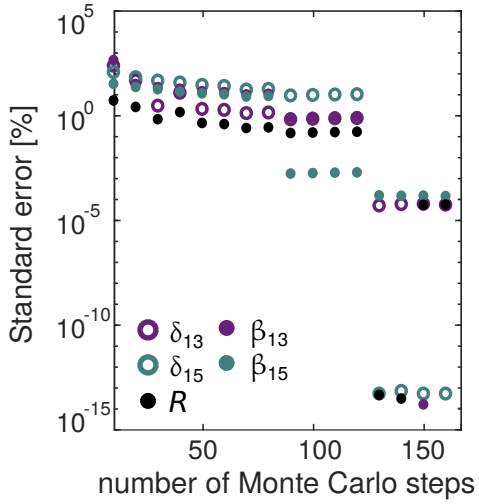

Figure 5.9.: Standard error (eq. (5.6)) versus number of Monte Carlo steps for the five fit parameters radius, and real and imaginary part of the 13th and 15th harmonic of the HHG pulse, respectively.

the real global minimum, a bootstrap method is applied to the experimental diffraction pattern from fig. 5.3. This is done as follows. The simplex fit with random starting parameters is computed for a certain number of Monte Carlo steps. Such a run results into one set of fitting parameters corresponding to the lowest error. This is repeated B times, resulting into B sets of fitting parameters, for which a standard error can be computed via

$$\epsilon_{\mathrm{se}} = \sqrt{\frac{1}{B}\sum(x-\bar{x})^2}, \tag{5.6}$$

where x denotes the fit parameter and $\bar{x}$ its average. If a certain number of Monte Carlo steps gives the same set of fit parameters in each run, the standard error will be zero. The standard error for different number of Monte Carlo steps is shown in fig. 5.9 for the five fit parameters, respectively. It can be seen that the error drops at 130 Monte Carlo steps to 10^{-5} for δ_{13}, β_{15} and the radius and to 10^{-15} for δ_{15} and β_{13}. Hence, in the following, the number of Monte Carlo steps is set to 150 to ensure finding the real global minimum.

Fit results

The simplex fit procedure is performed for the 18 radial profiles with 150 Monte Carlo steps with random starting parameters in the same limits as before. Resulting Mie fits for three example radial profiles are depicted in fig. 5.10. All fit results are shown in the appendix, figs. C.2 and C.3. To each experimental radial profile Mie fits can be found where either the 13th or 15th harmonic has the main contribution to the total scattered signal. Figure. 5.10a-c shows the fits with the 13th harmonic dominating the signal and fig. 5.10d-f the corresponding fits with the 15th harmonic dominating. The corresponding fitted radii are indicated in the upper right corner of each plot. Radii for the 15th harmonic being dominant are larger compared to the fits with the 13th harmonic having the main contribution to the total signal. This indicates that the harmonics exchange their roles in the contribution to the total signal by slightly adapting the droplet radius. This is the case for all of the 18 fits, when looking at the radial distribution for the two cases, depicted in fig. 5.11. The fitted droplet radii for the 13th harmonic being dominant are slightly smaller than for the 15th harmonic having the main contribution to the scattering signal.
The fitted refractive indices are depicted in fig. 5.12a and b for the 13th harmonic and the 15th harmonic being dominant, respectively, as δ versus β plots. The values underline the behavior of the harmonics exchanging their role, as in fig. 5.12a and b the clouds of red (13th harmonic) and blue (15th harmonic) dots exchange their positions.
Figure 5.13a-d shows δ and β of 13th and 15th harmonic as a function of radius R for the 13th harmonic being dominant and fig. 5.13e-f the corresponding plots for the 15th harmonic being dominant. The solid black line in each plot shows a linear regression revealing a dependence of δ and β on the droplet radius. The imaginary parts of the refractive indices decrease with larger radii for all cases. The δ parameter for the dominating harmonic (see figs. 5.13a and f) decreases with larger radius, the δ parameter

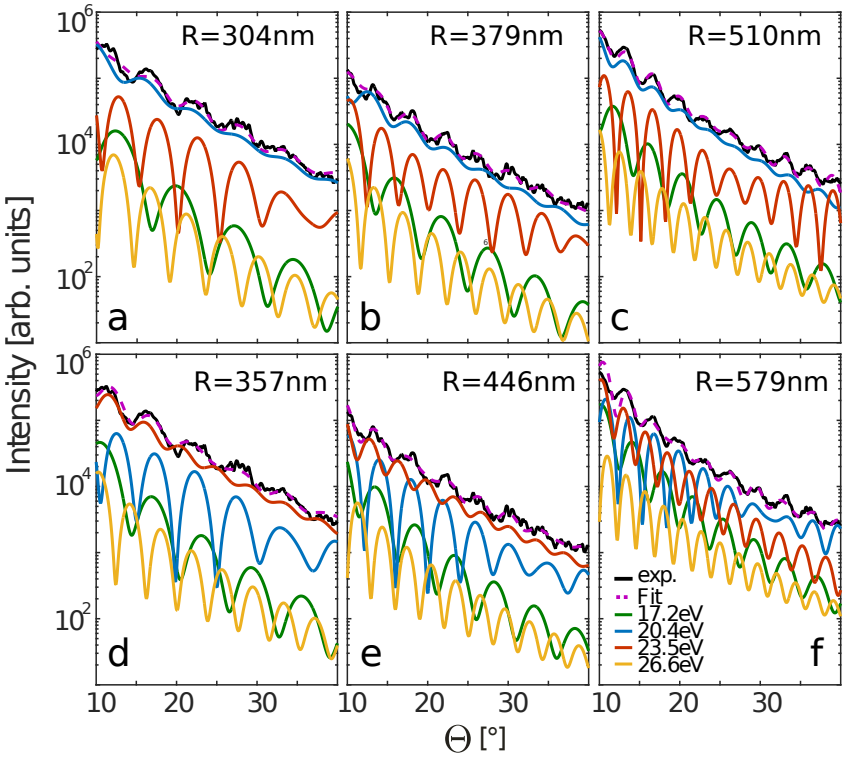

Figure 5.10.: Simplex Mie fit results for three selected radial profiles; a and d, b and e and c and f correspond to the same experimental radial profile, respectively. Fit parameters are the droplet radius and refractive indices of the 13th and 15th harmonic of the HHG pulse. The refractive indices of the 11th and 17th harmonic are fixed to $n_{11} = 0.97 + i0$ and $n_{17} = 1.0036 + i0.041$ according to the literature values for bulk liquid helium (fig. 5.2b). The intensity ratios are fixed to $c_{11} = 0.21$, $c_{13} = 0.82$, $c_{15} = 1.0$ and $c_{17} = 0.29$ according to the HHG spectrum (fig. 5.2a). a-c) Simplex Mie fits with 13th harmonic having the main contribution to the radial profile. d-f corresponding fits, where the 15th harmonic has the main contribution to the signal. Published in supplementary material of [109].

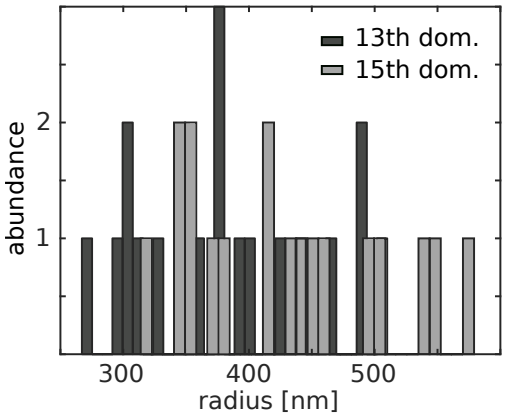

Figure 5.11.: Radial distribution of 18 simplex Mie fits. Fit parameters are droplet radius and refractive indices of the 13th and 15th harmonic of the HHG pulse, respectively. The refractive indices of the 11th and 17th harmonic are fixed to $n_{11} = 0.97 + i0$ and $n_{17} = 1.0036 + i0.041$ according to the literature values for bulk liquid helium (fig. 5.2b). The intensity ratios are fixed to $c_{11} = 0.21$, $c_{13} = 0.82$, $c_{15} = 1.0$ and $c_{17} = 0.29$ according to the HHG spectrum (fig. 5.2a). Dark gray indicated radii for fits where 13th harmonic has main contribution to the fit, light gray the radii for fits where 15th harmonic has main contribution to the fit. Published in supplementary material of [109].

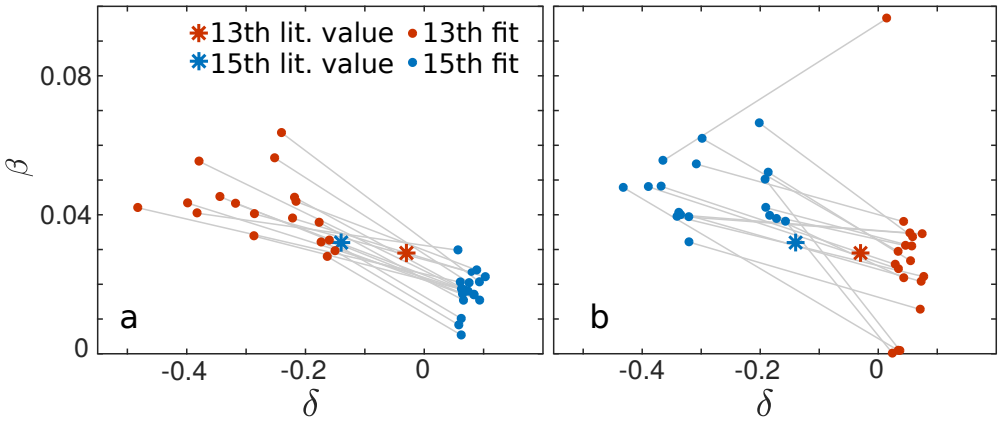

Figure 5.12.: Resulting refractive indices of 18 simplex Mie fits with fit parameters of droplet radius and refractive indices of the 13th and 15th harmonic of the HHG pulse, respectively. The refractive indices of the 11th and 17th harmonic are fixed to $n_{11} = 0.97 + i0$ and $n_{17} = 1.0036 + i0.041$ according to the literature values for bulk liquid helium (fig. 5.2b). The intensity ratios are fixed to $c_{11} = 0.21$, $c_{13} = 0.82$, $c_{15} = 1.0$ and $c_{17} = 0.29$ according to the HHG spectrum (fig. 5.2a). a) Resulting δ and β values for fit where 13th harmonic has main contribution to the radial profile. b) Resulting δ and β values for fit where 15th harmonic has main contribution to the radial profile. Published in supplementary material of [109].

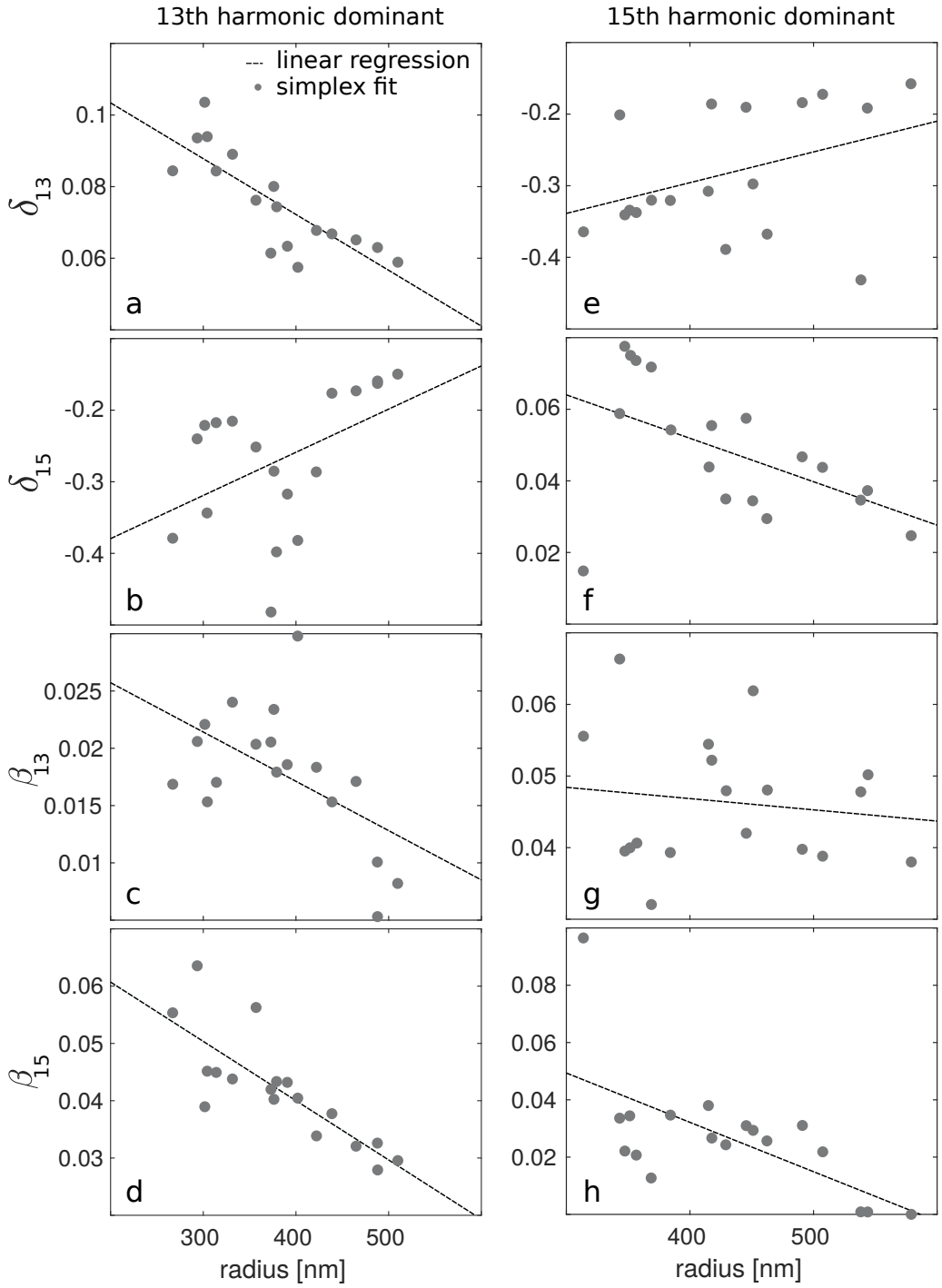

Figure 5.13.: Resulting refractive indices versus radius of 18 simplex Mie fits. Fit parameters are droplet radius and refractive indices of the 13th and 15th harmonic of the HHG pulse, respectively. The refractive indices of the 11th and 17th harmonic are fixed to $n_{11} = 0.97 + i0$ and $n_{17} = 1.0036 + i0.041$ according to the literature values for bulk liquid helium (fig. 5.2b). The intensity ratios are fixed to $c_{11} = 0.21$, $c_{13} = 0.82$, $c_{15} = 1.0$ and $c_{17} = 0.29$ according to the HHG spectrum (fig. 5.2a). Left column shows values for fit where 13th harmonic has main contribution to the radial profile, the right column the values for fit where 15th harmonic has main contribution to the radial profile.

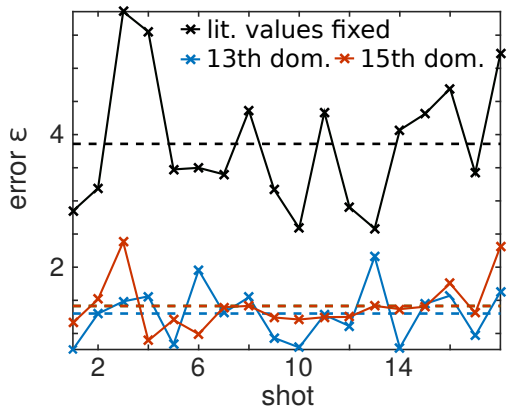

Figure 5.14.: Errors for each fit. Black: refractive indices fixed to literature values and intensity scalings c open. Intensity scalings fixed and refractive indices open, main contribution to Mie signal from 13th harmonic (blue) or 15th harmonic (red). Published in supplementary material of [109].

for the other harmonic (see figs. 5.13b and e) increase with larger radius. This behavior supports the tendency of the harmonics exchanging their roles in the Mie fit by simultaneously adapting the droplet radius and indicate a systematic size dependence. However, the remaining ambiguity of the two solutions needs to be resolved for a final conclusion.

To estimate whether one of the two possible solutions can be stated as more trustworthy, the error of the best fits for the two cases is analyzed, depicted in fig. 5.14 (blue denotes the 13th harmonic, red the 15th harmonic giving the main contribution to the signal). It can be seen that on the one hand the average error for the 13th harmonic being dominant is slightly smaller than for the 15th harmonic being dominant. Note that both solutions always deliver errors smaller than the error for the fit with the literature values of the refractive indices (black). On the other hand, the values for the 15th harmonic being dominant lie closer to the literature values (cf. fig. 5.12b). These observations are not sufficient to single out one of the two possible solutions.

Although, the determination of refractive indices of harmonics with similar photon energies is difficult, the multicolor imaging can be a promising tool to indirectly measure these unknown optical constants. The experiment could be improved by measuring the HHG spectrum on a shot-to-shot basis, since it became clear that the exact contribution of each harmonic to the signal is of importance. Further, is important to characterize the detection efficiency of the detector well, preferably with light far away from resonances. In addition to that, repeating such an experiment with a single unknown optical constant or the harmonics with unknown optical constants lying further apart would simplify the analysis drastically. This could be accomplished by slightly changing the fundamental wavelength or by using a higher photon energy for the high harmonic generation, which would result in the photon energies of the harmonics being further apart.
The multicolor analysis presented here, is a key requirement for inferring useful information from diffraction patterns obtained with HHG sources. Therefore, such an analysis is

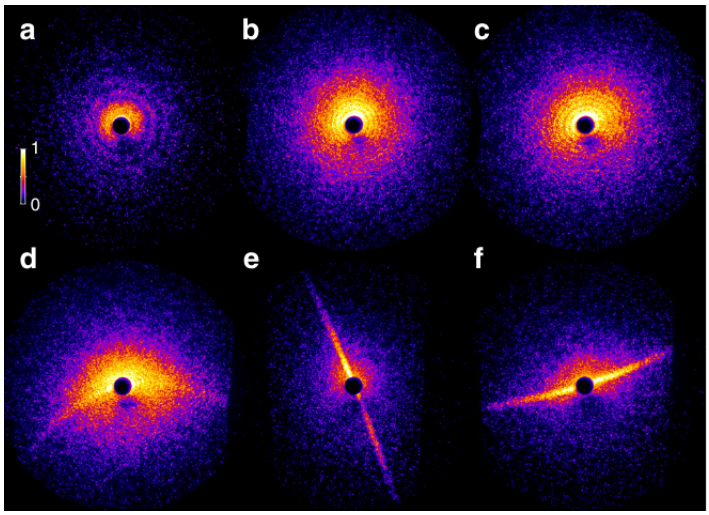

Figure 5.15.: Diffraction patterns from HHG single-shot diffractive imaging experiment (depicted in fig. 5.1). Scattering image from a sphere (a), from ellipsoids (b,c) and from prolate shapes (d-f). Figure from [109].

also necessary for future ultrafast imaging experiments, e. g. for resolving ultrafast plasma dynamics.

So far, the diffraction patterns with spherical fringes have been utilized for extracting optical properties from the data. However, not only spherical droplets were present in the experiment. About 23 % of the diffraction patterns showed elliptical or streaked patterns. In the following section, non-spherical diffraction patterns are evaluated with the forward fit methods MSFT and CSDDA for assigning three-dimensional shapes. This is possible since the XUV radiation of the HHG pulse enables resolution of large scattering angles.

5.4. 3D shape reconstruction via a forward fit

Most diffraction patterns obtained in the experiment exhibit spherical ring structures and therefore result from the scattering of spherical helium droplets, exemplified in fig. 5.15a. However, about 20 % of the patterns show elliptical patterns resulting from the scattering by ellipsoidal helium droplets, depicted in fig. 5.15b-c. Approximately 3 % of the patterns show distinct streak structures, examples shown in fig. 5.15d-f. A previous single-shot diffractive imaging experiment on helium nanodroplets by Gomez *et al.*, performed at LCLS with hard x-ray radiation [48] showed similar scattering images illustrated in fig. 5.16 with spherical (a), elliptical (b) and streaked patterns (c). Comparing the streaked pattern to the HHG streaked patterns fig. 5.15d-f reveals that in the x-ray experiment only straight streaks could be observed, whereas in the HHG experiment mostly bent streaks are present. The reason for this is that at LCLS, hard x-ray radiation with a photon energy of 1.5 keV was used, with this radiation one is restricted to the small an-

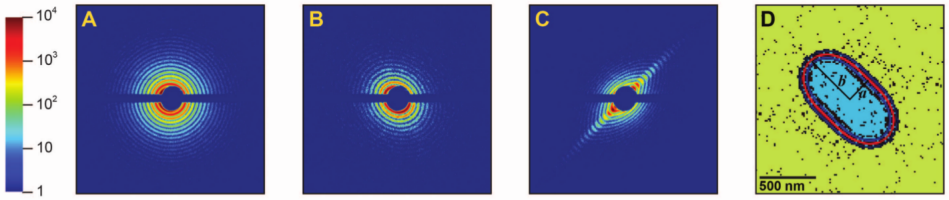

Figure 5.16.: Hard x-ray diffraction patterns of helium nanodroplets from LCLS experiment, spherical (A), elliptical (B) and streaked pattern (C). D shows the 2D projection reconstructed by a phase retrieval algorithm from C. Figure taken from [48].

gle scattering regime in which the diffraction pattern is only dependent on the projected particle density (cf. chps. 3.2 and 2.2.2). Figure 5.16d shows the 2D projected particle density obtained by phase retrieval from fig. 5.16c that was assigned to oblate wheel shaped particles [48]. In helium nanodroplets the transition from spherical or ellipsoidal droplets to prolate particles is suggested to be hindered by vortex arrays that stabilize the oblate shapes [4], which have been observed by Gomez *et al.*. Classically rotating liquid droplets are expected to form prolate particles for high angular momenta [15, 9]. A recent theoretical study predicts prolate shapes even for the superfluid state [3] that also have been observed in [72]. Thus, whether superfluid helium nanodroplets can form prolate and/or oblate shapes is controversial. Therefore, in the following subsection, a prolate particle shape represented by a pill and a oblate particle shape represented by a wheel are compared to each other by computing MSFT diffraction patterns for different orientations. It is investigated whether orientations exist for these particle shapes where bent streaks can be observed. In the second subsection, an experimental diffraction pattern with bent streaks is compared directly to a CSDDA diffraction pattern that includes absorption effects and scattering from all four harmonics.

5.4.1. Scattering from prolate and oblate particles

Certain diffraction patterns characteristic for helium nanodroplets show streaks, straight or bent. However, as previously discussed, whether oblate or prolate shapes are leading to such patterns is controversial. Therefore, in the following, the diffraction patterns from an oblate wheel shaped particle and a prolate pill shaped particle are analyzed for different rotation angles to analyze in which orientation bent streaks can be observed. All diffraction patterns are computed in the wide-angle scattering regime. For small angle scattering bent streaks could not be observed, since the diffraction pattern is only dependent on the projected particle density and always exhibits a point-symmetric structure (cf. chp. 2.2.2). The diffraction patterns are computed with MSFT (cf. chp. 2.2.2). The long axis of both shapes is set to $a = 950\,\text{nm}$, the short axis to $b = 300\,\text{nm}$ and the wavelength to $\lambda = 60.8\,\text{nm}$, absorption is neglected. The density resolution is set to $150 \times 150 \times 150$ and the resolution for the Fourier transforms to 1024×1024. The results are depicted in fig. 5.17. The upper panel shows the diffraction patterns for the

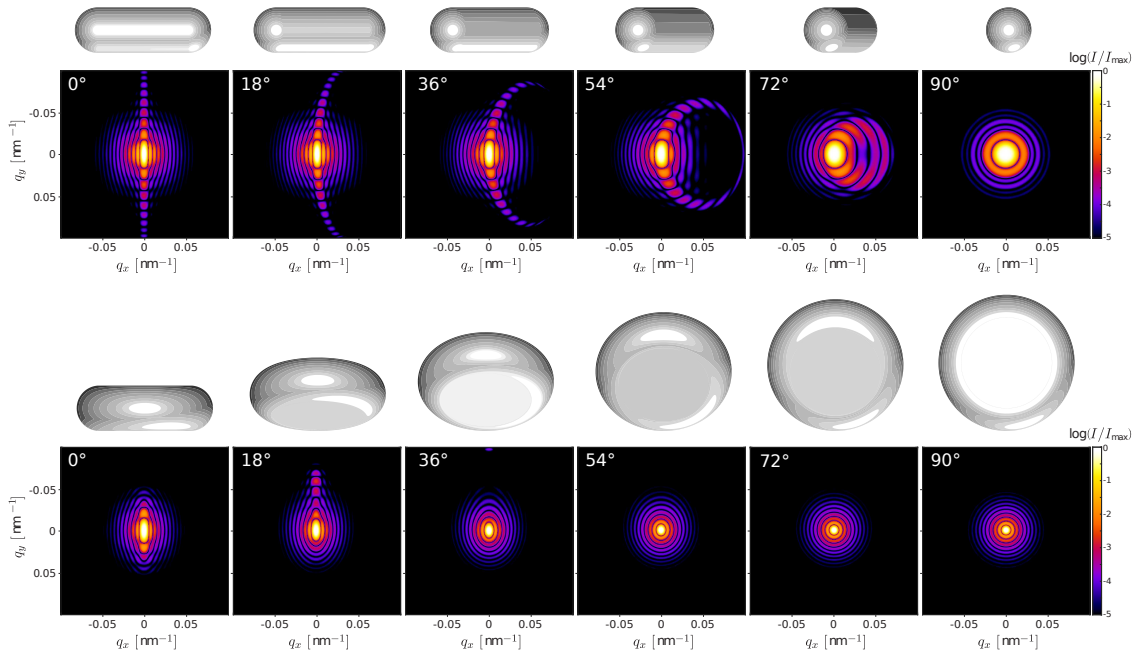

Figure 5.17.: MSFT diffraction patterns for different rotation angles and shapes (upper rows: pill, lower rows: wheel). The long axis is set to 950 nm, the short axis to 300 nm. The density resolution is set to $150 \times 150 \times 150$ and the Fourier transform resolution to 1024×1024, absorption is neglected. The pills are rotated around the y-axis, the wheels around the x-axis, the rotation angles are indicated in the upper left corners of each diffraction pattern and the shape as seen by the laser above each scattering image. Parts of the figure published in [109].

pill, the lower panel for the wheel particle. Above the diffraction patterns the 3D particle is depicted as it is seen by the laser. In the upper left corners the rotation angles are indicated. For 0 ° the projection of both particles is equivalent. Thus, for hard x-ray radiation the diffraction pattern would also be equivalent. Here, both diffraction patterns show straight streaks, however, the pill shaped particle yields longer streaks. Rotating the particles along the laser propagation axis shows that only for a pill shaped particle bent streaks can be observed. The wheel shaped particle does not induce bent streaks for any orientation, even two-sided straight streaks are only observable when hitting the particle directly on the edge. These results indicate, that in the HHG experiment no extremely oblate wheel shaped particles where present. The bent streak patterns can be assigned to prolate pill shaped particles. However, so far, the diffraction patterns were computed utilizing only a single frequency and neglecting absorption. Therefore, the results are verified in the following subsection, by comparing an example diffraction pattern with bent streaks to a CSDDA diffraction pattern from the four harmonics.

5.4.2. Comparison to a high-level simulation

In the previous subsection, the bent-streak structures could be assigned to pill-shaped nanodroplets. However, the MSFT simulations did not include absorption and only a single frequency component of the actual HHG beam was taken into account. In this subsection, therefore, the multiple orders of the HHG beam and absorption are included in the computation to compare to a selected diffraction pattern from the experiment with a bent-streak structure. The high-level simulation is performed utilizing CSDDA (cf. chp. 3.1). To obtain the diffraction pattern of a pill-shaped particle from the HHG laser beam, the patterns from the four different wavelength of the HHG spectrum have to be summed up (cf. eq. (5.1)). For the 11th and 17th harmonic the literature values of the refractive indices are applied ($n_{11} = 0.97 + i0.0$, $n_{17} = 0.9964 + i0.041$), for the 13th and 15th harmonic the average of the refractive indices obtained from the 18 fits is utilized (cf. fig. 5.12a) $n_{13} = 0.9252 + i0.0178$ and $n_{15} = 1.2688 + i0.0417$. CSDDA is performed until the residuum falls below $\Delta = 10^{-2}$. Each diffraction pattern is computed by the scattering of a prolate pill shaped droplet with $n = 6.2 \times 10^5$ dipoles and semi-minor axes $a = b = 370\,\text{nm}$ and the semi-major axis $c = 950\,\text{nm}$, that is rotated about 35 ° between optical axis and the symmetry axis of the particle. Further, the droplet is rotated around the laser propagation direction axis by 80 °. The resulting diffraction patterns from each harmonic are depicted in fig. 5.18a-d, respectively. The particle shape as seen by the laser is depicted in between fig. 5.18a,b,d and e. The diffraction patterns for the 11th and 13th harmonic show a blurring of the fringe structure, whereas the diffraction from the 15th and 17th harmonic show much sharper fringes. The diffraction patterns are summed up, weighted by the intensity ratios $c_{11} = 0.21$, $c_{13} = 0.82$, $c_{15} = 1.0$ and $c_{17} = 0.29$ (cf. fig. 5.2a), displayed in fig. 5.18e. The diffraction pattern shows blurry fringes with a beating structure. Comparing the CSDDA diffraction pattern to the experimental image in fig. 5.18f shows good agreement. The rotated pill shaped particle clearly can reproduce

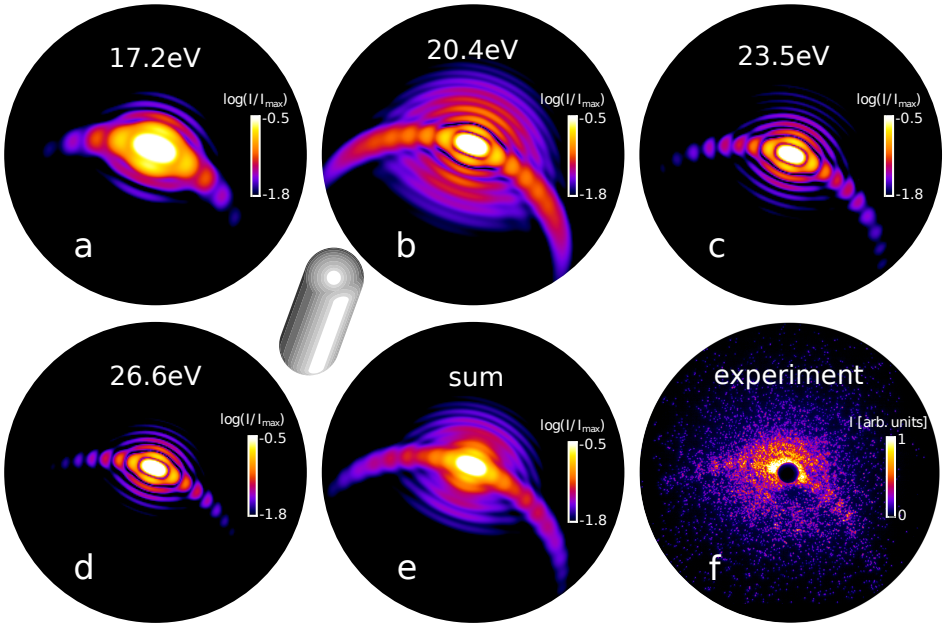

Figure 5.18.: CSDDA diffraction patterns of pill-shaped helium droplet (shape indicated between a,b,d and e) with semi-minor axes $a = b = 370\,\text{nm}$ and semi-major axis $c = 950\,\text{nm}$, that is rotated about $35\,^\circ$ between optical axis and the symmetry axis of the particle. Further, the droplet is rotated around the laser propagation direction axis by $80\,^\circ$. The pill is computed with $n = 6.2 \times 10^5$ dipoles and the residuum is set to $\Delta = 10^{-2}$. a) Diffraction pattern corresponding to 11th harmonic with $n_{11} = 0.97 + i0.0$. b) 13th harmonic with average of the refractive indices obtained from the 18 fits is utilized (cf. fig. 5.12a) $n_{13} = 0.9252 + i0.0178$ c) 15th harmonic with $n_{15} = 1.2688 + i0.0417$ and d) 17th harmonic with $n_{17} = 0.9964 + i0.041$. e) shows the sum of a-d with intensity ratios set to $c_{11} = 0.21$, $c_{13} = 0.82$, $c_{15} = 1.0$ and $c_{17} = 0.29$ according to the HHG spectrum (fig. 5.2a). f) shows an experimental HHG single-shot diffraction pattern. Parts of the figure published in [109].

the experimental diffraction pattern and verifies that the helium droplets can exhibit prolate shapes. Two possible explanations for this behavior exist. (i) The occurrence of prolate shapes is expected for classically rotating droplets, meaning the helium droplets in the experiment are not superfluid. (ii) The prolate shapes are stable in the superfluid state. This explanation would be confirmed by a recent theoretical study, suggesting the existence of prolate shapes even in the superfluid state [3]. This study and the observation of classically stable liquid rotating helium droplets in this experiment gives rise to future experiments investigating the existence of prolate droplets showing macroscopic shape rotation in the superfluid state. First experimental results showing the shape evolution of rotating superfluid helium nanodroplets can be found in [72].

6. Three-dimensional chracterization of free nanostructures via two-color single-shot diffractive imaging

Reconstruction of the two-dimensional projected electron density of a target from small angle x-ray diffraction patterns via phase retrieval schemes is well established (see chp. 1.2.1) and one of the commonly employed algorithms can be found in the app. D. Two-dimensional phase retrieval algorithms rely on the central assumption that the diffraction pattern of a particle is proportional to the modulus squared Fourier amplitude of the projected particle density. The generalization of the phase retrieval to higher dimensions is straightforward. Therefore, to gain a three-dimensional particle density, the Fourier amplitude of the object needs to be three-dimensional as well. The Fourier slice theorem states that a slice with a certain orientation in the 3D Fourier space representation of a 3D particle shape is equivalent to the 2D Fourier transform of the particle density projected onto the same plane. Thus, to recover the 3D Fourier amplitude distribution of a single nanoobject, multiple diffraction patterns of reproducible randomly oriented targets can be assembled according to the respective particle orientations. However, two restrictions for the applicability of phase retrieval algorithms exist. They are only applicable to the direct reconstruction of density projections (or 3D densities) in the limit of the first Born approximation and for small angle scattering. The first restriction is equivalent to the requirement that refraction and absorption are negligible. The second restriction results from the requirement that the momentum transfer must be perpendicular to the incoming beam. The laser wavelength in the single-shot diffraction experiment is therefore usually small (see also chps. 2.2.2 and 3.2). In this case, information about the target orientation cannot be inferred from the diffraction pattern unambiguously. Nevertheless, different procedures for orientation retrieval exist, but typically include expensive statistical analysis. They have been outlined in chp. 1.2.1.

In this chapter, a two-color imaging experiment that aims to simplify orientation retrieval is introduced. The key idea is that two simultaneously recorded diffraction patterns in the small angle and wide angle scattering regime can highly increase the information content of the single-shot diffractive imaging data. The small angle diffraction pattern obtained with hard x-ray radiation yields the data for 3D reconstruction via phase retrieval, the wide angle diffraction pattern with soft x-ray or extreme ultraviolet (XUV) radiation can be used to mitigate the orientation problem. Such a scenario could be realized at seeded free electron lasers such as FERMI in a high gain harmonic generation (HGHG) cascade [2]. A possible setup is depicted in fig. 6.1. A two-color laser beam is utilized to image a

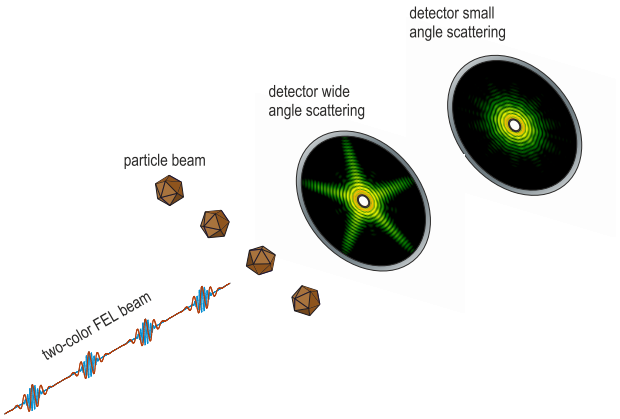

Figure 6.1.: Draft of setup for a two-color single-shot diffractive imaging experiment. A high-intensity two-color laser pulse hits a particle beam and two diffraction patterns are obtained simultaneously on a wide angle and a small angle scattering detector.

nanotarget, i. e. in each shot two diffraction patterns are recorded.

The proposed two-color 3D phase retrieval reconstruction scheme contains three basic steps. (i) First, the particle orientation problem is solved by employing the characteristics of the wide angle diffraction pattern. Therefore, a database of wide angle diffraction patterns with known particle orientations is pre-calculated. By comparison of wide angle scattering images with unknown orientation to the database, the particle orientation can be assigned to the wide angle image and, as both images are recorded simultaneously, also for the corresponding small angle image. This step is referred to as orientation tagging. (ii) Second, the orientation tagged small angle diffraction patterns are assembled according to their corresponding particle orientations to access the Fourier volume. (iii) In the third step, this 3D Fourier amplitude is utilized for the 3D reconstruction of the particle via phase retrieval. In the following, the first two steps are discussed in more detail. Therefore, first, a procedure to find the orientation of a diffraction pattern with unknown particle orientation is introduced. To this end, the diffraction pattern is compared to a database containing diffraction patterns with known particle orientations. Second, an estimation of the the number of randomly oriented diffraction patterns required for covering the complete 3D Fourier space is given. Last, the orientation tagging approach is tested for two model shapes, an asymmetric tripod and a highly symmetric icosahedron, by verifying its success by performing a 3D phase retrieval. The applied phase retrieval algorithm is outlined in app. D.

6.1. Orientation tagging

A necessary precondition for utilizing the two-color imaging approach is knowledge about the outer shape of the target. This allows for the computation of a database of wide

angle scattering images with known particle orientations for the soft x-ray or XUV laser wavelength. In the ideal case, also this rough outer shape should be extracted from the data, but for clarity it is assumed that the outer shape may already be known. The particle orientation is described by three Euler angles, in which the object is rotated around the z-axis by the angle α, around the x-axis by β and finally rotated around the rotated z'-axis by γ, depicted in fig. 6.2. Only for $\beta = \pm\pi$ the Euler angles are not unique. As shown in [26] the angles α and γ need to be sampled from 0 to 2π and $\cos(\beta)$ from -1 to 1 to cover all possible orientations. Note that for particles with symmetry axes a certain orientation can be achieved by multiple sets of Euler angles. The scattered electric field intensity is computed with the multislice Fourier transform method (MSFT, see sec. 2.2.2). To retrieve the particle orientation, the wide angle diffraction patterns I_{exp} with unknown particle orientation are compared to the database $I_{\mathrm{db}}(\alpha, \beta, \gamma)$. For each diffraction pattern the following error ϵ is computed via

$$\epsilon(\alpha, \beta, \gamma) = \sum \left(\log_{10} I_{\mathrm{db}}(\alpha, \beta, \gamma) - \log_{10} I_{\mathrm{exp}}\right)^2 . \tag{6.1}$$

Note that I_{exp} refers to the numerical experiment here. The orientation yielding the minimal error is assigned to the soft x-ray diffraction pattern and its respective hard x-ray diffraction pattern. The major goal of the comparison to the database is to get close enough to the correct solution for the orientation. Afterwards, the Euler angles are refined further by applying a simplex algorithm [90] (cf. sec. 5.3). To this end, the starting point for the simplex fit are the three retrieved Euler angles from the comparison. An updated set of Euler angles is computed by minimizing the error (similar to eq. (6.1))

$$\epsilon(\alpha, \beta, \gamma) = \sum \left(\log_{10} I_{\mathrm{comp}}(\alpha, \beta, \gamma) - \log_{10} I_{\mathrm{exp}}\right)^2 . \tag{6.2}$$

via the simplex scheme, the diffraction patterns (I_{comp}) for the current sets of Euler angles are computed via MSFT in each simplex iteration.

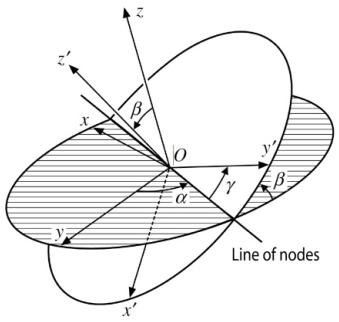

Figure 6.2.: Particle rotation in 3D described by Euler angles α, β and γ, where the object first is rotated around the z-axis around α, then around the y-axis by β and last around the rotated z-axis z' by γ. Figure taken from [87].

After the orientation tagging is performed, the small angle diffraction patterns can be assembled according to the corresponding particle orientations to obtain the 3D Fourier volume. However, to recover the complete 3D Fourier data, each voxel needs to be covered at least by one pixel of the small angle diffraction patterns. Therefore, in the following section, an estimation of how many diffraction patterns are needed to cover the complete 3D Fourier space is given.

6.2. 3D diffraction pattern

By assembling diffraction patterns according to their corresponding particle orientations the squared modulus of the 3D Fourier transform can be obtained. In that process, it is important that each voxel of that 3D Fourier volume is covered by at least one pixel of the diffraction patterns. The probability p that all pixels are covered by at least one diffraction pattern can be calculated via [34]

$$p = \left(1 - (1 - k/K)^N\right)^K, \tag{6.3}$$

with the number of diffraction patterns N, $K = 2\pi(D/d - 1/2)^2$ and $k = \pi(D/d - 1/2)$ with the particle diameter D and the resolution d. Figure 6.3 illustrates this relation. It shows the number of randomly oriented diffraction patterns N required for covering the complete Fourier volume with a probability of 99% in dependence on particle resolution and particle diameters. It becomes evident that for larger particles and for a better resolution the number of required diffraction patterns increases. Thus, for a given particle size the achievable resolution for the particle reconstruction highly depends on the number of diffraction patterns that can be recorded and orientation tagged for a randomly oriented reproducible target. Note that the achievable half-period resolution additionally is limited by the largest scattering angle that can be resolved and the utilized wavelength.

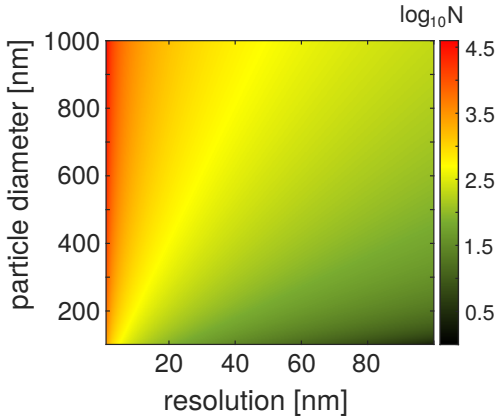

Figure 6.3.: Number of diffraction patterns N of randomly oriented particles to reach a probability of $p = 0.99$ (eq. (6.3)) that all pixels of the 3D Fourier volume are covered for different resolutions and particle diameters.

In the following section, the orientation tagging and the resulting two-color phase retrieval scheme is tested for two sample shapes, an asymmetric tripod and a symmetric icosahedron. To this end, for both shapes, first, the required database resolution is evaluated, then the orientation tagging is performed and last is tested by performing the 3D phase retrieval.

6.3. Test cases

First, the ideal case of an asymmetric shape is investigated, where a certain diffraction pattern only can be achieved with a single orientation, i. e. one set of Euler angles. Second, a symmetric target is analyzed, an icosahedron, chosen to represent a realistic target

motivated by the pseudo-icosahedral shape of a mimivirus. For both test cases, the same simulation parameters are utilized. The values for the laser wavelength are chosen such that they could be achieved at the FEL FERMI. For the wide angle scattering it is set to $\lambda_{\text{waxs}} = 21\,\text{nm}$ ($\hat{=}\ 59\,\text{eV}$) and the wavelength for small angle scattering to $\lambda_{\text{saxs}} = 4\,\text{nm}$ ($\hat{=}\ 310\,\text{eV}$). In a realistic scenario, absorption is expected to have a large impact for small photon energies. Therefore, the absorption length is set equal to $l_{\text{abs}} = 10\,\text{nm}$ for λ_{waxs}, for λ_{saxs} absorption is neglected. All diffraction patterns are computed with MSFT with the Fourier transforms having the dimension 64×64.

Before the orientation tagging step can be performed, for both test shapes a sufficient database resolution needs to be found. Therefore, the error (eq. (6.1) for a single diffraction pattern is characterized. Afterwards, the orientation tagging is performed and the diffraction patterns are assembled to the 3D Fourier volume, the phase retrieval scheme is applied for reconstruction of the 3D particle density. The utilized phase retrieval output-output algorithm is outlined in app. D. Convergence was reached fastest for the β parameter set to 0.9. The starting Fourier phase is chosen randomly. Further, for the phase retrieval algorithm to converge efficiently a suitable mask has to be chosen. A convenient choice is a shrinkwrap mask that is adapted in each iteration [79]. This can be done by convolution of the density map with a Gaussian with a certain width, resulting into a smoothed density. The mask is then set to unity at all pixels where the convoluted normalized density is above a certain threshold and set to zero where it is below that threshold. The threshold is set to $\tau = 0.2$ and the Gaussian width is varied every 100 iterations between $b = 5, 7, 9, 11$ pixels. These values were found to lead to a fast convergence for the considered scenario.

6.3.1. Asymmetric shape: tripod

The two-color 3D phase retrieval scheme is first tested for an asymmetric shape without any symmetry axes. A convenient choice for this is a tripod sketched in fig. 6.4a. The legs of the tripod are set to $a = 600\,\text{nm}$ along x, $b = 450\,\text{nm}$ along y and $c = 510\,\text{nm}$ along z. The width of each leg is equal and is set to $d = 300\,\text{nm}$. Inside the leg along the x-axis a spherical void represents the inner structure with radius $R = 100\,\text{nm}$, the isosurface of the object is shown in fig. 6.4b. The resolution of the homogeneous density for the wide angle diffraction patterns is set to 30 nm, for the small angle diffraction patterns to 14.1 nm.

Database resolution

To correctly estimate the particle orientation from comparison to the diffraction patterns in the database, the database needs to cover the possible Euler angles with a sufficient resolution. To estimate this resolution, first the error (eq. (6.1)) for a single diffraction pattern is characterized for different database resolutions. Therefore, one diffraction pattern of the tripod with spherical void in the orientation configuration $\alpha_{\text{test}} = 44\,^\circ$,

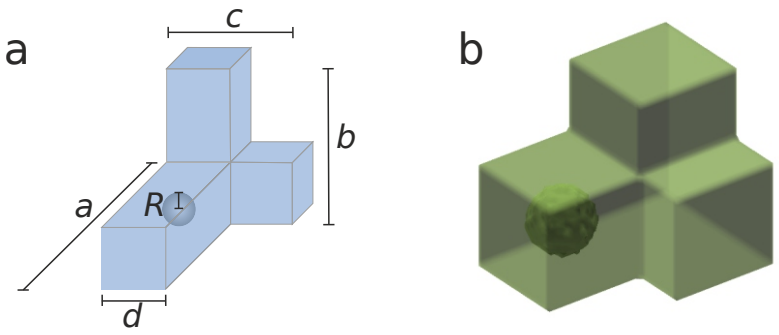

Figure 6.4.: a) Sketch of asymmetric model shape, a tripod. b) Isosurface of the object. The legs of the tripod are set to $a = 600\,\text{nm}$, $b = 510\,\text{nm}$ and $c = 450\,\text{nm}$. The width of each leg is equal and is set to $d = 300\,\text{nm}$. Inside the leg along the a-leg a spherical void with $R = 100\,\text{nm}$ is inserted by setting the density there equal to zero.

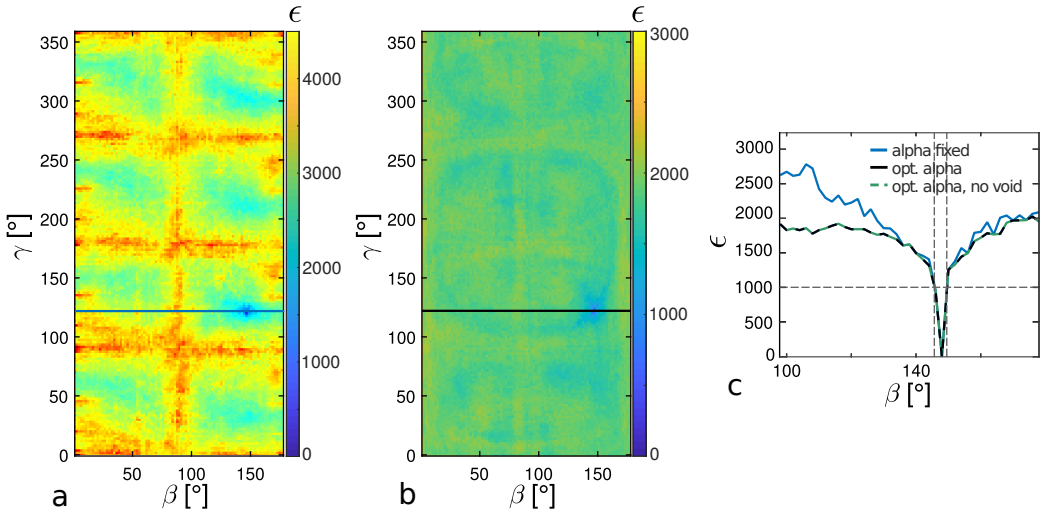

Figure 6.5.: Error ϵ in dependence of Euler angles β and γ for a single diffraction pattern with void $R = 100\,\text{nm}$ with rotation angles $\alpha_{\text{test}} = 44\,°$, $\beta_{\text{test}} = 148\,°$ and $\gamma_{\text{test}} = 122\,°$. Each diffraction pattern is computed with MSFT with $\lambda_{\text{waxs}} = 21\,\text{nm}$ and $l_{\text{abs}} = 10\,\text{nm}$, the tripod legs dimensions are $a = 600\,\text{nm}$ along x, $b = 450\,\text{nm}$ along y and $c = 510\,\text{nm}$ along z and a width of each leg of $d = 300\,\text{nm}$. Comparison diffraction patterns are computed without spherical void. Further details on the MSFT simulation can be found in the text. a) shows error map for $\alpha = \alpha_{\text{test}}$ b) shows error map for α corresponding to minimal error and c) Cuts through a, b at $\gamma = \gamma_{\text{test}}$, indicated by solid lines in a and b, respectively. Blue solid line shows error for $\alpha = \alpha_{\text{test}}$ (corresponding to a), the black solid line shows minimal error corresponding for optimal α (corresponding to b). The green dashed line shows the error for the same case, where the asymmetric shape does not have a spherical void, but has the exact same structure as for the computation of the database diffraction patterns.

$\beta_{\text{test}} = 148\,^\circ$ and $\gamma_{\text{test}} = 122\,^\circ$ is computed. The error ϵ via eq. (6.1) of this diffraction pattern is computed by comparison to a database with α set to α_{test} and β sampled from 0 to $180\,^\circ$ and γ sampled from 0 to $360\,^\circ$ in $2\,^\circ$ steps. Diffraction patterns for the database are computed without inner structure. The resulting error map is depicted in fig. 6.5a, which reveals eight valleys including one containing the single global minimum at $\beta = 148\,^\circ$ and $\gamma = 122\,^\circ$. The error map for the same parameters, but with optimal α for each β-γ combination (fig. 6.5b) shows the same structure, with a distinct deep global minimum. Still, local quite shallow minima exist. Nonetheless, the error map verifies that diffraction patterns are unique for a single orientation. Figure. 6.5c shows cuts through the global minimum of fig. 6.5a and b, indicated by the solid lines. For both cases (fixed α and optimal α), the minimum has the same width. Further, the error for the sample configuration is computed for a diffraction pattern obtained without inner structure and plotted as dashed green line. It can be seen that the error is equivalent to the error for the tripod including the inner structure. Hence, the inner structure does not have a severe effect on the orientation tagging for the considered example. The inner structure of the target is hidden for the soft x-ray or XUV wavelength because of two reasons, first, the longer wavelength leads to lower resolution, since only length scales on the order of the wavelength can be resolved and second the higher absorption in this wavelength regime prevents the light to completely penetrate the target. To find the global minimum, the database has to be sampled with a resolution smaller than the width of the global minimum. The plot reveals a width of the minimum of $3\,^\circ$ at an error of 1000. Therefore, a $2\,^\circ$ resolution of the database is sufficient to find the correct orientation of a randomly oriented target. To verify this, the orientation tagging is performed for 500 diffraction patterns with random orientations for a database resolution of $8\,^\circ$ and $2\,^\circ$. The retrieved Euler angles are refined by performing 100 simplex steps. The respective retrieved angles versus the correct orientation angles are depicted in fig. 6.6a and b. For correct orientation retrieval all angles should lie on the diagonals. For the $8\,^\circ$ sampling this is not the case, e. g. for α lines parallel to the diagonals appear, representing points where a local minimum has been found. The mean deviation between correct and retrieved Euler angles can be computed via

$$\Delta = \sqrt{(\alpha_{\text{corr}} - \alpha_{\text{ret}})^2 + (\beta_{\text{corr}} - \beta_{\text{ret}})^2 + (\gamma_{\text{corr}} - \gamma_{\text{ret}})^2}. \tag{6.4}$$

For the $8\,^\circ$ sampling, it is $\Delta = 22.9\,^\circ$. For the $2\,^\circ$ sampling all angles lie very close the diagonals, the mean deviation to the correct Euler angles is $\Delta = 3\,^\circ$. In conclusion, the $8\,^\circ$ sampling is not sufficient for correct orientation tagging. Thus, the $2\,^\circ$ sampling is utilized in the following, resulting in a database containing 2.9 million diffraction patterns.

3D phase retrieval

Since all small angle scattering images are computed with a resolution of 64×64, the 3D Fourier volume dimensions are $64 \times 64 \times 64$. This corresponds to a spatial resolution of 14.1 nm for the retrieved particle density. To cover all pixels of the 3D Fourier space with

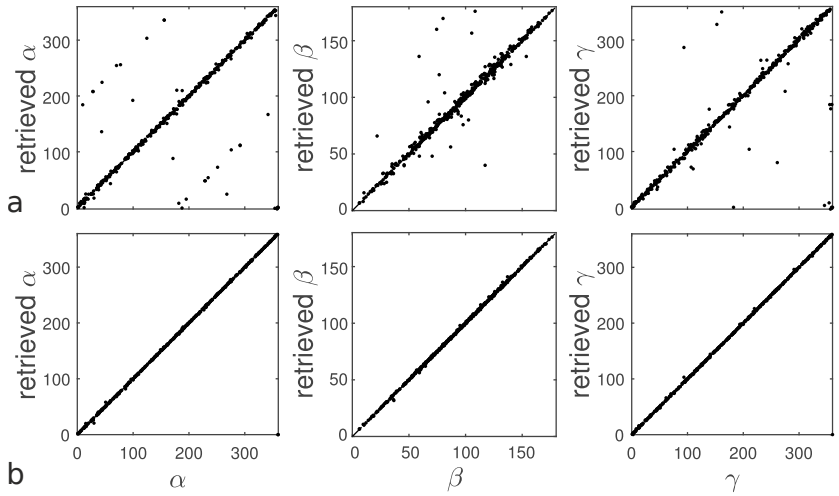

Figure 6.6.: Euler angles retrieved by comparison to a database for 500 diffraction patterns of tripod (fig. 6.4) with random orientations. Each database diffraction pattern is computed with MSFT with $\lambda_{\mathrm{waxs}} = 21\,\mathrm{nm}$ and $l_{\mathrm{abs}} = 10\,\mathrm{nm}$, the tripod with $a = 600\,\mathrm{nm}$ along x, $b = 450\,\mathrm{nm}$ along y and $c = 510\,\mathrm{nm}$ along z and a width of each leg of $d = 300\,\mathrm{nm}$. Additional details on the MSFT simulation can be found in the text. The three Euler angles are sampled evenly, α and γ from 0 to 360 ° and β from 0 to 180 °. a) shows the retrieved versus actual Euler angles for a database with 8 ° sampling, and b) for a database with 2 ° sampling.

a probability of 100% 3000 sets of wide angle and small angle diffraction patterns with random orientations are computed. The orientation tagging is performed by comparing the wide angle diffraction patterns to the 2 ° sampled database. Again, 100 simplex iterations are performed to refine the retrieved orientation angles.
After the orientation tagging step, the small angle diffraction patterns are assembled to the Fourier volume in accordance to their respective orientation angles. The output-output algorithm with a shrinkwrap mask is applied to retrieve the target shape. The resulting isosurface of the retrieved 3D density is depicted in fig. 6.7a. It can be seen that compared to the input object (cf. 6.4b) the edges are less sharp and the surface is not as even. However, the overall shape including the spherical void could be retrieved correctly. A slice through the density at $z = 0$ is shown in fig. 6.7b and confirms this. The white dashed lines show the edges of the slice through the input 3D density. Not only the shape but also the size of void and object could be recovered correctly. The particle density should be homogeneous, however, shows some inhomogeneities in the reconstruction.

6.3.2. Symmetric shape: icosahedron

As shown above, for an asymmetric object with no symmetry axes, one set of orientation angles delivers a unique diffraction pattern. Therefore, by comparison to a database it is quite simple to retrieve the correct orientation angle. For a symmetric shape it gets a bit more complicated. This is tested in this section exemplified by an icosahedral shape, which is a regular faceted shape, motivated by the structure of a mimivirus. The icosahedron is

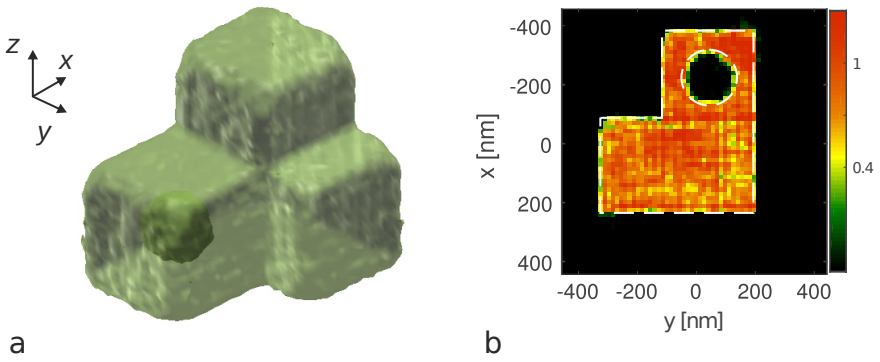

Figure 6.7.: Resulting particle density of 3D phase retrieval (output-output scheme) from 3000 orientation tagged, assembled small angle diffraction patterns. Further information on the phase retrieval scheme is outlined in the text. The MSFT diffraction patterns from a tripod with legs $a = 600\,\text{nm}$, $b = 450\,\text{nm}$ and $c = 510\,\text{nm}$, a width of each leg of $d = 300\,\text{nm}$ and s spherical void with radius $R = 100\,\text{nm}$ are computed with $\lambda_{\text{saxs}} = 4\,\text{nm}$ and $l_{\text{abs}} = 10\,\text{nm}$. Additional details on the MSFT simulation can be found in the text. a) shows the isosurface of retrieved object and b) slice through the retrieved density at x-y-plane at $z = 0$. White dashed line shows the edges of the input tripod.

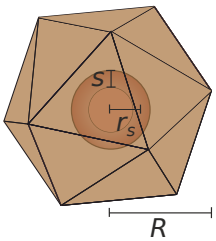

Figure 6.8.: Model shape. Icosahedron with outer radius $R = 300\,\text{nm}$ and inner spherical shell with zero density with radius of $r_s = 80\,\text{nm}$ and a shell thickness of $s = 30\,\text{nm}$.

a symmetric structure with 31 symmetry axes, meaning that a certain diffraction pattern can be imaged with different sets of orientation angles. There exist ten three-fold axes through the centers of opposite faces, six five-fold axes through opposite vertices and fifteen two-fold axes through the midpoints of two opposite edges.

To test the two-color 3D phase retrieval scheme, the icosahedron is constructed with a simple inner structure, a spherical shell inside, depicted in fig. 6.8. As a model system, the outer radius of the icosahedron is set to $R = 300\,\text{nm}$, the shell inside to $r_s = 80\,\text{nm}$ with a thickness of $s = 30\,\text{nm}$, where the density is set to zero. The resolution of the density for the wide angle diffraction patterns is set to 24.2 nm, for the small angle diffraction patterns to 11.5 nm.

Database resolution

For computation of the orientation tagging database, diffraction patterns are computed with the XUV wavelength of the icosahedron without inner structure with a particle resolution of 20 nm. As in the previous section, to estimate the necessary size of the database the error map for a single diffraction pattern in a certain orientation is characterized. Therefore the icosahedron with shell is rotated by $\alpha_{\text{test}} = 24°$, $\beta_{\text{test}} = 64°$ and $\gamma_{\text{test}} = 50°$. The resulting MSFT diffraction pattern is compared to a database with a 4 ° sampling for different β and γ, and α set to α_{test} where the error again is computed via eq. (6.1). The resulting error map is depicted in fig. 6.9. The error map reveals the fivefold symmetry of the icosahedron, since the pattern repeats itself every 72° in γ. Hence, it is sufficient to sample the angle γ only from 0 to 72°.
This area is further characterized by computing the error for the test pattern for all orientation angles in 1° steps. Figures 6.10a and b show the error map in dependence on β and γ and β and α, respectively, where the third angle for each pair is set to the optimal value. It becomes clear that for both error maps a large number of local minima emerges, which all belong to equivalent orientation angles of the icosahedron due to the existence of the symmetry axes. Further, two observations can be made. First, fig. 6.10b shows a symmetric pattern, hence, as for the rotation of the angle γ it is sufficient to only compute α in the range from 0 to 180 °. Second, the majority of the local minima show a circular structure, however, in fig. 6.10a along the γ-axis around $\beta = 10\,°$ and $\beta = 170\,°$ the minima are stretched over a range of about 40 °. The same structure can be seen along the β axis in fig. 6.10b. This complicates the orientation tagging, since for a too coarse sampling it is possible to end up with a local minimum that does not belong to the correct or equivalent orientation of the icosahedron. The cuts (indicated as lines solid and dashed gray and black lines in fig. 6.10a and b, depicted in fig. 6.10c, reveal a width of about 0.6 ° of the minima at an error of 200. The error that has to be resolved needs to be that small so the global minima can be distinguished from the deep local minima. Therefore, the orientation angles of the database are sampled in 0.5° steps. This sampling

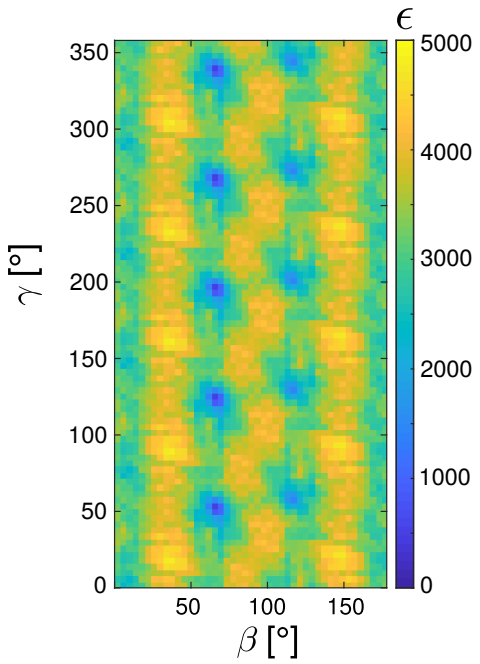

Figure 6.9.: Error ϵ for different β and γ for a single MSFT diffraction pattern of an $R = 300\,\text{nm}$ icosahedron with a spherical shell void with $r_s = 80\,\text{nm}$, rotated by $\alpha_{\text{test}} = 24°$, $\beta_{\text{test}} = 64°$ and $\gamma_{\text{test}} = 50°$ with rotation angle α fixed to the α_{test}. MSFT diffraction patterns computed with $\lambda_{\text{waxs}} = 21\,\text{nm}$ and $l_{\text{abs}} = 10\,\text{nm}$. Diffraction patterns for comparison (database) to test pattern are computed without void inside. Additional information on the MSFT simulations can be found in the text.

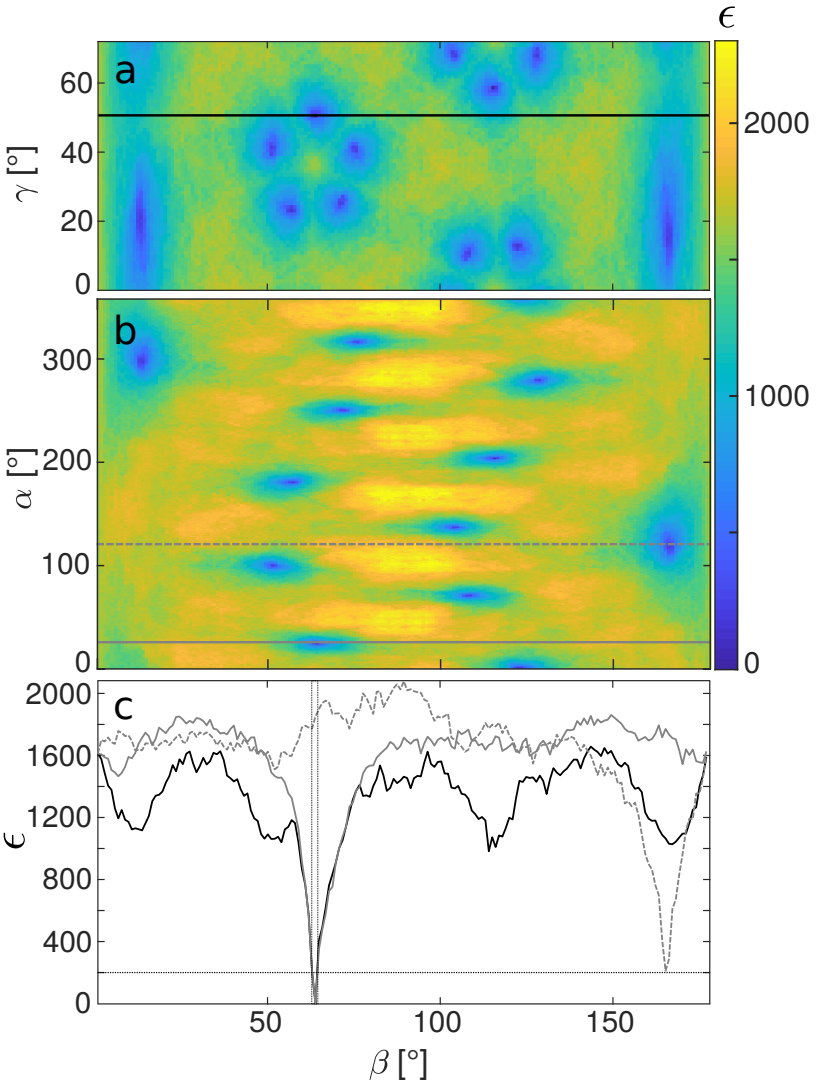

Figure 6.10.: Error ϵ in dependence of Euler angels β and γ for a single diffraction pattern of an icosahedron with $R = 300\,\text{nm}$ and $r_s = 80\,\text{nm}$ oriented with $\alpha_{\text{test}} = 24\,°$, $\beta_{\text{test}} = 64\,°$ and $\gamma_{\text{test}} = 50\,°$. The MSFT diffraction patterns are computed with $\lambda_{\text{waxs}} = 21\,\text{nm}$ and $l_{\text{abs}} = 10\,\text{nm}$, the comparison (database) diffraction patterns are computed without void. Further details on the MSFT simulation can be found in the text. a) shows the error map for β versus γ (with α corresponding to minimal error for each β-γ combination). b) shows the error map for β versus α (with optimal γ). c) depicts cuts indicated by the solid and dashed lines in a and b. The minima at $\beta = 64\,°$ has a width of $0.6\,°$ for $\epsilon = 200$.

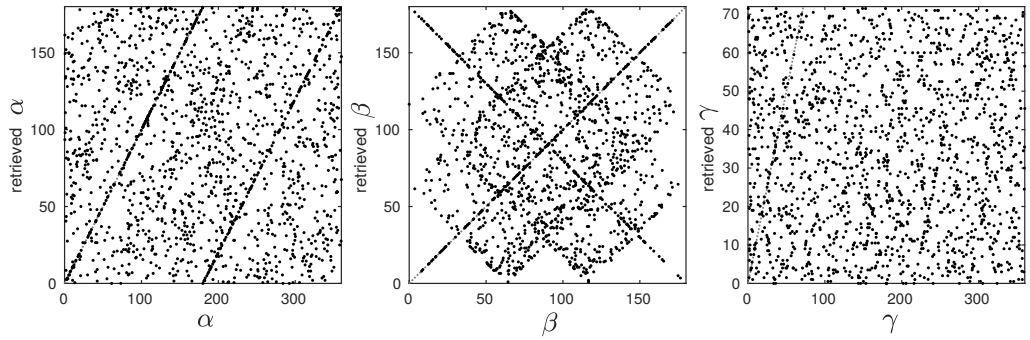

Figure 6.11.: Retrieved Euler angles versus actual Euler angles for 1600 MSFT diffraction patterns of a $R = 300\,\text{nm}$ icosahedron with spherical shell void with $r_s = 80\,\text{nm}$, computed with $\lambda_{\text{waxs}} = 21\,\text{nm}$ and $l_{\text{abs}} = 10\,\text{nm}$. The Euler angles are retrieved by comparison to a database computed without spherical void. Additional details on the MSFT simulation can be found in the text. The Euler angles for computation of the database are sampled in α and β from 0 to 180 ° and γ from 0 to 72 ° in 0.5 ° steps. The dashed grey lines indicate the diagonals where retrieved Euler angle equals actual Euler angle.

results in a database containing 18.7 million diffraction patterns, which corresponds to 300 GB of disk space for single precision.

3D phase retrieval

All scattering images are computed with a resolution of 64×64, hence, the 3D Fourier volume has the dimensions $64 \times 64 \times 64$, resulting in a spatial resolution of 11.5 nm for the retrieved target shape. To cover all voxels of the 3D Fourier space with a possibility greater than 99% 1600 diffraction patterns of hard and soft x-ray radiation with random orientations with the respective dimensions are computed. These sets of scattering images then are orientation tagged by comparing each wide angle diffraction pattern to the database.
The resulting retrieved orientation angles in dependence on real orientation angles are depicted in fig. 6.11. Again, it shows that no unique diffraction pattern exists for one set of Euler angles, since not all real and retrieved angles lie on the diagonal indicated by the solid black line in each of the three plots. For the α and β angle symmetric structures are visible emerging from the symmetry axes of the icosahedron.
The orientation tagged small angle diffraction patterns are interpolated onto the 3D Fourier volume and the phase retrieval scheme is performed as described at the beginning of the section. The results are depicted in fig. 6.12. Figure 6.12a shows the isosurface of the retrieved icosahedron. The outer shape of the icosahedron could be retrieved correctly. Also a spherical shape inside the icosahedron is visible, however, a structure beside it can be observed. Figures 6.12b-c shows cuts through the retrieved density for $x = 0$, $y = 0$ and $z = 0$, respectively. The images reveal that the outer shape and spherical shell show the expected size and shape. However, the density is not equal everywhere, but shows an inhomogeneity as in the reconstruction of the tripod, however, more severe. The phase retrieval result can be improved by performing the phase retrieval multiple times with

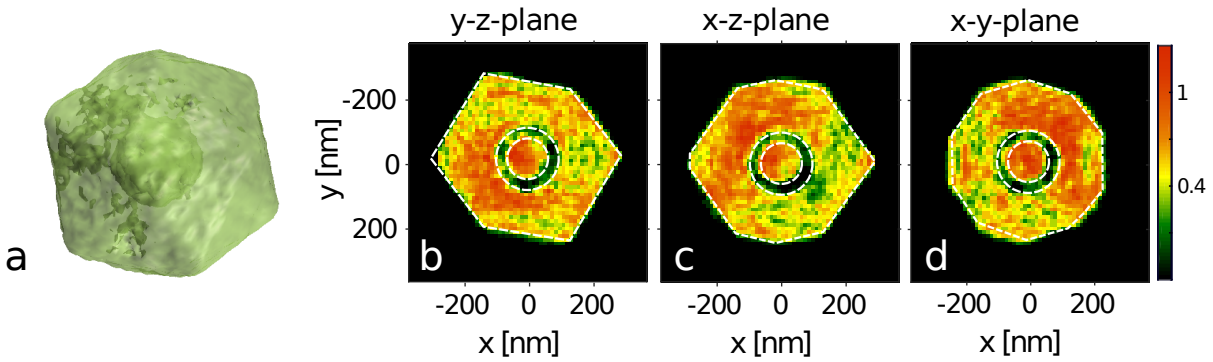

Figure 6.12.: Retrieved particle shape and density, obtained with output-output phase retrieval algorithm. Details on the algorithm are outlined in the text. The 3D Fourier volume is obtained by assembling 1600 orientation tagged small angle diffraction patterns. Orientation tagging is performed by comparison of corresponding wide angle diffraction patterns to a database with 0.5 ° sampling. The diffraction patterns are computed with MSFT, simulation parameters can be found in the text. a) shows the isosurface of retrieved object and b)-c) slices through the particle density, the planes are indicated in the title of each plot. The white dashed lines show the edges of the density for the input icosahedron.

different random Fourier phases as starting parameter. The averaged particle density of 100 retrieved densities is shown in fig. 6.13. It can bee seen that the isosurface of the density in fig. 6.13a clearly reflects the shape of the icosahedron and the shell inside. No unexpected structures are present. The cuts through the density, depicted in figs. 6.13c-d shows no unevenness anymore. The size and shape of the icosahedron is reproduced well. However, the density is not zero inside the shell, but a bit larger.

In summary, the two-color phase retrieval scheme could successfully be shown on artificial data. Hence, the imaging of nanotargets simultaneously with two different wavelength is a promising route to perform the orientation tagging step by comparison to a database and then be able to retrieve the three-dimensional target shape. A drawback of the approach is the necessity of knowledge about the outer shape of the target.

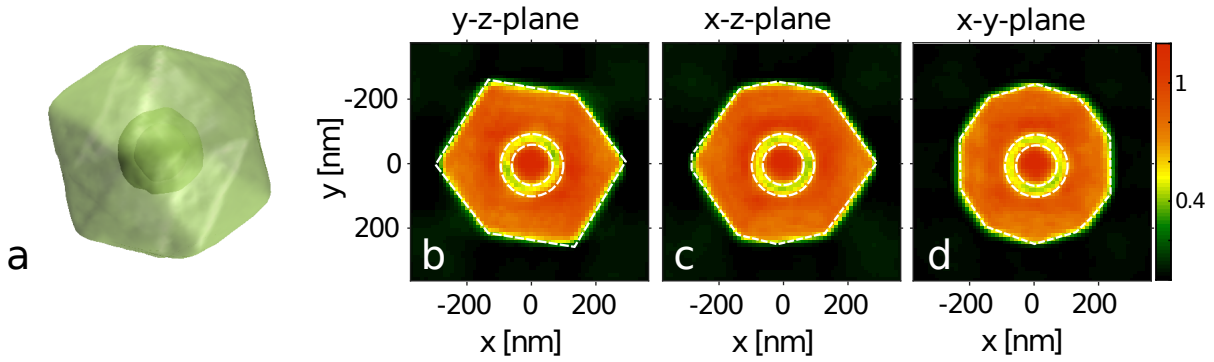

Figure 6.13.: Particle shape and density averaged over 100 retrieved densities, each obtained with output-output phase retrieval algorithm with different random phase as starting parameter. Details on the algorithm are outlined in the text. The 3D Fourier volume is obtained by assembling 1600 orientation tagged small angle diffraction patterns. The orientation tagging is performed by comparison of the corresponding wide angle diffraction patterns to a database with 0.5 ° sampling. The diffraction patterns are computed with MSFT, simulation parameters can be found in the text. a) shows the isosurface of retrieved object and b)-c) slices through the particle density, the planes are indicated in the title of each plot. The white dashed lines show the edges of the density of the input icosahedron.

7. Summary and Outlook

The goal of this work was the development, characterization and application of reconstruction methods for the structure determination of free nanoparticles with single-shot diffractive imaging. Conceptually different reconstruction methods were implemented and utilized in the theoretical analysis and on experimental data to infer information about the target and for the investigation of different laser parameters on the diffraction pattern.

The second chapter was dedicated to deriving the basic principles of scattering theory in linear response relevant for the work presented in this thesis. It became clear, that the utilized wavelength not only influences the obtainable resolution in a scattering experiment, but impacts the applicable reconstruction model. Short wavelength radiation in the hard x-ray regime leads to a restriction to small scattering angles. It was shown that in this case, the far-field scattering image is proportional to the squared Fourier amplitude of the projected target density onto the scattering plane. In this regime phase retrieval algorithms can be utilized. Scattering with larger wavelength radiation enables the resolution of larger scattering angles, in which the diffraction pattern is dependent on the orientation of the target. It has been shown that wide angle diffraction patterns can be computed by the multislice Fourier transform method (MSFT), that can include a simple absorption model. Atomic resolution of the target cannot be accessed in the simple continuum approach. To this end, the well-established discrete dipole approximation has been derived, that builds on the description of the target as an ensemble of discrete point dipoles.

The third chapter introduced an intuitive approach to solve the discrete dipole approximation by a complex scaling mixing (CSDDA). The numerical models MSFT and CSDDA have been applied to systematically analyze the influence of wavelength on the diffraction patterns. It could be clarified, that the wide-angle scattering regime only is applicable with soft x-ray and extreme ultraviolet (XUV) radiation. However, it also became evident that in this regime the influence of absorption largely impacts the diffraction pattern by blurring the fringe structure and raising the scattering signal at larger scattering angles. By decreasing the wavelength, the non-symmetric diffraction patterns go towards a point-symmetric diffraction pattern in the small angle scattering regime, which is an indication of the diffraction pattern only being dependent on the projected particle density. A second laser parameter that has been studied was the pulse duration. It could be shown, that for pulse durations reached in free electron lasers the large bandwidth does not affect the diffraction patterns. Only for very short pulses on the order of a few tens of attoseconds, the diffraction pattern alters by a decreasing fringe contrast. For a certain pulse duration

the fringe contrast gets lost. Due to the larger absorption at large wavelength the already smaller contrast of the fringes, leads to the critical pulse durations being larger than for smaller wavelength. Further, the fringe contrast gets lost at larger scattering angles already at longer pulse durations. When the fringe contrast is lost, information about the size of the target is hidden, however, the orientation of the target can still be inferred from the diffraction pattern. Hence, even in this case, still useful insights about the target can be gained, meaning that attosecond imaging is feasible. The simple estimate presented in the study can be used to find the trade-off between pulse duration and resolution that can be achieved with a certain wavelength.

In chapter four and five, MSFT and DDA have been applied for reconstruction of particle properties such as shape and optical properties from experimental diffraction patterns. Two different samples were investigated, hydrogen jets and helium nanodroplets.
Chapter four showed that the diffraction patterns from cylindrical jets highly depend on the utilized laser parameters. The typical diffraction pattern of a jet appears as a streak perpendicular to the jet axis. The width of that streak depends on the spot size of the incoming laser pulse. Further, the streak signal depends on the strength of the scattering from the shape (coherent scattering), whereas the signal strength beside the streak depends on the strength of the scattering from structural disorder (incoherent scattering). For a jet both contributions can be on the same order and therefore are resolvable on a single detector. In the single-shot diffractive imaging experiment on solid-state hydrogen jets not a single streak could be observed, but multiple streaks with differing intensities and rotation angles. A few properties of the diffraction patterns could be connected to possible jet shape variations. However, it could not be verified that the structure of the diffraction patterns uniquely emerge from the different jet shapes, since the incident laser pulse from FLASH had a noisy spectrum. The analysis could be highly simplified by performing such an experiment at a FEL generating smooth pulse shapes, e. g. generated at seeded FELs such as FERMI.
In chapter five, it was shown that although multicolor diffraction patterns from high harmonic generation sources complicate the reconstruction of the target shape, the existence of different wavelength in the spectrum can allow for reconstruction of the refractive indices. A simplex Mie fit routine for extracting optical properties from multicolor diffraction patterns of spherical droplets has been implemented. It could be shown that the refractive indices close to the helium 1s2p resonance can be inferred from the diffraction patterns of the spherical droplets. However, due to the photon energies of the two harmonics with unknown refractive indices lying very close to each other, they can interchange their roles by adaption of the cluster radius. The simplex fit procedure could be improved if the number of harmonics with unknown refractive indices could be decreased or their photon energies lie further away from each other. For future experiments with attosecond resolution, it became clear that a multicolor analysis of the diffraction patterns is key for retrieving useful information from the experiment. A second result, presented in the chapter was the 3D reconstruction of a pill-shaped droplet by MSFT and CSDDA

by comparison to the experimental wide angle diffraction patterns that are dependent on the orientation of the target. That demonstrated that superfluid helium droplets can exist in such shapes that had been excluded by previous studies [48]. This study shows that the behavior of superfluid helium droplets and the shapes they can form when rotating are not yet well understood and hence, are an interesting object for future research.

The last chapter was dedicated to a different reconstruction approach, the iterative phase retrieval algorithm. It could be shown that a two-color imaging setup that simultaneously records small and wide angle diffraction patterns, can simplify the task of finding the correct orientation of a randomly oriented reproducible target. This task is key to access the 3D Fourier amplitude of the imaged object, and finally perform a 3D phase retrieval algorithm to reconstruct the 3D particle density. By comparison to a database that covers all Euler angles it could be shown that orientation retrieval is feasible for asymmetric and symmetric targets. Although the orientation tagging task can be solved by comparison to a database of diffraction patterns, for this approach the target outer shape needs to be known. A large improvement would be to directly reconstruct the 3D orientation from the diffraction pattern. This should be possible, since the information is encoded in the diffraction pattern. However, so far, no methods are available to solve this task without some knowledge about the target.

A. CSDDA compared to Krylov-subspace methods

The aim of the discrete dipole approximation (DDA) is to find a self-consistent solution for the local electric field $\mathbf{E}_{\mathrm{loc}}(\mathbf{r}_j)$ at each dipole position $\mathbf{r}_j$ (cf. eq. 2.75)

$$\mathbf{E}_{\mathrm{loc}}(\mathbf{r}_j) = \mathbf{E}_{\mathrm{inc}}(\mathbf{r}_j) + \alpha(\omega)\omega^2\mu_0 \sum_{n\neq j} \overleftrightarrow{\mathbf{G}}(\mathbf{r}_j, \mathbf{r}_n)\mathbf{E}_{\mathrm{loc}}(\mathbf{r}_n). \tag{A.1}$$

with $\mathbf{E}_{\mathrm{inc}}(\mathbf{r}_j)$ denoting the incident electric field, ω the light frequency, α the frequency-dependent polarizability and μ_0 permeability of free space. The dyadic Green's function for electromagnetic scattering is

$$\overleftrightarrow{\mathbf{G}}(\mathbf{R}) = \frac{\exp(ikR)}{4\pi R}\left[\left(1 + \frac{ikR-1}{k^2R^2}\right)\overleftrightarrow{\mathbf{I}} + \frac{3-3ikR-k^2R^2}{k^2R^2}\frac{\mathbf{R}\otimes\mathbf{R}}{R^2}\right], \tag{A.2}$$

with the distance between dipole and observation point $R = |\mathbf{r}_j - \mathbf{r}|$ and the wave number k. In the following, the dyadic Green's function and the prefactors in eq. (A.1) are combined to $\overleftrightarrow{\mathbf{A}} = \alpha(\omega)\omega^2\mu_0 \sum_{n\neq j} \overleftrightarrow{\mathbf{G}}(\mathbf{R})$. Inserting this into eq. (A.1) and rearranging the equation gives

$$\mathbf{E}_{\mathrm{inc}}(\mathbf{r}_j) = \left(1 - \overleftrightarrow{\mathbf{A}}\right)\mathbf{E}_{\mathrm{loc}}(\mathbf{r}_j), \tag{A.3}$$

where $1 - \overleftrightarrow{\mathbf{A}}$ is a symmetric matrix. The above equation represents a linear system of equations of the form $b = Ax$ and can be solved using Krylov-subspace methods [71]. These methods are based on the assumption that the unknown x lies in the affine space

$$x = x_0 + \mathcal{K}_r(A, b), \tag{A.4}$$

with

$$\mathcal{K}_r(A, b) = \mathrm{span}\{b, Ab, A^2b, \ldots, A^{r-1}b\}, \tag{A.5}$$

where r is the degree of the subspace $\mathcal{K}$. An overview of different Krylov subspace methods can be found in [113].

Numerical implementations for solving the discrete dipole approximation utilizing Krylov subspace methods are available as the DDSCAT code by Bruce T. Draine [29] and ADDA by Maxim Yurkin [143]. Here, ADDA is used to compare the state-of-the-art Krylov subspace methods to the complex scaling discrete dipole approximation (CSDDA). The different implementations of the discrete dipole approximation not only use different meth-

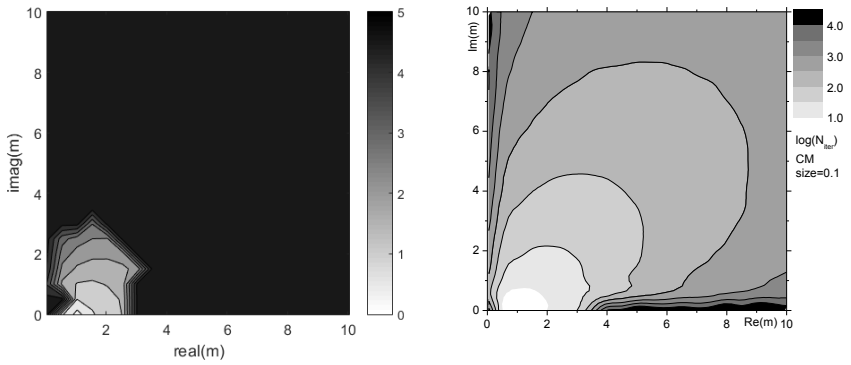

Figure A.1.: Number of iterations needed to converge for a spherical target for different refractive indices for CSDDA (left) and quasi-minimal residual method (QMR). The polarizability is connected to the refractive index with the Clausius-Mossotti relation. The size parameter is set to $kR = 0.1$. Left plot in courtesy of Maxim Yurkin.

ods for solving the linear system of equations but also different descriptions of the complex polarizability. Here, the polarizability is described by the Clausius-Mossotti relation via

$$\frac{\epsilon_r - 1}{\epsilon_r + 2} = \frac{n_a \alpha}{3\epsilon_0}, \tag{A.6}$$

with the material specific dielectric constant $\epsilon_r = \epsilon/\epsilon_0$ with the permittivity ϵ_0 of free space and n_a denoting the number density. The permittivity ϵ is connected to the complex refractive index m via

$$m = \sqrt{\epsilon_r}. \tag{A.7}$$

The CSDDA is compared to the Krylov subspace method quasi-minimal residual (QMR) for a spherical target with a size parameter $kR = 0.1$. The number of iterations necessary for convergence is computed for different refractive indices. Convergence is reached when the error falls below the limit $\Delta < 1\mathrm{e} - 5$. The results are depicted in Fig. A.1. The left plot shows the results for CSDDA and the right plot the results for QMR. For the black areas in the left plots, no convergence can be reached. Hence, it becomes obvious that CSDDA is only reasonable to use for refractive indices very close to unity, where the performance is similar to the Krylov subspace method. Still, the implementation of

CSDDA has some advantages compared to the more efficient Krylov subspace methods. It is simple to implement and it is an intuitive solution of the discrete dipole approximation. Further, the dipoles can be distributed randomly and do not have to be distributed on a regular grid. In ADDA this is not implemented, since the computation is accelerated by a FFT-convolution method, which only is applicable for regular spacing. Hence, the CSDDA offers the possibility to compute the discrete dipole approximation e. g. for crystal lattices in face-centered cubic structure with atomic resolution.

B. Mie Theory

The Mie theory [84] gives a solution to the scattered electric field by a plane wave for absorbing, homogeneous spherical, cylindrical or elliptical targets by solving the Maxwell's equations. It is applicable to all sizes of targets, wavelengths and refractive indices. The Maxwell's equations are solved in spherical coordinates. The incident plane wave is expanded in Legendre Polynomials allowing the matching of the solutions inside and outside of the spherical object. The Mie theory gives the solution of scattering functions in the far-field via

$$S_1(\theta) = \sum_{n=1}^{\infty} \frac{2n+1}{n(n+1)} [a_n \pi_n(\cos(\theta)) + b_n \tau_n(\cos(\theta))], \tag{B.1}$$

$$S_2(\theta) = \sum_{n=1}^{\infty} \frac{2n+1}{n(n+1)} [b_n \pi_n(\cos(\theta)) + a_n \tau_n(\cos(\theta))], \tag{B.2}$$

with the scattering angle θ. The coefficients π_n and τ_n are functions of Legendre Polynomials of first kind P_n^1 and are given by

$$\pi_n(\cos(\theta)) = \frac{1}{\sin(\theta)} P_n^1(\cos(\theta)) \tag{B.3}$$

$$\tau_n(\cos(\theta)) = \frac{d}{d\theta} P_n^1(\cos(\theta)) \tag{B.4}$$

The coefficients a_n and b_n are given by

$$a_n = \frac{\Psi_n'(m\alpha)\Psi_n(\alpha) - m\Psi_n(m\alpha)\Psi_n'(\alpha)}{\Psi_n'(m\alpha)\xi_n(\alpha) - m\Psi_n(m\alpha)\xi'(\alpha)}, \tag{B.5}$$

$$b_n = \frac{m\Psi_n'(m\alpha)\Psi_n(\alpha) - \Psi_n(m\alpha)\Psi_n'(\alpha)}{m\Psi_n'(m\alpha)\xi_n(\alpha) - \Psi_n(m\alpha)\xi'(\alpha)}, \tag{B.6}$$

where m denotes the refractive index, α is the size parameter $\alpha = kR$, with the sphere radius R and the wave number k. Further, Ψ_n and ξ_n are the Riccatty-Bessel functions, Ψ_n' and ξ_n' its derivatives with respect to radial distance r. They are functions of spherical Bessel functions j_n and n_n of first and second kind given by

$$\Psi_n(t) = t j_n(t) \tag{B.7}$$

$$\xi_n(t) = t n_n(t). \tag{B.8}$$

The scattered electric field $\mathbf{E}_{\text{scatt}}$ then is connected to the incident electric field $\mathbf{E}_{\text{inc}}$ via

$$\mathbf{E}_{\text{scatt}} = \frac{e^{-ikr+ikz}}{ikr} \left[\begin{pmatrix} S_2(\theta) & 0 \\ 0 & S_1(\theta) \end{pmatrix} \right] \mathbf{E}_{\text{inc}}, \tag{B.9}$$

Hence, the scattered electric field in Mie theory basically is an infinite sum of spherical multipole partial waves. In the simulation, the sum is computed up to a certain order where the solution converged.

C. Simplex Mie fits

The simplex Mie fits utilized in chp. 5 are plotted in the following. The scattered intensity is composed of four Mie intensities from four harmonics with different intensity scalings c via (cf. eq. (5.1))

$$I_{\text{fit}} = c_{11} I_{\text{mie},11} + c_{13} I_{\text{mie},13} + c_{15} I_{\text{mie},15} + c_{17} I_{\text{mie},17}, \tag{C.1}$$

Each Mie intensity is dependent on sphere radius R and refractive index n. The fits for refractive indices fixed to the literature values

$$\begin{aligned} n_{11} &= 0.97 + i0 \\ n_{13} &= 1.14 + i0.032 \\ n_{15} &= 1.03 + i0.029 \\ n_{17} &= 1.0036 + i0.041 \end{aligned}$$

and the intensity scalings and radius treated as fit parameters are depicted in Fig. C.1. The fits with the intensity scalings (according to Fig. 5.2b) being fixed

$$\begin{aligned} c_{11} &= 0.21 \\ c_{13} &= 0.82 \\ c_{15} &= 1.0 \\ c_{17} &= 0.29 \end{aligned}$$

and the radius and refractive index of 13th and 15th harmonic being the fit parameters is shown in Figs. C.2 and C.3 for the solution of the 15th harmonic and the 13th harmonic being dominant, respectively.

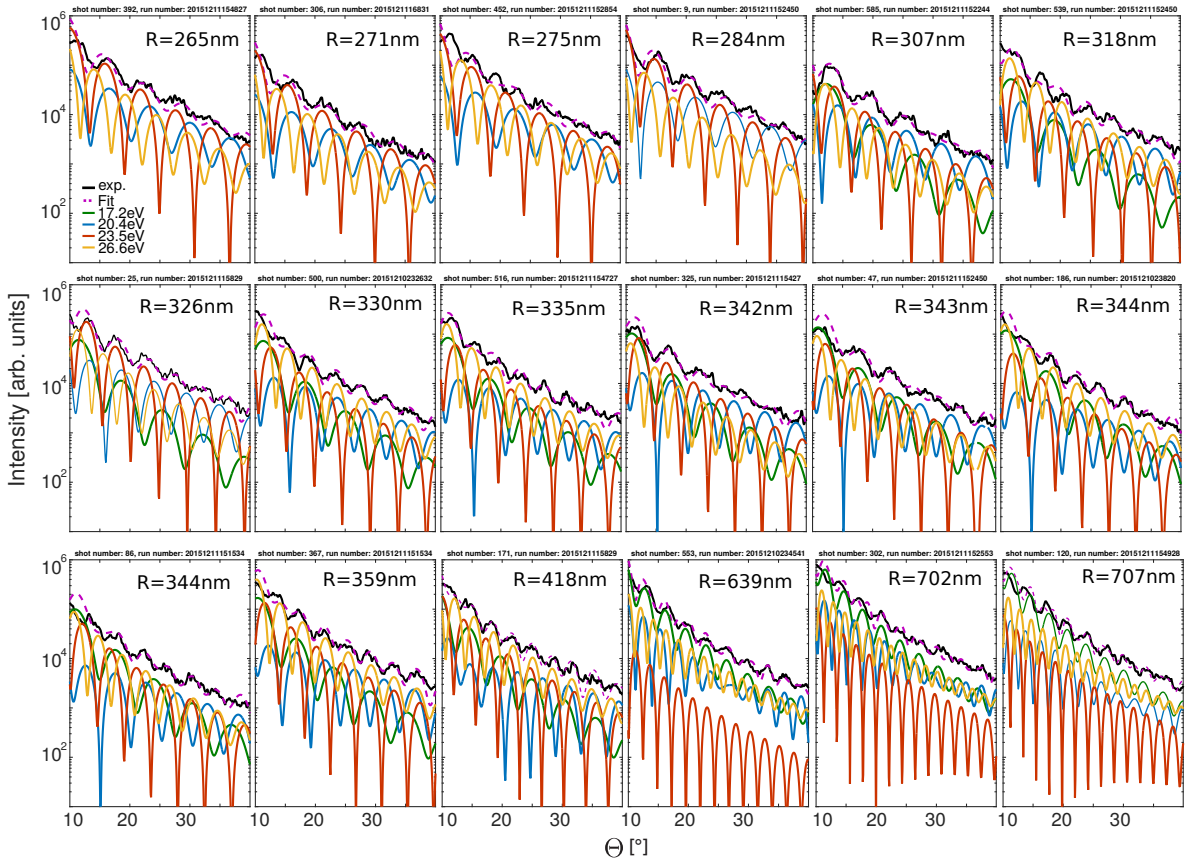

Figure C.1.: Simplex Mie fits for 18 selected diffraction patterns with open intensity scalings and refractive indices fixed to literature values. From supplementary material from [109].

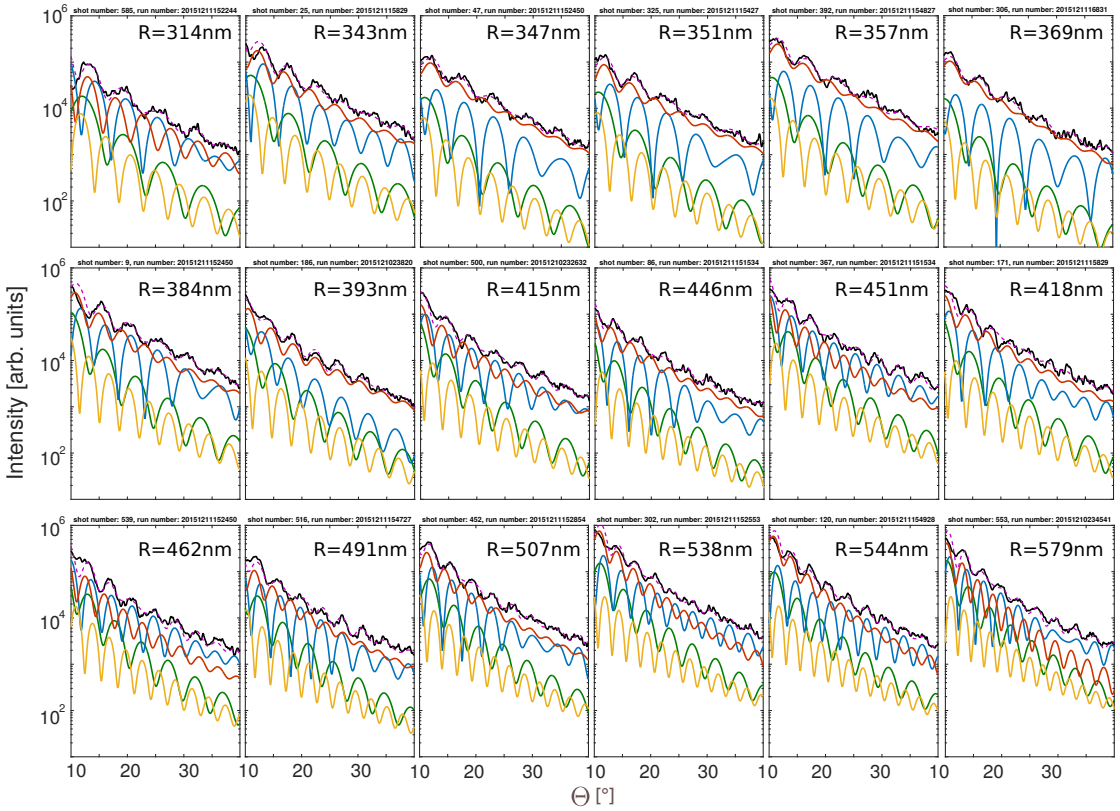

Figure C.2.: Simplex Mie fits for 18 selected diffraction patterns with 13th harmonic dominant. From supplementary material from [109].

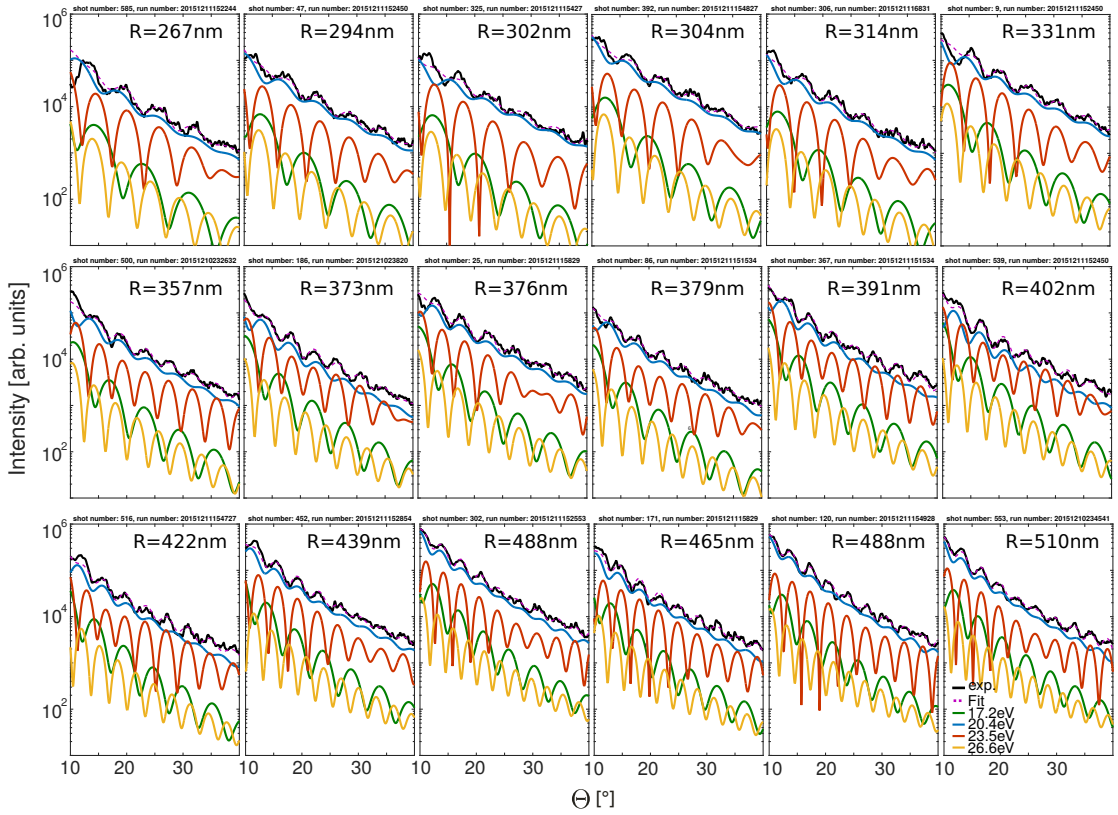

Figure C.3.: Simplex Mie fits for 18 selected diffraction patterns with 15th harmonic dominant. From supplementary material from [109].

D. Phase retrieval algorithm

In a single-shot diffractive imaging experiment the scattered intensity is measured as

$$I_{\text{scatt}} = \frac{c\epsilon_0}{2}|\hat{E}|^2, \tag{D.1}$$

which is proportional to the field amplitude of the scattered electric field, however, the phase of the field is lost. Phase retrieval algorithms are well-established methods for solving this phase problem and offer the possibility of reconstructing the target from the diffraction patterns without information about the exact target shape. Starting point of the phase retrieval algorithms is the Born result (eq. (2.45)), i. e. it is important to know that the scattered electric field is proportional to the Fourier transform of the particle density. And then vice versa, the particle density is proportional to the inverse Fourier transform of the scattered electric field. Note that the Born result does not include absorption and therefore phase retrieval is only applicable to weak scattering scenarios. In all phase retrieval algorithms four basic steps are performed. First, the scattered electric field at the detector is constructed by taking the field amplitude from the scattered intensity of the diffraction pattern and guessing a phase Φ_0: $E^0 = \sqrt{I}\exp(i\Phi_0)$. In the first step, the object density $\tilde{\rho}$ for iteration j is obtained via

$$\tilde{\rho}^j = \mathcal{FT}^{-1}(E^j). \tag{D.2}$$

Second, the object density is updated by satisfying a function constraint e. g. with the output-output scheme [37] with

$$\rho^{j+1}(x \in \Sigma) = \tilde{\rho}^j(x \in \Sigma), \tag{D.3}$$

$$\rho^{j+1}(\notin \Sigma) = \tilde{\rho}^j(x \notin \Sigma) - \beta\tilde{\rho}^j(x \notin \Sigma), \tag{D.4}$$

where Σ is the mask. The mask can be adapted in each step via a shrinkwrap algorithm [79]. Then, in the third step, a new estimate for the electric field $\tilde{E}$ is obtained via

$$\tilde{E}^{j+1} = \mathcal{FT}(\rho^{j+1}) = \hat{E}^{j+1}\exp(i\Phi^{j+1}). \tag{D.5}$$

In the fourth step, the Fourier constraints need to be satisfied by exchanging the electric field amplitude with the electric field amplitude obtained by the experiment or simulation, the electric field phase is kept

$$E^{j+1} = \sqrt{I}\exp(i\Phi^{j+1}). \tag{D.6}$$

This step is the same for all phase retrieval schemes. The four steps are repeated until convergence is reached, which can be measured by computing the error ϵ in each iteration j via

$$\epsilon^j = \sqrt{\frac{\sum(\hat{E}^j - \sqrt{I})^2}{\sum I}}. \tag{D.7}$$

This phase retrieval scheme can be applied to 2D diffraction patterns to obtain the projected particle density (cf. eq. (2.49)) and if the amplitude of the 3D Fourier transform of the particle can be recovered, also to obtain the 3D particle density.

Bibliography

[1] M. Adrian, J. Dubochet, J. Lepault, and A. W. McDowall, "Cryo-electron microscopy of viruses", *Nature*, vol. 308, 32, 1984.

[2] E. Allaria, L. Badano, S. Bassanese, et al., "The fermi free-electron lasers", *Journal of Synchrotron Radiation*, vol. 22, 485–491, 2015.

[3] F. Ancilotto, M. Barranco, and M. Pi, "Spinning superfluid helium-4 nanodroplets", *arXiv*, 2017. [Online]. Available: https://arxiv.org/abs/1711.03750.

[4] F. Ancilotto, M. Pi, and M. Barranco, "Vortex arrays in nanoscopic superfluid helium droplets", *Phys. Rev. B*, vol. 91, 100503, 2015.

[5] S. Asano and G. Yamamoto, "Light scattering by a spheroidal particle", *Appl. Opt.*, vol. 14, 29–49, 1975.

[6] K. Ayyer, H. T. Philipp, M. W. Tate, V. Elser, and S. M. Gruner, "Real-space x-ray tomographic reconstruction of randomly oriented objects with sparse data frames", *Optics Express*, vol. 22, 2403–2413, 2014.

[7] K. Ayyer, H. T. Philipp, M. W. Tate, J. L. Wierman, V. Elser, and S. M. Gruner, "Determination of crystallographic intensities from sparse data", *IUCrJ*, vol. 2, 29–34, 2014.

[8] K. Ayyer, O. M. Yefanov, D. Oberthar, et al., "Macromolecular diffractive imaging using imperfect crystals", *Nature*, vol. 530, 202–206, 2016.

[9] K. A. Baldwin, S. L. Butler, and R. J. A. Hill, "Artificial tektites: an experimental technique for capturing the shapes of spinning drops", *Scientific Reports*, vol. 5, 7660, 2014.

[10] I. Barke, H. Hartmann, D. Rupp, et al., "The 3d-architecture of individual free silver nanoparticles captured by x-ray scattering", *Nat Commun*, vol. 6, 6187, 4, 2015.

[11] R. Bates, "Fourier phase problems are solvable in more than one dimension. i: Underlying theory". 1982, vol. 61.

[12] M. J. Bogan, W. H. Benner, S. Boutet, et al., "Single particle x-ray diffractive imaging", *Nano Lett.*, vol. 8, 310–316, 2008.

[13] C. Bostedt, M. Adolph, E. Eremina, M. Hoener, D. Rupp, S. Schorb, H. Thomas, A. R. B. de Castro, and T. Möller, "Clusters in intense flash pulses: ultrafast ionization dynamics and electron emission studied with spectroscopic and scattering techniques", *Journal of Physics B: Atomic, Molecular and Optical Physics*, vol. 43, 194011, 2010.

[14] C. Bostedt, E. Eremina, D. Rupp, et al., "Ultrafast x-ray scattering of xenon nanoparticles: imaging transient states of matter", *Phys. Rev. Lett.*, vol. 108, 093401, 2012.

[15] R. A. Brown and . E. Scriven, "The shape and stability of rotating liquid drops", *Proc R Soc Lond A Math Phys Sci*, vol. 371, 331, 1980.

[16] Y. Bruck and L. Sodin, "On the ambiguity of the image reconstruction problem", *Optics Communications*, vol. 30, 304–308, 1979.

[17] C. Burda, X. Chen, R. Narayanan, and M. A. El-Sayed, "Chemistry and properties of nanocrystals of different shapes", *Chemical Reviews*, vol. 105, 1025–1102, 2005, PMID: 15826010.

[18] H. H. Chang, M. Y. Lai, J. H. Wei, C. M. Wei, and Y. L. Wang, "Structure determination of surface magic clusters", *Phys. Rev. Lett.*, vol. 92, 066103, 2004.

[19] C. T. Chantler, "Theoretical form factor, attenuation, and scattering tabulation for z=1–92 from e=1–10 ev to e=0.4–1.0 mev", *Journal of Physical and Chemical Reference Data*, vol. 24, 71–643, 1995.

[20] H. N. Chapman, P. Fromme, A. Barty, et al., "Femtosecond x-ray protein nanocrystallography", *Nature*, vol. 470, 73, 2011.

[21] H. N. Chapman, A. Barty, M. J. Bogan, et al., "Femtosecond diffractive imaging with a soft-x-ray free-electron laser", *Nature Physics*, vol. 2, 839, 2006.

[22] H. N. Chapman and K. A. Nugent, "Coherent lensless x-ray imaging", *Nat Photon*, vol. 4, 833–839, 2010.

[23] B. Chen, R. A. Dilanian, S. Teichmann, B. Abbey, A. G. Peele, G. J. Williams, P. Hannaford, L. Van Dao, H. M. Quiney, and K. A. Nugent, "Multiple wavelength diffractive imaging", *Phys. Rev. A*, vol. 79, 023809, 2009.

[24] P. B. Corkum, "Plasma perspective on strong field multiphoton ionization", *Phys. Rev. Lett.*, vol. 71, 1994–1997, 1993.

[25] J. M. Cowley and A. F. Moodie, "The scattering of electrons by atoms and crystals. I. A new theoretical approach", *Acta Crystallographica*, vol. 10, 609–619, 1957.

[26] A. N. M. D. A. Varshalovich and V. K. Khersonskii, "Quantum Theory of Angular Momentum". 1988, Original Russian edition: Nauka, 1975.

[27] M. Dierolf, A. Menzel, P. Thibault, P. Schneider, C. M. Kewish, R. Wepf, O. Bunk, and F. Pfeiffer, "Ptychographic x-ray computed tomography at the nanoscale", *Nature*, vol. 467, 436, 2010.

[28] J. J. Donatelli, P. H. Zwart, and J. A. Sethian, "Iterative phasing for fluctuation x-ray scattering", *Proceedings of the National Academy of Sciences of the United States of America*, vol. 112, 10286–10291, 2015.

[29] B. T. Draine and P. J. Flatau, "Discrete-dipole approximation for scattering calculations", *J. Opt. Soc. Am. A*, vol. 11, 1491–1499, 1994.

[30] B. T. Draine and J. Goodman, "Beyond clausius-mossotti - wave propagation on a polarizable point lattice and the discrete dipole approximation", *Astrophysical Journal*, vol. 405, 685–697, 1993.

[31] B. Draine, "The discrete dipole approximation and its applications to interstellar graphite grains", *The Astrophysical Journal*, vol. 333, 848–872, 1988.

[32] R. Drezek, A. Dunn, and R. Richards-Kortum, "Light scattering from cells: finite-difference time-domain simulations and goniometric measurements", *Appl. Opt.*, vol. 38, 3651–3661, 1999.

[33] A. Dunn and R. Richards-Kortum, "Three-dimensional computation of light scattering from cells", *IEEE Journal of Selected Topics in Quantum Electronics*, vol. 2, 898–905, 1996.

[34] T. Ekeberg, M. Svenda, C. Abergel, et al., "Three-dimensional reconstruction of the giant mimivirus particle with an x-ray free-electron laser", *Phys. Rev. Lett.*, vol. 114, 098102, 2015.

[35] P. Emma, R. Akre, J. Arthur, et al., "First lasing and operation of an angstrom-wavelength free-electron laser", *Nat Photon*, vol. 4, 641–647, 2010.

[36] J. Feldhaus, J. Arthur, and J. B. Hastings, "X-ray free-electron lasers", *Journal of Physics B: Atomic, Molecular and Optical Physics*, vol. 38, S799, 2005.

[37] J. R. Fienup, "Phase retrieval algorithms: a comparison", *Appl. Opt.*, vol. 21, 2758–2769, 1982.

[38] ——, "Reconstruction of an object from the modulus of its fourier transform", *Opt. Lett.*, vol. 3, 27–29, 1978.

[39] F. Frassetto, A. Trabattoni, S. Anumula, G. Sansone, F. Calegari, M. Nisoli, and L. Poletto, "High-throughput beamline for attosecond pulses based on toroidal mirrors with microfocusing capabilities", *Review of Scientific Instruments*, vol. 85, 103115, 2014.

[40] R. Fung, V. Shneerson, D. K. Saldin, and A. Ourmazd, "Structure from fleeting illumination of faint spinning objects in flight", *Nat Phys*, vol. 5, 64–67, 2009.

[41] K. J. Gaffney and H. N. Chapman, "Imaging atomic structure and dynamics with ultrafast x-ray scattering", *Science*, vol. 316, 1444–1448, 2007.

[42] M. Gallagher-Jones, Y. Bessho, S. Kim, et al., "Macromolecular structures probed by combining single-shot free-electron laser diffraction with synchrotron coherent x-ray imaging", vol. 5, 3798, 2014.

[43] R. Gerchberg and A. Saxton W. O., "A practical algorithm for the determination of phase from image and diffraction plane pictures". 1971, vol. 35, 237–250.

[44] D. O. Gericke, J. Vorberger, K. Wünsch, and G. Gregori, "Screening of ionic cores in partially ionized plasmas within linear response", *Phys. Rev. E*, vol. 81, 065401, 2010.

[45] D. Giannakis, P. Schwander, and A. Ourmazd, "The symmetries of image formation by scattering. i. theoretical framework", *Opt. Express*, vol. 20, 12799–12826, 2012.

[46] S. H. Glenzer, L. B. Fletcher, E. Galtier, et al., "Matter under extreme conditions experiments at the linac coherent light source", *Journal of Physics B: Atomic, Molecular and Optical Physics*, vol. 49, 092001, 2016.

[47] S. H. Glenzer, O. L. Landen, P. Neumayer, et al., "Observations of plasmons in warm dense matter", *Phys. Rev. Lett.*, vol. 98, 065002, 2007.

[48] L. F. Gomez, K. R. Ferguson, J. P. Cryan, et al., "Shapes and vorticities of superfluid helium nanodroplets", *Science*, vol. 345, 906–909, 2014.

[49] T. Gorkhover, S. Schorb, R. Coffee, et al., "Femtosecond and nanometre visualization of structural dynamics in superheated nanoparticles", *Nat Photon*, vol. 10, 93–97, 2016.

[50] T. Gorkhover, A. Ulmer, K. Ferguson, et al., "Femtosecond x-ray fourier holography imaging of free-flying nanoparticles", *Nature Photonics*, vol. 12, 150–153, 2018.

[51] G. Gregori, S. H. Glenzer, W. Rozmus, R. W. Lee, and O. L. Landen, "Theoretical model of x-ray scattering as a dense matter probe", *Phys. Rev. E*, vol. 67, 026412, 2003.

[52] T. Guillot, "Interiors of giant planets inside and outside the solar system", *Science*, vol. 286, 72–77, 1999.

[53] S. Hädrich, M. Krebs, J. Rothhardt, H. Carstens, S. Demmler, J. Limpert, and A. Tünnermann, "Generation of μw level plateau harmonics at high repetition rate", *Opt. Express*, vol. 19, 19374–19383, 2011.

[54] A. Hare and G. Morrison, "Near-field soft x-ray diffraction modelled by the multislice method", *Journal of Modern Optics*, vol. 41, 31–48, 1994.

[55] M. Hayes, "The reconstruction of a multidimensional sequence from the phase or magnitude of its fourier transform", *IEEE Transactions on Acoustics, Speech, and Signal Processing*, vol. 30, 140–154, 1982.

[56] S. W. Hell and J. Wichmann, "Breaking the diffraction resolution limit by stimulated emission: stimulated-emission-depletion fluorescence microscopy", *Opt. Lett.*, vol. 19, 780–782, 1994.

[57] B. L. Henke, E. M. Gullikson, and J. C. Davis, "X-ray interactions: photoabsorption, scattering, transmission, and reflection at e = 50-30,000 ev, z = 1-92", *Atomic Data and Nuclear Data Tables*, vol. 54, 181–342, 1993.

[58] J.-F. Hergott, M. Kovacev, H. Merdji, C. Hubert, Y. Mairesse, E. Jean, P. Breger, P. Agostini, B. Carre, and P. Salieres, "Extreme-ultraviolet high-order harmonic pulses in the microjoule range", *Phys. Rev. A*, vol. 66, 021801, 2002.

[59] A. Hoekstra, J. Rahola, and P. Sloot, "Accuracy of internal fields in volume integral equation simulations of light scattering", *Appl. Opt.*, vol. 37, 8482–8497, 1998.

[60] E. Hofstetter, "Construction of time-limited functions with specified autocorrelation functions", *IEEE Transactions on Information Theory*, vol. 10, 119–126, 1964.

[61] K.-H. Hong, C.-J. Lai, J. P. Siqueira, P. Krogen, J. Moses, C.-L. Chang, G. J. Stein, L. E. Zapata, and F. X. K"artner, "Multi-mj, khz, 2.1μm optical parametric chirped-pulse amplifier and high-flux soft x-ray high-harmonic generation", *Opt. Lett.*, vol. 39, 3145–3148, 2014.

[62] A. Hosseinizadeha, A. Dashtia, P. Schwander, R. Fung, and A. Ourmazd, "Single-particle structure determination by x-ray free-electron lasers: possibilities and challenges", *Structural Dynamics*, vol. 2, 2015.

[63] Z. Huang, "Brightness and coherence of synchrotron radiation and fels", *Proc. 4th Int. Particle Accelerater Conf. (IPAC 2013)*, 2013. [Online]. Available: `https://accelconf.web.cern.ch/accelconf/IPAC2013/html/author.ht`.

[64] H. C. van de Hulst, "Light scattering by small particles", Q. J. of the Royal Meteorological Society, Ed. 1957.

[65] T. Ishikawa, H. Aoyagi, T. Asaka, et al., "A compact x-ray free-electron laser emitting in the sub-angstrom region", *Nat Photon*, vol. 6, 540–544, 2012.

[66] M. Joppien, R. Karnbach, and T. Möller, "Electronic excitations in liquid helium: the evolution from small clusters to large droplets", *Phys. Rev. Lett.*, vol. 71, 2654–2657, 1993.

[67] Z. Kam, "Determination of macromolecular structure in solution by spatial correlation of scattering fluctuations", *Macromolecules*, vol. 10, 927–934, 1977.

[68] S. Kassemeyer, A. Jafarpour, L. Lomb, J. Steinbrener, A. V. Martin, and I. Schlichting, "Optimal mapping of x-ray laser diffraction patterns into three dimensions using routing algorithms", *Phys. Rev. E*, vol. 88, 042710, 2013.

[69] J. B. Kim, S. Göde, and S. H. Glenzer, "Development of a cryogenic hydrogen microjet for high-intensity, high-repetition rate experiments", *Review of Scientific Instruments*, vol. 87, 11E328, 2016.

[70] F. Krausz and M. Ivanov, "Attosecond physics", *Rev. Mod. Phys.*, vol. 81, 163–234, 2009.

[71] A. N. Krylov, "On the numerical solution of the equation by which in technical questions frequencies of small oscillations of material systems are determined", *Izvestija AN SSSR*, vol. II, 491–539, 1931.

[72] B. Langbehn, K. Sander, Y. Ovcharenko, et al., "Three-dimensional shapes of spinning helium nanodroplets", *Phys. Rev. Lett.*, vol. 121, 255301, 2018.

[73] K.-S. Lee and M. A. El-Sayed, "Gold and silver nanoparticles in sensing and imaging: sensitivity of plasmon response to size, shape, and metal composition", *The Journal of Physical Chemistry B*, vol. 110, 19220–19225, 2006.

[74] J. D. Lindl, P. Amendt, R. L. Berger, S. G. Glendinning, S. H. Glenzer, S. W. Haan, R. L. Kauffman, O. L. Landen, and L. J. Suter, "The physics basis for ignition using indirect-drive targets on the national ignition facility", *Physics of Plasmas*, vol. 11, 339–491, 2004.

[75] N. D. Loh, M. J. Bogan, V. Elser, et al., "Cryptotomography: reconstructing 3d fourier intensities from randomly oriented single-shot diffraction patterns", *Phys. Rev. Lett.*, vol. 104, 225501, 2010.

[76] N. D. Loh, C. Y. Hampton, A. V. Martin, et al., "Fractal morphology, imaging and mass spectrometry of single aerosol particles in flight", *Nature*, vol. 489, 513–517, 2012.

[77] N.-T. D. Loh and V. Elser, "Reconstruction algorithm for single-particle diffraction imaging experiments", *Phys. Rev. E*, vol. 80, 026705, 2009.

[78] A. A. Lucas, J. P. Vigneron, S. E. Donnelly, and J. C. Rife, "Theoretical interpretation of the vacuum ultraviolet reflectance of liquid helium and of the absorption spectra of helium microbubbles in aluminum", *Phys. Rev. B*, vol. 28, 2485–2496, 1983.

[79] S. Marchesini, H. He, H. N. Chapman, S. P. Hau-Riege, A. Noy, M. R. Howells, U. Weierstall, and J. C. H. Spence, "X-ray image reconstruction from a diffraction pattern alone", *Phys. Rev. B*, vol. 68, 140101, 2003.

[80] J. C. Maxwell, "A dynamical theory of the electromagnetic field", *Philosophical Transactions of the Royal Society of London*, vol. 155, 459–512, 1865.

[81] J. Miao, P. Charalambous, J. Kirz, and D. Sayre, "Extending the methodology of x-ray crystallography to allow imaging of micrometre-sized non-crystalline specimens", *Nature*, vol. 400, 342–344, 1999.

[82] J. Miao, T. Ishikawa, E. H. Anderson, and K. O. Hodgson, "Phase retrieval of diffraction patterns from noncrystalline samples using the oversampling method", *Phys. Rev. B*, vol. 67, 174104, 2003.

[83] J. Miao, T. Ishikawa, I. K. Robinson, and M. M. Murnane, "Beyond crystallography: diffractive imaging using coherent x-ray light sources", *Science*, vol. 348, 530, 2015.

[84] G. Mie, "Beiträge zur optik trüber medien, speziell kolloidaler metallösungen", *Ann. Phys.*, vol. 330, 377, 1908.

[85] R. P. Millane, "Phase retrieval in crystallography and optics", *J. Opt. Soc. Am. A*, vol. 7, 394–411, 1990.

[86] S. V. Milton, E. Gluskin, N. D. Arnold, et al., "Exponential gain and saturation of a self-amplified spontaneous emission free-electron laser", *Science*, vol. 292, 2037–2041, 2001.

[87] M. I. Mishchenko and M. A. Yurkin, "On the concept of random orientation in far-field electromagnetic scattering by nonspherical particles", *Opt. Lett.*, vol. 42, 494–497, 2017.

[88] M. Morcrette, Y. Chabre, G. Vaughan, G. Amatucci, J.-B. Leriche, S. Patoux, C. Masquelier, and J.-M. Tarascon, "In situ x-ray diffraction techniques as a powerful tool to study battery electrode materials", *Electrochimica Acta*, vol. 47, 3137–3149, 2002.

[89] B. Moths and A. Ourmazd, "Bayesian algorithms for recovering structure from single-particle diffraction snapshots of unknown orientation: a comparison", *Acta Crystallographica Section A: Foundations of Crystallography*, vol. 67, 481–486, 2011.

[90] J. A. Nelder and R. Mead, "A simplex method for function minimization", *The Computer Journal*, vol. 7, 308–313, 1965.

[91] R. Neutze, R. Wouts, D. van der Spoel, E. Weckert, and J. Hajdu, "Potential for biomolecular imaging with femtosecond x-ray pulses", *Nature*, vol. 406, 752–757, 2000.

[92] L. Novotny and B. Hecht, "Principles of Nano-Optics". 2006.

[93] D. Paganin, "Coherent X-Ray Optics", English. 2006, xii, 411 p. : ISBN: 9780198567288 0198567286.

[94] G. J. Palenik, W. P. Jensen, and I.-H. Suh, "The history of molecular structure determination viewed through the nobel prizes", *J. Chem. Educ.*, vol. 80, 753, 2003.

[95] D. T. Papageorgiou, "On the breakup of viscous liquid threads", *Physics of Fluids*, vol. 7, 1529–1544, 1995.

[96] B. Pedrini, A. Menzel, M. Guizar-Sicairos, V. A. Guzenko, S. Gorelick, C. David, B. D. Patterson, and R. Abela, "Two-dimensional structure from random multiparticle x-ray scattering images using cross-correlations", *Nature Communications*, vol. 4, 1647, 2013.

[97] H. T. Philipp, K. Ayyer, M. W. Tate, V. Elser, and S. M. Gruner, "Solving structure with sparse, randomly-oriented x-ray data", *Optics Express*, vol. 20, 13129–13137, 2012.

[98] D. Popmintchev, C. Hernández-García, F. Dollar, et al., "Ultraviolet surprise: efficient soft x-ray high-harmonic generation in multiply ionized plasmas", *Science*, vol. 350, 1225–1231, 2015.

[99] E. M. Purcell and C. R. Pennypacker, "Scattering and Absorption of Light by Nonspherical Dielectric Grains", *Astrophysical Journal*, vol. 186, 705–714, 1973.

[100] K. S. Raines, S. Salha, R. L. Sandberg, H. Jiang, J. A. Rodriguez, B. P. Fahimian, H. C. Kapteyn, J. Du, and J. Miao, "Three-dimensional structure determination from a single view", *Nature*, vol. 463, 214–217, 2010.

[101] A. Ravasio, D. Gauthier, F. R. N. C. Maia, et al., "Single-shot diffractive imaging with a table-top femtosecond soft x-ray laser-harmonics source", *Phys. Rev. Lett.*, vol. 103, 028104, 2009.

[102] R. Redmer, H. Reinholz, G. Röpke, R. Thiele, and A. Höll, "Theory of x-ray thomson scattering in dense plasmas", *IEEE Transactions on Plasma Science*, vol. 33, 77–84, 2005.

[103] D. Reinhard, B. D. Hall, D. Ugarte, and R. Monot, "Size-independent fcc-to-icosahedral structural transition in unsupported silver clusters: an electron diffraction study of clusters produced by inert-gas aggregation", *Phys. Rev. B*, vol. 55, 7868–7881, 1997.

[104] D. Riley, N. C. Woolsey, D. McSherry, I. Weaver, A. Djaoui, and E. Nardi, "X-ray diffraction from a dense plasma", *Phys. Rev. Lett.*, vol. 84, 1704–1707, 2000.

[105] I. K. Robinson, I. A. Vartanyants, G. J. Williams, M. A. Pfeifer, and J. A. Pitney, "Reconstruction of the shapes of gold nanocrystals using coherent x-ray diffraction", *Phys. Rev. Lett.*, vol. 87, 195505, 2001.

[106] J. Rodriguez-Carvajal, "Recent advances in magnetic structure determination by neutron powder diffraction", *Physica B: Condensed Matter*, vol. 192, 55–69, 1993.

[107] P. Rudawski, C. M. Heyl, F. Brizuela, et al., "A high-flux high-order harmonic source", *Review of Scientific Instruments*, vol. 84, 073103, 2013.

[108] D. Rupp, M. Adolph, T. Gorkhover, et al., "Identification of twinned gas phase clusters by single-shot scattering with intense soft x-ray pulses", *New Journal of Physics*, vol. 14, 055016, 2012.

[109] D. Rupp, N. Monserud, B. Langbehn, et al., "Coherent diffractive imaging of single helium nanodroplets with a high harmonic generation source", *Nature Communications*, vol. 8, 493, 2017.

[110] D. Rupp, M. Adolph, L. Flückiger, et al., "Generation and structure of extremely large clusters in pulsed jets", *The Journal of Chemical Physics*, vol. 141, 044306, 2014.

[111] D. Rupp, L. Flückiger, M. Adolph, et al., "Diffractive imaging of transient electronic core-shell structures in a nanoplasma", *arXiv*, submitted, 2017. [Online]. Available: https://arxiv.org/abs/1611.01074.

[112] M. Rycenga, C. M. Cobley, J. Zeng, W. Li, C. H. Moran, Q. Zhang, D. Qin, and Y. Xia, "Controlling the synthesis and assembly of silver nanostructures for plasmonic applications", *Chemical Reviews*, vol. 111, 3669–3712, 2011.

[113] Y. Saad, "Iterative methods for sparse linear systems". 2003.

[114] J. D. Sadler, R. Nathvani, P. Oleśkiewicz, L. A. Ceurvorst, N. Ratan, M. F. Kasim, R. M. G. M. Trines, R. Bingham, and P. A. Norreys, "Compression of x-ray free electron laser pulses to attosecond duration", *Scientific Reports*, vol. 5, 16755–, 2015.

[115] D. K. Saldin, H. C. Poon, V. L. Shneerson, M. Howells, H. N. Chapman, R. A. Kirian, K. E. Schmidt, and J. C. H. Spence, "Beyond small-angle x-ray scattering: exploiting angular correlations", *Phys. Rev. B*, vol. 81, 174105, 2010.

[116] R. L. Sandberg, A. Paul, D. A. Raymondson, et al., "Lensless diffractive imaging using tabletop coherent high-harmonic soft-x-ray beams", *Phys. Rev. Lett.*, vol. 99, 098103, 2007.

[117] K. Sander, C. Peltz, C. Varin, S. Scheel, T. Brabec, and T. Fennel, "Influence of wavelength and pulse duration on single-shot x-ray diffraction patterns from nonspherical nanoparticles", *Journal of Physics B: Atomic, Molecular and Optical Physics*, vol. 48, 204004, 2015.

[118] D. Sayre, "Some implications of a theorem due to shannon", *Acta Crystallographica*, vol. 5, 843, 1952.

[119] J. R. Schneider, "Flash - from accelerator test facility to the first single-pass soft x-ray free-electron laser", *Journal of Physics B: Atomic, Molecular and Optical Physics*, vol. 43, 194001, 2010.

[120] P. Schwander, D. Giannakis, C. H. Yoon, and A. Ourmazd, "The symmetries of image formation by scattering. ii. applications", *Opt. Express*, vol. 20, 12827–12849, 2012.

[121] M. D. Seaberg, D. E. Adams, E. L. Townsend, et al., "Ultrahigh 22 nm resolution coherent diffractive imaging using a desktop 13 nm high harmonic source", *Opt. Express*, vol. 19, 22470–22479, 2011.

[122] M. M. Seibert, T. Ekeberg, F. R. N. C. Maia, et al., "Single mimivirus particles intercepted and imaged with an x-ray laser", *Nature*, vol. 470, 78–81, 2011.

[123] P. Self, M. O'Keefe, P. Buseck, and A. Spargo, "Practical computation of amplitudes and phases in electron diffraction", *Ultramicroscopy*, vol. 11, 35–52, 1983.

[124] Y. Shechtman, Y. C. Eldar, O. Cohen, H. N. Chapman, J. Miao, and M. Segev, "Phase retrieval with application to optical imaging: a contemporary overview", *IEEE Signal Processing Magazine*, vol. 32, 87–109, 2015.

[125] S. K. Sinha, E. B. Sirota, S. Garoff, and H. B. Stanley, "X-ray and neutron scattering from rough surfaces", *Phys. Rev. B*, vol. 38, 2297–2311, 1988.

[126] L. Slabinski, L. Jaroszewski, A. P. Rodrigues, L. Rychlewski, I. A. Wilson, S. A. Lesley, and A. Godzik, "The challenge of protein structure determination–lessons from structural genomics", *Protein Science : A Publication of the Protein Society*, vol. 16, 2472–2482, 2007.

[127] C. Song, H. Jiang, A. Mancuso, B. Amirbekian, L. Peng, R. Sun, S. S. Shah, Z. H. Zhou, T. Ishikawa, and J. Miao, "Quantitative imaging of single, unstained viruses with coherent x rays", *Phys. Rev. Lett.*, vol. 101, 158101, 2008.

[128] W. Sun and Q. Fu, "Finite-difference time-domain solution of light scattering by dielectric particles with large complex refractive indices", *Appl. Opt.*, vol. 39, 5569–5578, 2000.

[129] W. Sun, Q. Fu, and Z. Chen, "Finite-difference time-domain solution of light scattering by dielectric particles with a perfectly matched layer absorbing boundary condition", *Appl. Opt.*, vol. 38, 3141–3151, 1999.

[130] C. M. Surko, G. J. Dick, F. Reif, and W. C. Walker, "Spectroscopic study of liquid helium in the vacuum ultraviolet", *Phys. Rev. Lett.*, vol. 23, 842–846, 1969.

[131] E. J. Takahashi, P. Lan, O. D. M"ucke, Y. Nabekawa, and K. Midorikawa, "Attosecond nonlinear optics using gigawatt-scale isolated attosecond pulses", vol. 4, 2691, 2013.

[132] C. Ungureanu, R. G. Rayavarapu, S. Manohar, and T. G. van Leeuwen, "Discrete dipole approximation simulations of gold nanorod optical properties: choice of input parameters and comparison with experiment", *Journal of Applied Physics*, vol. 105, 102032, 2009.

[133] J. D. Watson and F. H. C. Crick, "Molecular structure of nucleic acids: a structure for deoxyribose nucleic acid", *Nature*, vol. 171, 737–, 1953.

[134] J. L. Wierman, T.-Y. Lan, M. W. Tate, H. T. Philipp, V. Elser, and S. M. Gruner, "Protein crystal structure from non-oriented, single-axis sparse x-ray data", *IUCrJ*, vol. 3, 43–50, 2015.

[135] G. J. Williams, M. A. Pfeifer, I. A. Vartanyants, and I. K. Robinson, "Three-dimensional imaging of microstructure in au nanocrystals", *Phys. Rev. Lett.*, vol. 90, 175501, 2003.

[136] R. Xu, H. Jiang, C. Song, et al., "Single-shot three-dimensional structure determination of nanocrystals with femtosecond x-ray free-electron laser pulses", *Nat. Comm.*, vol. 5, 4061, 2014.

[137] P. Yang and K. N. Liou, "Finite-difference time domain method for light scattering by small ice crystals in three-dimensional space", *J. Opt. Soc. Am. A*, vol. 13, 2072–2085, 1996.

[138] W.-H. Yang, G. C. Schatz, and R. P. Van Duyne, "Discrete dipole approximation for calculating extinction and raman intensities for small particles with arbitrary shapes", *The Journal of Chemical Physics*, vol. 103, 869–875, 1995.

[139] K. Yee, "Numerical solution of initial boundary value problems involving maxwell's equations in isotropic media", *IEEE Transactions on Antennas and Propagation*, vol. 14, 302–307, 1966.

[140] O. Yefanov, C. Gati, G. Bourenkov, R. A. Kirian, T. A. White, J. C. H. Spence, H. N. Chapman, and A. Barty, "Mapping the continuous reciprocal space intensity distribution of x-ray serial crystallography", *Philosophical Transactions of the Royal Society of London B: Biological Sciences*, vol. 369, 2014.

[141] L.-H. Yeh, J. Dong, J. Zhong, L. Tian, M. Chen, G. Tang, M. Soltanolkotabi, and L. Waller, "Experimental robustness of fourier ptychography phase retrieval algorithms", *Opt. Express*, vol. 23, 33214–33240, 2015.

[142] M. A. Yurkin and A. G. Hoekstra, "The discrete dipole approximation: an overview and recent developments", *Journal of Quantitative Spectroscopy and Radiative Transfer*, vol. 106, 558–589, 2007.

[143] M. A. Yurkin and A. G. Hoekstra, "The discrete-dipole-approximation code adda: capabilities and known limitations", *Journal of Quantitative Spectroscopy and Radiative Transfer*, vol. 112, 2234–2247, 2011, Polarimetric Detection, Characterization, and Remote Sensing.

[144] J. M. Zuo, I. Vartanyants, M. Gao, R. Zhang, and L. A. Nagahara, "Atomic resolution imaging of a carbon nanotube from diffraction intensities", *Science*, vol. 300, 1419–1421, 2003.

[145] M. Zürch, J. Rothhardt, S. Hädrich, S. Demmler, M. Krebs, J. Limpert, A. Tünnermann, A. Guggenmos, U. Kleineberg, and C. Spielmann, "Real-time and sub-wavelength ultrafast coherent diffraction imaging in the extreme ultraviolet", vol. 4, 7356, 2014.

Scientific curriculum vitae

Not included in the online version.

Declaration of authorship

gemäß §4 der Promotionsordnung
der mathematisch-naturwissenschaftlichen Fakultät
der Universität Rostock

Ich gebe folgende Erklärung ab:

1. Die Gelegenheit zum vorliegenden Promotionsvorhaben ist mir nicht kommerziell vermittelt worden. Insbesondere habe ich keine Organisation eingeschaltet, die gegen Entgelt Betreuer*innen für die Anfertigung von Dissertationen sucht oder die mir obliegenden Pflichten hinsichtlich der Prüfungsleistungen für mich ganz oder teilweise erledigt.

2. Ich versichere hiermit an Eides statt, dass ich die vorliegende Arbeit selbstständig angefertigt und ohne fremde Hilfe verfasst habe. Dazu habe ich keine außer den von mir angegebenen Hilfsmitteln und Quellen verwendet und die den benutzten Werken inhaltlich und wörtlich entnommenen Stellen habe ich als solche kenntlich gemacht.

Rostock, 15. August 2018 .....
Katharina Sander

Acknowledgements

Ich möchte mich an dieser Stelle bei meinem Doktorvater Thomas Fennel bedanken, der es mir nicht nur ermöglicht hat an diesen spannenden Themen während meiner Promotion zu arbeiten, sondern auch diverse Reisen zu interessanten Fachkonferenzen und Experimenten und die Zusammenarbeit mit vielen Kollaborationspartnerinnen und -partnern ermöglicht hat. Weiterhin möchte ich mich bei der gesamten AG Theoretische Clusterphysik und Nanophotonik für die tolle Atmosphäre in der Gruppe und im Büro bedanken. Zu nennen sind dabei Christian Peltz, Lennart Seiffert, Björn Kruse and Benjamin Liewehr, sowie Mathias Arbeiter. Auch den anderen Promovierenden des Graduiertenkollegs möchte ich danken, für tolle Seminarwochenenden und den wissenschaftlichen und sozialen Austausch. Außerdem bedanke ich mich bei Madlen und auch Oskar für die schönen Kaffeepausen.

Eine große Bereicherung für meine Promotionsarbeit waren wie bereits gesagt die zahlreichen Kollaborationen, mit der AG von Thomas Möller der TU Berlin, später der Gruppe von Daniela Rupp vom MBI Berlin und Maxim Yurkin der Novosibirsk State University. Insbesondere möchte ich mich hier bei Maxim Yurkin, Bruno Langbehn und Daniela Rupp für die tolle Zusammenarbeit bedanken. Letzterer und Anatoli Ulmer möchte ich außerdem für das schnelle Durchsehen von Teilen der Arbeit danken.

Zum Schluss möchte ich mich natürlich noch bei meiner Familie und meinen Freunden und Freundinnen bedanken, insbesondere Caro und Tommy ♡.